Davies, P. J., McKenzie, J. A., Palmer-Julson, A., et al., 1991
Proceedings of the Ocean Drilling Program, Initial Reports, Vol. 133

8. SITE 815[1]

Shipboard Scientific Party[2]

HOLE 815A

Date occupied: 27 August 1990

Date departed: 30 August 1990

Time on hole: 3 days, 1 hr

Position: 19°9.034′S, 149°59.508′E

Bottom felt (rig floor; m , drill-pipe measurement): 476.7

Distance between rig floor and sea level (m): 11.17

Water depth (drill-pipe measurement from sea level, m): 465.5

Total depth (rig floor; m): 950.2

Penetration (m): 473.5

Number of cores (including cores with no recovery): 51

Total length of cored section (m): 473.5

Total core recovered (m): 415.37

Core recovery (%): 87

Oldest sediment cored:
Depth (mbsf): 463.8
Nature: dolomitized foraminifer rudstone
Age: early to middle Miocene

SITE 815B

Date occupied: 30 August 1990

Date departed: 31 August 1990

Time on hole: 5 hr, 15 min

Position: 19°9.034′S, 149°59.524′

Bottom felt (rig floor; m, drill-pipe measurement): 477.1

Distance between rig floor and sea level (m): 11.17

Water depth (drill-pipe measurement from sea level, m): 465.9

Total depth (rig floor, m): 513.5

Penetration (m): 36.4

Number of cores (including cores with no recovery): 4

Total length of cored section (m): 36.4

Total core recovered (m): 37.79

Core recovery (%): 103

Oldest sediment cored:
Depth (mbsf): 36.4
Nature: foraminifer nannofossil ooze with clay
Age: late Pliocene

Principal results: Site 815 is situated along the southern margin of the Townsville Trough, about 3 km north and in front of the northwestern edge of the Marion Plateau. Drilling penetrated a 473.5-m-thick sequence of sediments composed of a 416-m-thick package of uppermost Miocene–Pleistocene hemipelagic sediments overlying uppermost lower to middle Miocene and upper Miocene shelf carbonates. Benthic foraminifer assemblages in the uppermost Miocene sediments indicate outer neritic water depths (100–200 m), but also contain redeposited reefal taxa. During the period of hemipelagic sedimentation, Site 815 had deepened to upper bathyal depths (200–600 m). Sedimentation rates during the late Pliocene to Pleistocene were 1.7 to 3.2 cm/k.y., which is relatively normal for a pelagic setting, but increased 10-fold during the early Pliocene, with rates up to 38.5 cm/k.y. for the interval between 3.51 and 4.24 Ma. The expanded lower Pliocene section, with about 275 m of sediment, offers great potential for high-resolution biostratigraphic investigations.

Six major sedimentary units were recovered between the seafloor and 473.5 mbsf. These lithologic units are described as follows:

1. *Unit I:* depth, 0 to 73.3 mbsf; age, Pleistocene to late early Pliocene. Unit I is divided into three subunits based on color and clay content of the predominantly foraminifer nannofossil to nannofossil foraminifer ooze. The nannofossil content varies between 20% and 30%.

Subunit IA: depth, 0 to 16.3 mbsf; age, Pleistocene. Subunit IA contains alternating pale brown and white foraminifer nannofossil to nannofossil foraminifer ooze with varying amounts of micrite and bioclastic debris and zero to low clay content.

Subunit IB: depth, 16.3 to 35.3 mbsf; age, late late Pliocene. Subunit IB differs from the overlying oozes in that it has consistently higher clay content and exhibits alternating dark and light intervals.

Subunit IC: depth, 35.3 to 73.3 mbsf; age, early to late Pliocene to late early Pliocene. Subunit IC differs from the overlying oozes in that it has a variable clay content (up to 25%) and is darker in color, changing from a light gray to darker gray.

2. *Unit II:* depth, 73.3 to 280.5 mbsf; age, early Pliocene. Unit II comprises the greatly expanded lower Pliocene section recovered at Site 815. These sediments are greenish-gray to gray, slightly bioturbated nannofossil oozes to unlithified nannofossil mixed sediment. Unit II has been divided into two subunits on the basis of the degree of induration and varying percentages of foraminifers and nannofossils.

Subunit IIA: depth, 73.3 to 111.3 mbsf; age, early Pliocene. Subunit IIA is characterized by soft to very firm, dark gray to gray, foraminifer nannofossil and nannofossil foraminifer ooze. Thin, patchy chalk to lithified intervals occur between 92.3 and 111.3 mbsf. The nannofossil content is about 25%.

Subunit IIB: depth, 111.3 to 280.5 mbsf; age, early Pliocene. Subunit IIB is characterized by local partial lithification of the dark to light greenish-gray to varying gray nannofossil ooze with clayey nannofossil mixed sediment. Repetitive color changes suggest cyclic sedimentation, while the color pattern is probably controlled by changes in both grain size and carbonate content. The nannofossil content varies between 10% and 35%.

3. *Unit III:* depth, 280.5 to 348.4 mbsf; age, early Pliocene. The greenish-gray to gray foraminifer nannofossil and nannofossil foraminifer chalks comprising Unit III are distinguished by a marked increase in degree of induration and by intervals of contorted and folded bedding. The nannofossil content increases strikingly in Unit III, with values up to 80%.

Subunit IIIA: depth, 280.5 to 306.25 mbsf; age, early Pliocene. Subunit IIIA contains foraminifer nannofossil and nannofossil foraminifer chalks that are distinguished by the presence of numerous and generally larger burrow structures.

[1] Davies, P. J., McKenzie, J. A., Palmer-Julson, A., et al., 1991. *Proc. ODP, Init. Repts.*, 133: College Station, TX (Ocean Drilling Program).
[2] Shipboard Scientific Party is as given in list of participants preceding the contents.

Subunit IIIB: depth, 306.25 to 348.4 mbsf; age, early Pliocene. The foraminifer nannofossil and nannofossil foraminifer chalks of Subunit IIIB are characterized by the occurrence of contorted and locally folded bedding within blocks of chalk and within the matrix sediment. Evidence of several discrete intervals of slumping is present. Soft sediment deformation of the blocks may have occurred during transport.

4. *Unit IV:* depth, 348.4 to 425.3 mbsf; age, late late Miocene to early early Pliocene. Unit IV contains predominantly greenish-gray, foraminifer nannofossil and nannofossil foraminifer chalks having a marked increase in the number of burrows preserved as sedimentary structures. Larger burrows become more numerous with depth; recognized trace fossils include *Chondrites*, *Zoophycos*, *Planolites*, and possibly *Scoyenia*. The nannofossil content varies between 35% and 50%.

5. *Unit V:* depth, 425.3 to 444.5 mbsf; age, late Miocene. Unit V contains pale brown, dolomitized and lithified foraminifer packstones with bioclasts and minor amounts of chalk. Trace fossils are abundant in the upper part of the unit, but become less common with depth. Between Units V and VI, (444.5–454.2 mbsf), nothing was recovered, while downhole logging did not reach this level. Consequently, interpretation of this interval is impossible at this time.

6. *Unit VI:* depth, 454.2 to 463.8 mbsf; age, latest early Miocene to early middle Miocene. Dolomitized, white, large benthic foraminifer rudstones to floatstones within a planktonic foraminifer packstone characterize the material of Unit VI, where recovery was poor.

The interstitial water chemistry of the hemipelagic sequence cored at Site 815 shows a downward trend of increasing ionic concentrations that points to an underlying source of water having an elevated salinity, probably associated with evaporite dissolution. Within the upper 200 m of the section, the chemistry apparently is controlled by clay mineral alteration, metastable carbonate dissolution, and bacterial sulfate reduction. The byproduct of this latter reaction, H_2S, is consumed during formation of pyrite. Higher magnetic susceptibility (between 125 and 440 mbsf) indicates the presence of ferrimagnetic minerals. Large nodules (~3 cm) of pyrite were observed below 350 mbsf. This correlates with increased concentrations of bulk sulfur (up to 0.45%) between 350 and 440 mbsf. Apparently, all of the components for pyrite formation (organic matter, sulfate, and ferrous iron) are available in this system; in particular, an unlimited supply of sulfate is migrating upward from an underlying source, as shown by the progressive increase in concentrations of sulfate with depth below about 200 mbsf.

The predominant carbonate mineral is calcite, but aragonite also is present within the hemipelagic sequence. The mineral disappears downward within the Pleistocene sediments, but reappears in upper and lower Pliocene sediments, while contents range between 2% and 23%. High Mg-calcite was recorded at 4.5 mbsf, but was not found again below this level. The carbonate content varies greatly from more than 90% to as low as 34.3%, but an overall trend toward decreasing values downward occurs between about 75 and 260 mbsf. This interval lies within the expanded lower Pliocene section. Estimates of the nannofossil content in core-catcher samples remain constant throughout the high-sedimentation period (3.51 to 4.24 Ma), implying that pelagic contribution to these sediments did not vary significantly. Thus, variations recorded in carbonate content probably are related to changes in carbonate composition of detrital influx and may reflect the contribution of material that eroded from regional carbonate platforms vs. terrestrial influx of clays.

The mechanism of lateral transport of fine-grained material and deposition as a drift or contourite best explains rapid accumulation of a 275-m-thick wedge of sediments between 3.51 and 4.24 Ma at Site 815, as well as the geometric expression of the sedimentary deposit in seismic profiles. This interval of accelerated sedimentation is characterized by distinctive physical properties, as observed in both shipboard analyses and downhole logging profiles. Shipboard measurements of porosity, bulk density, and water content of sediments through this interval indicate abnormally constant values with depth. This suggests that the high sedimentation rate rapidly buried the sediments and in combination with low permeabilities did not allow sufficient time for the sediments to dewater, as normally occurs with burial compaction. Velocity and density logs show a simple, first-order compaction profile with depth. In addition, these logs and the resistivity log contain high frequency variations, indicating porosity anomalies related to a combination of changes in consolidation and lithology.

Shipboard paleomagnetic studies revealed a good reversal stratigraphy in the upper Pliocene–Pleistocene with sediments registering the Gauss/Gilbert boundary at about 62 mbsf (3.4 Ma). Based on our initial results, we should be able to resolve a good paleomagnetic reversal signal in the uppermost Miocene–lower Pliocene sediments with our shore-based study of discrete samples.

Total organic carbon content of the sediments was low but variable and ranged from 0% to 1.0%. Volatile hydrocarbons (with methane concentrations up to 9 ppm and rare trace amounts of ethane and propane) presented no safety problems.

BACKGROUND AND SCIENTIFIC OBJECTIVES

Sites 815 and 816 occur along the northern margin of the Marion Plateau, approximately 250 km east of the Australian mainland (see Fig. 1, "Introduction" chapter, this volume). The Marion Plateau lies directly east of the central Great Barrier Reef (GBR) and covers an area of approximately 77,000 km^2. It is bounded along its northern margin by the Townsville Trough and along its eastern margin by the Cato Trough (see Fig. 4, "Introduction" chapter, this volume). The present-day plateau surface forms a deeper water extension of the Australian continental shelf, with water depths ranging from 100 m along the western border to 500 m along the eastern margin. At the present time, reef growth is restricted to Marion Reef on the northeastern corner and Saumarez Reef at the southeastern extremity of the plateau (Davies et al., 1989).

Little detailed subsurface structure and facies distribution information exists for the Marion Plateau (Mutter and Karner, 1980). A summary of recently acquired BMR (Davies et al., 1989) data is shown in Figure 1. During the early Tertiary, the Marion Plateau formed a marginal plateau separated from the continent by a series of half grabens. Basement beneath the plateau is a planated surface that dips gently to the northeast; the basement surface is steeply downfaulted into the Townsville and Cato troughs. The slope sequences on the northern and eastern margins of the plateau both onlap and prograde.

Basement was completely transgressed during the early Miocene, with the resulting development of a carbonate platform (MR1 in Fig. 1). Currently, the top of this platform is thought to lie at a depth of about 450 m. Shelf-edge barrier reefs (Fig. 2A) and platform reefs, separated by lagoons and inter-reef areas (Fig. 2B), can be identified in the subsurface over the northeastern two-thirds of the platform (Fig. 3). Barrier reefs formed a distinct rimmed margin only along the northern edge of the plateau. A second and later phase of reef development has been identified in the south of the plateau (Fig. 3), and this phase of platform growth was initiated at a topographic level that was considerably lower than the top of the first growth phase. A third phase of growth occurs as small discrete reefal areas, whereas a fourth—and even more restricted—phase is ongoing at Marion and Saumarez reefs.

At the present time, the upper surface of the Marion Plateau is swept by moderately strong currents such that only hemipelagic sediments are accumulating in restricted areas. This was not always the case, however; the downlapping sequences along the northern margin of the plateau (Fig. 4) suggest that currents, probably the East Australia Boundary Current, have been operating for a substantial time.

Little is known about the tectonic history of the Marion Plateau, or how it relates to that of the Queensland Plateau. It

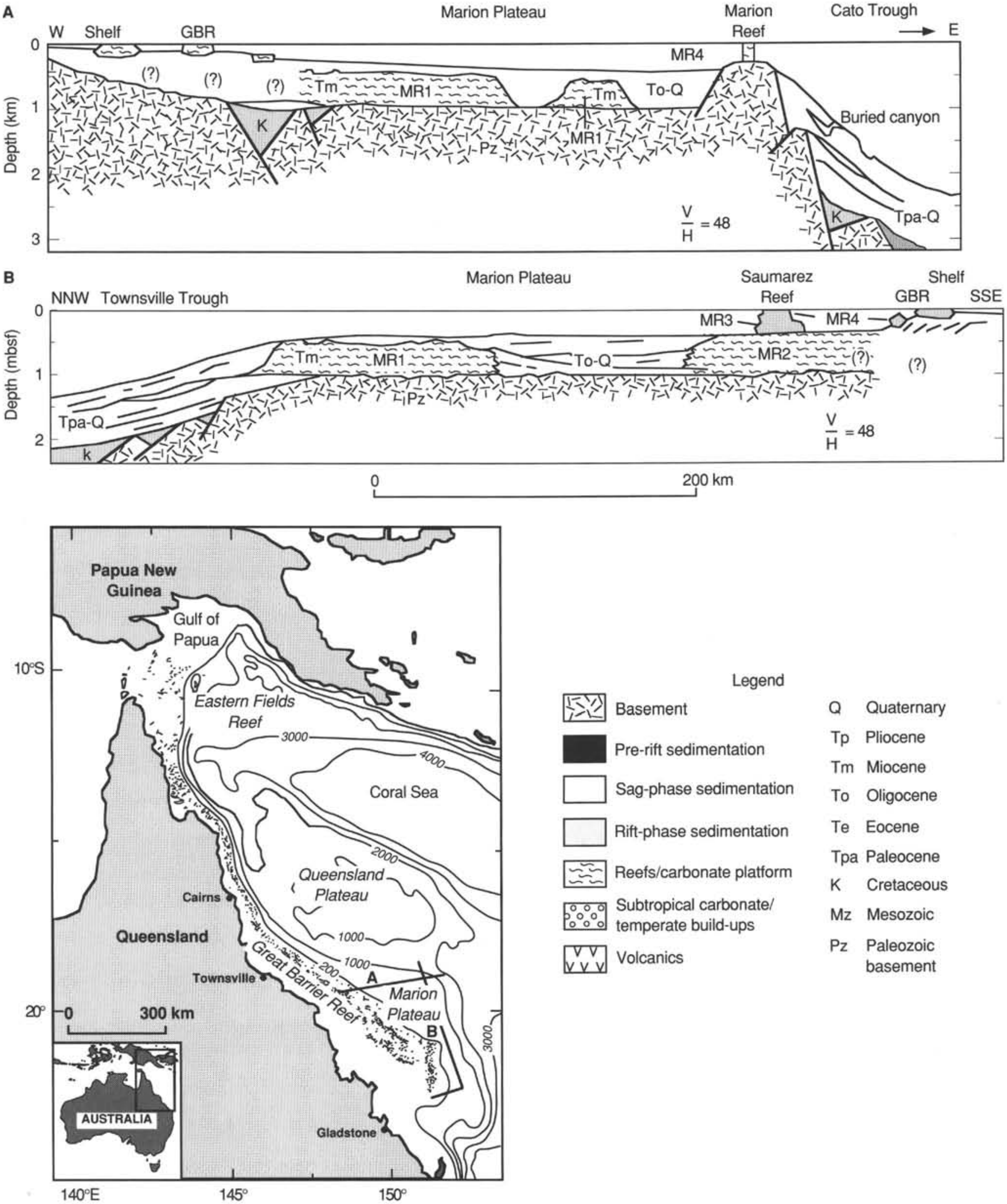

Figure 1. Schematic cross sections (**A** and **B**) of Marion Plateau showing relationship of the platform accretion phases to basement and the modern GBR. MR1 to MR4 refer to carbonate platform growth phases.

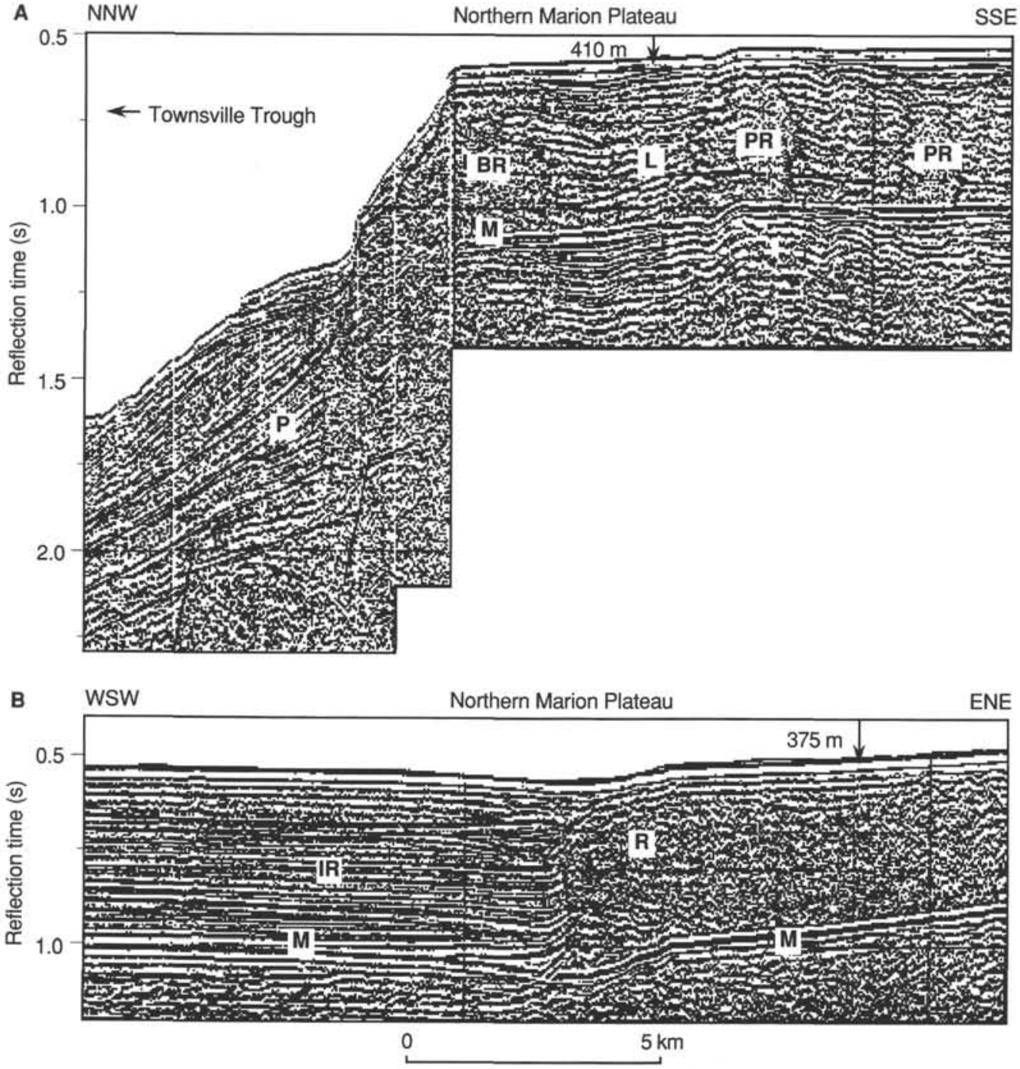

Figure 2. Seismic sections across Marion Plateau carbonate platforms. **A.** Water-gun section showing MR1 platform margin adjacent to Townsville Trough. Note reflection-free, thick, barrier reef (BR) and patch reef facies (PR), fore-reef periplatform facies (P), and back barrier, bedded, lagoonal facies (L). **B.** Water-gun section across northeastern Marion Plateau showing development of platform reefs (R) and bedded inter-reef sediments (IR); M = multiple.

appears that at some time the carbonate factory of the Marion Plateau was closed down suddenly, presumably as a consequence of subsidence of the platform. Drilling at Sites 815 and 816 was intended to help determine these relationships and to allow us to compare them with the history of Queensland Plateau.

Site 815 is located in approximately 465 m of water on the northern margin of the Marion Plateau, on the southern edge of the Townsville Trough. Distribution of site-survey data is shown in Figure 5, and a seismic section through the site, including the pre-drilling prognosis, is presented in Figure 6. We think that the downlapping sequence was deposited by the East Australian Current and that it may define the timing of the onset of the current along the eastern Australian margin. The basal reflector near the proposed termination depth of the hole (horizon 9) we think is related to reef development to the west and thus may indicate change in sea level at the time of formation.

Objectives for Site 815 were as follows:

1. To determine the cause and timing of the demise of the oldest phase of carbonate platform accretion as a key for understanding controls of the development of carbonate platforms on Marion Plateau.
2. To determine the nature and age of the periplatform sequence deposited throughout much of the Neogene and Pliocene–Pleistocene, both during and between periods of carbonate platform growth.
3. To record and understand the paleoclimatic and paleoceanographic factors controlling the development of carbonate platforms.

OPERATIONS

Transit to Site 815

The transit from Hole 812C to Site 815 (proposed Site NEA-14) covered 78 nmi in 7.0 hr at an average speed of 11 kt. A seismic survey was conducted over Sites 815 and 816 (proposed Sites NEA-14 and NEA-13), which covered 23 nmi in 4.75 hr at an average speed of 4.8 kt. A Datasonics commandable release beacon was dropped at 2155L (all times are in local time, or L), 27 August 1990, at the previously

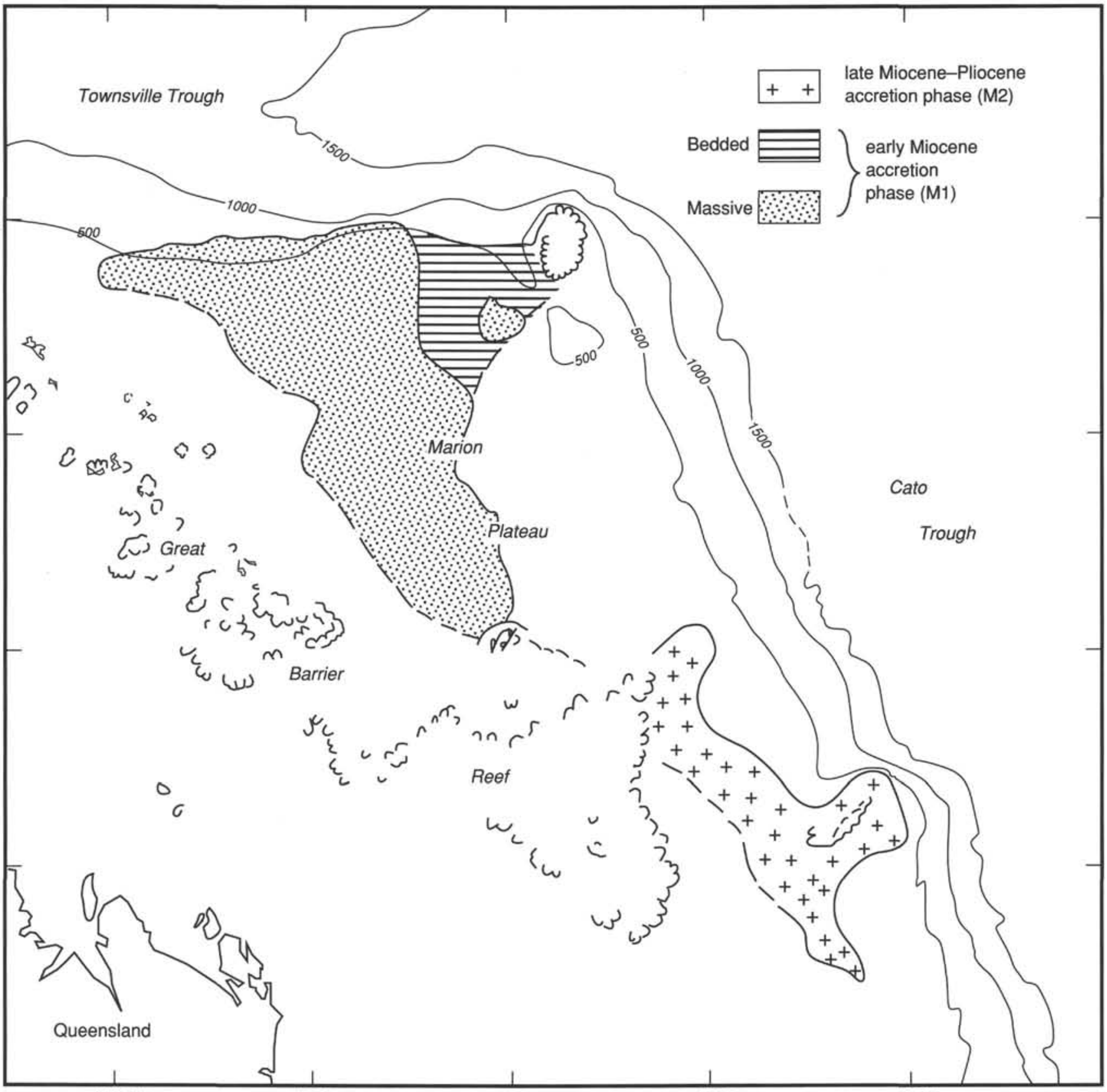

Figure 3. Map showing location of major phases of platform development on Marion Plateau.

surveyed global positioning system (GPS) coordinates 19°9.034′S, 149°59.508′E.

Hole 815A

A used Security four-cone insert bit was run with a seal bore drill collar, monel drill collar, and Hydrolex jars in a 12-drill-collar bottom-hole assembly (BHA). The precision depth recorder (PDR) indicated that water depth was 466.6 m from sea level. The bit was positioned at a water depth of 462.8 m, and the first core was shot. From Core 133-815A-1H, we recovered 6.8 m of sediment, which placed the mud line at a water depth of 465.5 m from sea level. Continuous APC cores (Cores 133-815A-1H through -9H) were taken from 0 to 82.8 mbsf, with 82.8 m cored and 85.38 m recovered (103.1% recovery). At that point, we unexpectedly lost the acoustic signal from the beacon, and a back-up Benthos model was launched at 0430L, 28 August. The ship drifted off location about 35 ft (about 2°); coring was resumed after we repositioned the ship.

Continuous APC cores (Cores 133-815A-10H through -25H) were taken from 82.8 to 225.8 mbsf, with 143.0 m cored and 148.1 m recovered (103.6%). APC coring ended in hard clay because of repeated failure of the core liner. Overpull was negligible.

Cores 133-815A-26X through -51X were taken from 225.8 to 473.5 mbsf, with 247.7 m cored and 184.1 m recovered (74.3% recovery). We obtained approval to extend coring past the originally approved target depth of 400 mbsf to reach a seismic reflector objective. No hole problems were noted in the clay, although the circulation rate and pressure were increased to prevent bit-nozzle plugging.

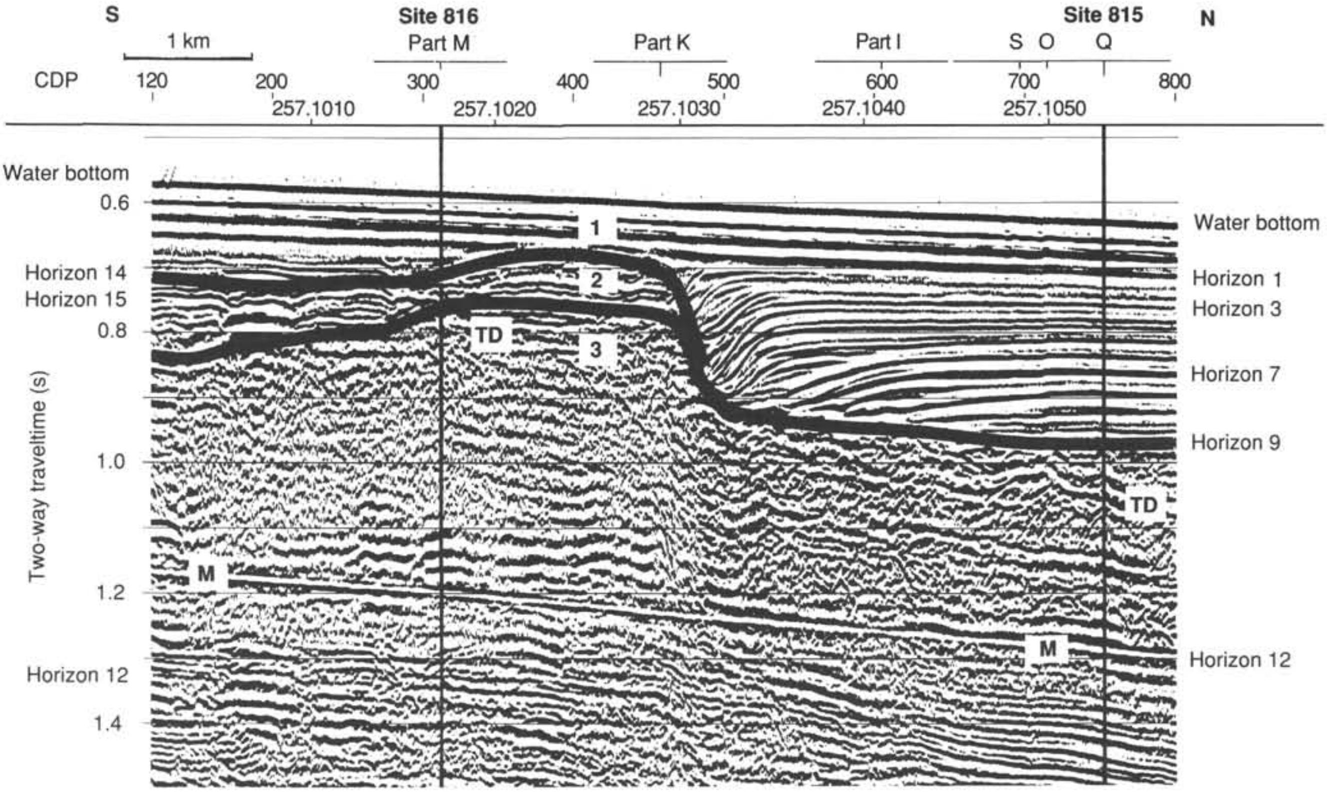

Figure 4. Seismic sections of Sites 815 and 816 (BMR Line 75/27, Part A); M = multiple.

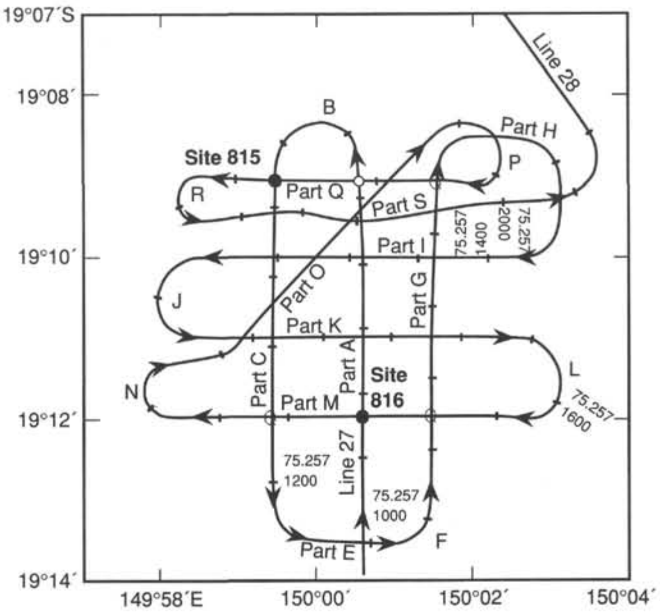

Figure 5. Track map of site-survey data for Sites 815 and 816.

A short trip was made to condition the hole for logs; no drag was noted. The bit encountered 13 m of fill, starting at the top of an interval of poor recovery. A 30-bbl-mud sweep was circulated to clean the hole before logging.

Logs were run as follows:

1. The induction/density/sonic/caliper/gamma-ray (DITE/HLDT/SDT/MCDG/NGT) logging tool was placed in the hole at 0954L, 30 August, encountered 31.3 m of fill at the bot4tom of the hole, and was removed from the hole at 1420L. Problems persisted with the Schlumberger logging computer, despite our installation of new hardware and software.

2. The geochemical/aluminum clay tool/gamma-ray (GST/ACT/CNTG/NGT/TCC) logging tool was placed in the hole at 1615L, 30 August, where it encountered 149.5 m of fill. Computer problems continued and logging was terminated; the tool string was out of the hole at 2110L, 30 August.

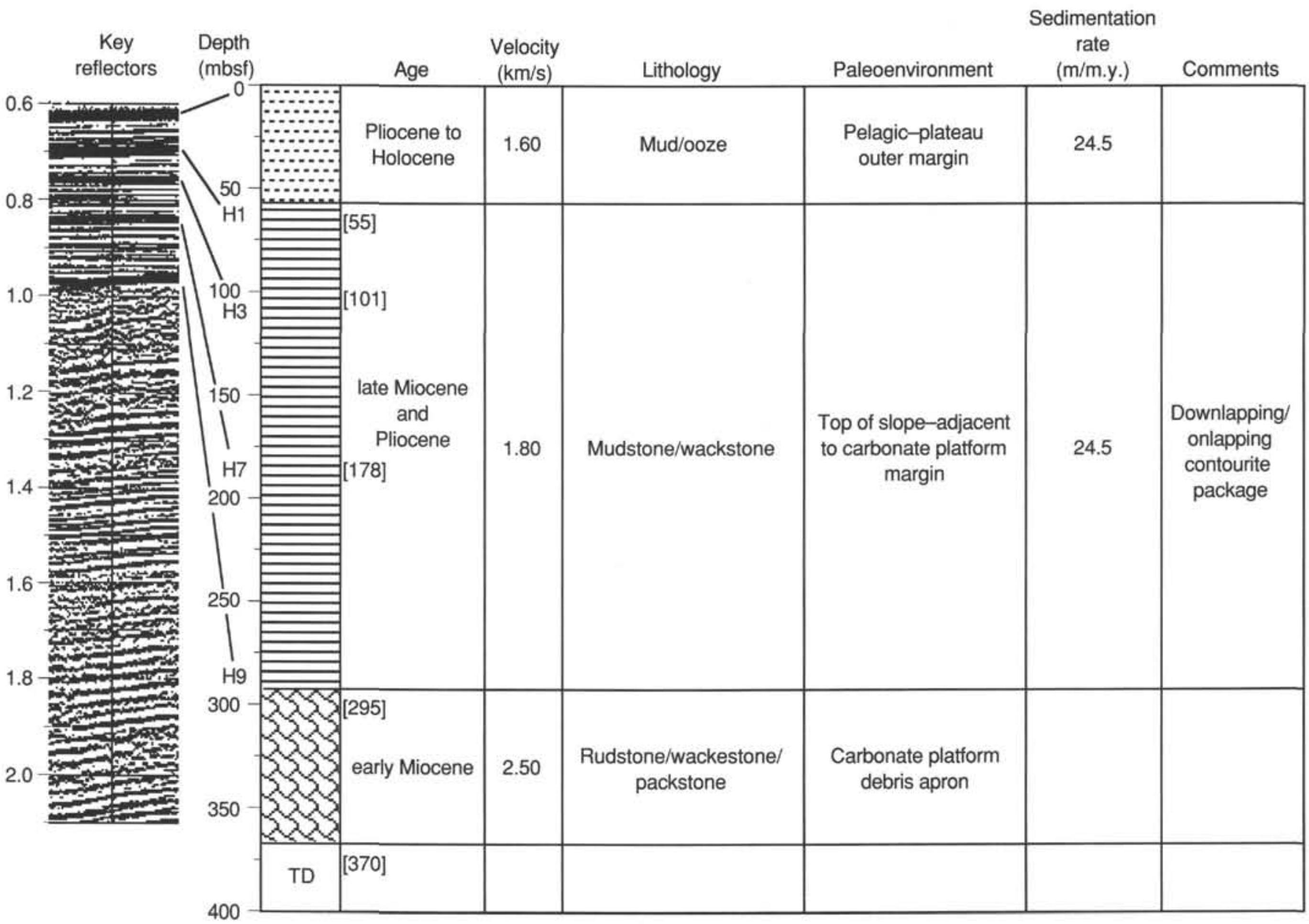

Figure 6. Pre-drilling prognosis for Site 815.

The BHA was pulled out of the hole to a water depth of 409 m, clearing the seafloor at 2215L, 30 August. The ship was moved in DP mode 15 m east and arrived at Hole 815B at 2227L, 30 August.

Hole 815B

High recovery in Hole 815A eliminated the need for a planned RCB hole. Thus, Hole 815B was cored to duplicate the upper part of the section using the APC. The new hole was located at 19°9.034′S, 149°59.524′E. Hole 815B was spudded at 2342L, 30 August, with the bit positioned at a water depth of 464.3 m from sea level. From Core 133-815B-1H, we recovered 7.94 m of sediment and placed the mud line at a water depth of 465.9 m from sea level. Continuous APC cores (Cores 133-815B-1H through -4H) were taken from 0 to 36.4 mbsf, with 36.4 m cored and 37.79 m recovered (103.8% recovery). We recalled the beacon; the bit cleared the seafloor at 1130L, 31 August.

The coring summary for Site 815 is presented in Table 1.

SITE GEOPHYSICS

JOIDES Resolution separated from the beacon at Hole 812C at 0845L (JD 238/2245 UTC), 27 August 1990, and began the 7-hr transit to Sites 815 and 816 (proposed Sites NEA-14 and NEA-13) at 0900L (JD 238/2300 UTC). A magnetometer was towed immediately after departure, and continuous bathymetric and magnetic data were recorded during the Line 3 transit, while heading about 160° across the Townsville Trough. The ship arrived at a position of 19°06.500′S and 150°00.602′E, about 5.5 nmi north of Site 816, at 1606L (JD 239/0606 UTC), ready to begin the site location survey.

Sites 815 and 816 lie in approximately 425 to 460 m of water on the northwestern margin of the Marion Plateau, adjacent to the southern flank of the Townsville Trough (Fig. 7), and about 56 km northwest of the Great Barrier Reef, about 220 km west of Marion Reef. These sites were selected to examine the effects of changes in eustatic sea level, paleoclimate, and paleoceanography on the development of Miocene and Pliocene carbonate platforms in both on- and off-platform settings. The area was first recognized as a potential ODP drilling target from a 1972 BMR sparker line (Line 13/058, Fig. 7). In 1987, the BMR vessel, *Rig Seismic*, was used to conduct a site survey at this location (Symonds and Davies, 1988; Feary et al., 1990) and about 94 km of 24-channel, 80-in.[3] water-gun, magnetic, and bathymetric data were collected on a grid of north-south and east-west lines (Figs. 7 and 8). The exact location of the two sites within this grid changed during planning of Leg 133 and during discussions with various JOIDES panels, particularly the Pollution Prevention and Safety Panel (PPSP). Both sites lie on intersecting seismic lines located by GPS navigation, but are not connected by a single site-survey track. Site 815 was positioned to recover current-reworked sediments in front of the earliest phase of the growth of the Marion Plateau carbonate platform, and Site 816 is on the edge of a small build-up thought to constitute one of the last phases of platform growth.

Table 1. Coring summary, Site 815.

Core no.	Date (Aug. 1990)	Time (UTC)	Depth (mbsf)	Length cored (m)	Length recovered (m)	Recovery (%)	Age (Ma)
Hole 815A							
1H	27	1450	0–6.8	6.8	6.80	100.0	
2H	27	1505	6.8–16.3	9.5	9.82	103.0	0.465–0.93
3H	27	1530	16.3–25.8	9.5	9.89	104.0	1.88–2.29
4H	27	1600	25.8–35.3	9.5	9.38	98.7	2.42–2.60
5H	27	1625	35.3–44.8	9.5	9.92	104.0	
6H	27	1700	44.8–54.3	9.5	10.14	106.7	2.6–3.45
7H	27	1725	54.3–63.8	9.5	9.84	103.0	2.6–3.45
8H	27	1745	63.8–73.3	9.5	9.53	100.0	3.51–3.88
9H	27	1830	73.3–82.8	9.5	10.06	105.9	3.51–3.88
10H	27	1900	82.8–92.3	9.5	9.95	105.0	3.51–3.88
11H	27	1925	92.3–101.8	9.5	9.97	105.0	3.51–3.88
12H	27	1950	101.8–111.3	9.5	10.01	105.3	3.51–3.88
13H	27	2015	111.3–120.8	9.5	9.96	105.0	3.51–3.88
14H	27	2100	120.8–130.3	9.5	9.99	105.0	3.51–3.88
15H	27	2125	130.3–139.8	9.5	10.03	105.6	3.51–3.88
16H	27	2145	139.8–149.3	9.5	10.13	106.6	3.51–3.88
17H	27	2210	149.3–158.8	9.5	8.60	90.5	
18H	27	2235	158.8–168.3	9.5	10.13	106.6	3.51–3.88
19H	27	2310	168.3–177.8	9.5	7.75	81.6	3.51–3.88
20H	27	2340	177.8–187.3	9.5	9.81	103.0	3.51–3.88
21H	28	0005	187.3–196.8	9.5	9.27	97.6	3.51–3.88
22H	28	0030	196.8–206.3	9.5	9.97	105.0	
23H	28	0140	206.3–215.8	9.5	8.71	91.7	
24H	28	0140	215.8–225.3	9.5	9.73	102.0	
25H	28	0230	225.3–225.8	0.5	0.33	66.0	3.88–4.6
26X	28	0330	225.8–232.2	6.4	7.13	111.0	
27X	28	0435	232.2–241.8	9.6	9.39	97.8	3.88–4.6
28X	28	0520	241.8–251.5	9.7	9.90	102.0	
29X	28	0610	251.5–261.2	9.7	9.30	95.9	3.88–4.6
30X	28	0705	261.2–270.8	9.6	9.98	104.0	3.88–4.6
31X	28	0750	270.8–280.5	9.7	9.91	102.0	
32X	28	0835	280.5–290.2	9.7	9.35	96.4	
33X	28	0935	290.2–299.9	9.7	6.08	62.7	
34X	28	1030	299.9–309.6	9.7	9.80	101.0	
35X	28	1155	309.6–319.3	9.7	9.45	97.4	
36X	28	1335	319.3–329.0	9.7	9.63	99.3	4.24–5.26
37X	28	1510	329.0–338.7	9.7	9.89	102.0	4.6–5.06
38X	28	1700	338.7–348.4	9.7	9.89	102.0	4.6–5.06
39X	28	1855	348.4–358.1	9.7	6.78	69.9	5.26–5.6
40X	28	2115	358.1–367.8	9.7	9.67	99.7	5.25–5.6
41X	29	0100	367.8–377.4	9.6	9.70	101.0	
42X	29	0340	377.4–387.1	9.7	10.02	103.3	5.6–5.9
43X	29	0540	387.1–396.4	9.3	9.76	105.0	
44X	29	0745	396.4–406.0	9.6	8.71	90.7	5.9–6.74
45X	29	0950	406.0–415.7	9.7	3.59	37.0	5.9–6.74
46X	29	1155	415.7–425.3	9.6	1.25	13.0	
47X	29	1345	425.3–434.9	9.6	5.17	53.8	
48X	29	1515	434.9–444.5	9.6	1.10	11.4	
49X	29	1625	444.5–454.2	9.7	0.00	0.0	
50X	29	1715	454.2–463.8	9.6	0.20	2.1	
51X	29	1810	463.8–473.5	9.7	0.00	0.0	
Coring totals				473.5	415.37	87.7	
Hole 815B							
1H	29	1355	0–7.9	7.9	7.94	100.0	
2H	29	1405	7.9–17.4	9.5	9.99	105.0	
3H	29	1420	17.4–26.9	9.5	9.99	105.0	
4H	29	1435	26.9–36.4	9.5	9.87	104.0	
Coring totals				36.4	37.79	103.8	

Note that times are given in Universal Time Coordinated or UTC, which is 10 hr later than local time.

An important requirement of Leg 133 site-location surveys was that the seismic records obtained on the *JOIDES Resolution* be as close as possible in appearance to those collected during the 1987 site surveys by the *Rig Seismic*, thus reducing ambiguity in site definition and when comparing the seismic stratigraphy of the two data sets. Accordingly, the *JOIDES Resolution* seismic deployment systems were modified.

Because both Sites 815 and 816 lie within the same site-survey grid and are less than 6 km apart, we decided to conduct site-location surveys for these sites at the same time. This survey was designed to confirm the proposed positions of the sites on *JOIDES Resolution* seismic data collected along a *Rig Seismic* track and then to obtain a seismic line that directly connected the two sites. Following the survey, the sites were to be relocated using confirmed GPS coordinates, and a beacon was to be dropped while maneuvering onto the location using the dynamic positioning system of the *Resolution*. We expected that this method would allow us to position the vessel's moonpool over the sites accurately. We knew that

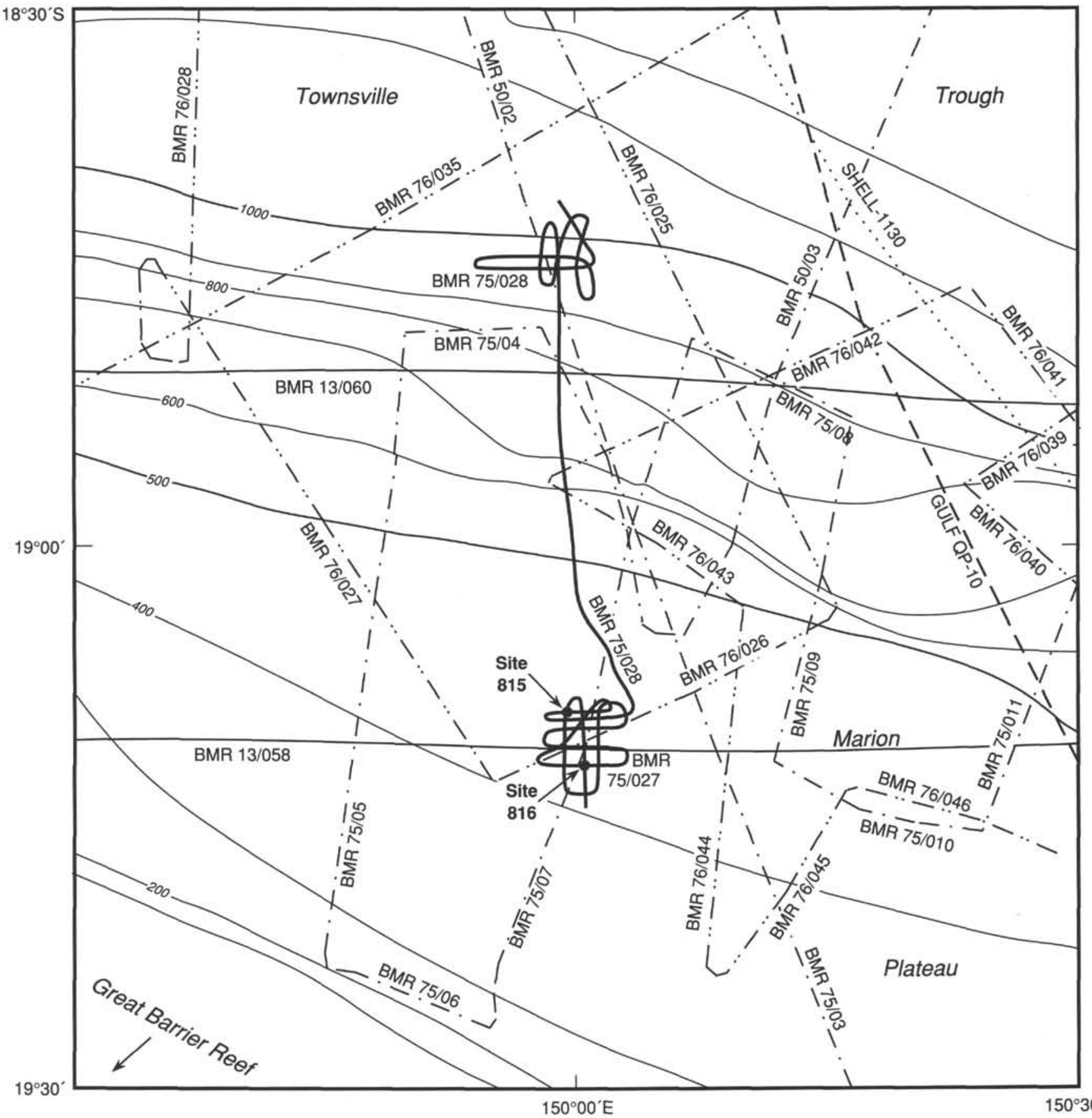

Figure 7. Track chart showing distribution of regional seismic data in area around Sites 815 and 816 (simplified bathymetry in meters).

accurate site positioning was extremely important for fulfilling the objectives of Site 816, where only tens of meters leeway occurred in the position for drilling the flank of the youngest carbonate bank (as recommended by the PPSP) or completely missing the feature.

Distribution of regional seismic data in the area around the sites is shown in Figure 7, and tracks of the original *Rig Seismic* site survey and the *JOIDES Resolution* site-location survey are shown in Figure 8. Following a reduction in ship's speed to 5 kt, the *JOIDES Resolution*'s single-channel seismic profiling system was deployed, and seismic recording began at JD 239/0620UTC, 27 August 1990, in calm seas (Beaufort Scale force 2). The *JOIDES Resolution* initially sailed south across Site 816 and then north across Site 815 to confirm GPS positions; she then turned to the west and sailed on a heading of about 160°, tying the two sites together (Fig. 8). Seismic acquisition was stopped, and equipment retrieved, at JD 239/1000UTC, 27 August 1990. About 31 km of seismic and magnetic data were collected during the survey. Signals from four GPS satellites were received throughout the survey, and we consider that the ship's track was positioned accurately. Seismic equipment operated well, except for substantial misfiring between the two 80-in.^{3} water guns during the first 15 to 20 min of the survey, and some streamer-induced noise appears on our southerly-heading lines, apparently the result of a following (southerly)

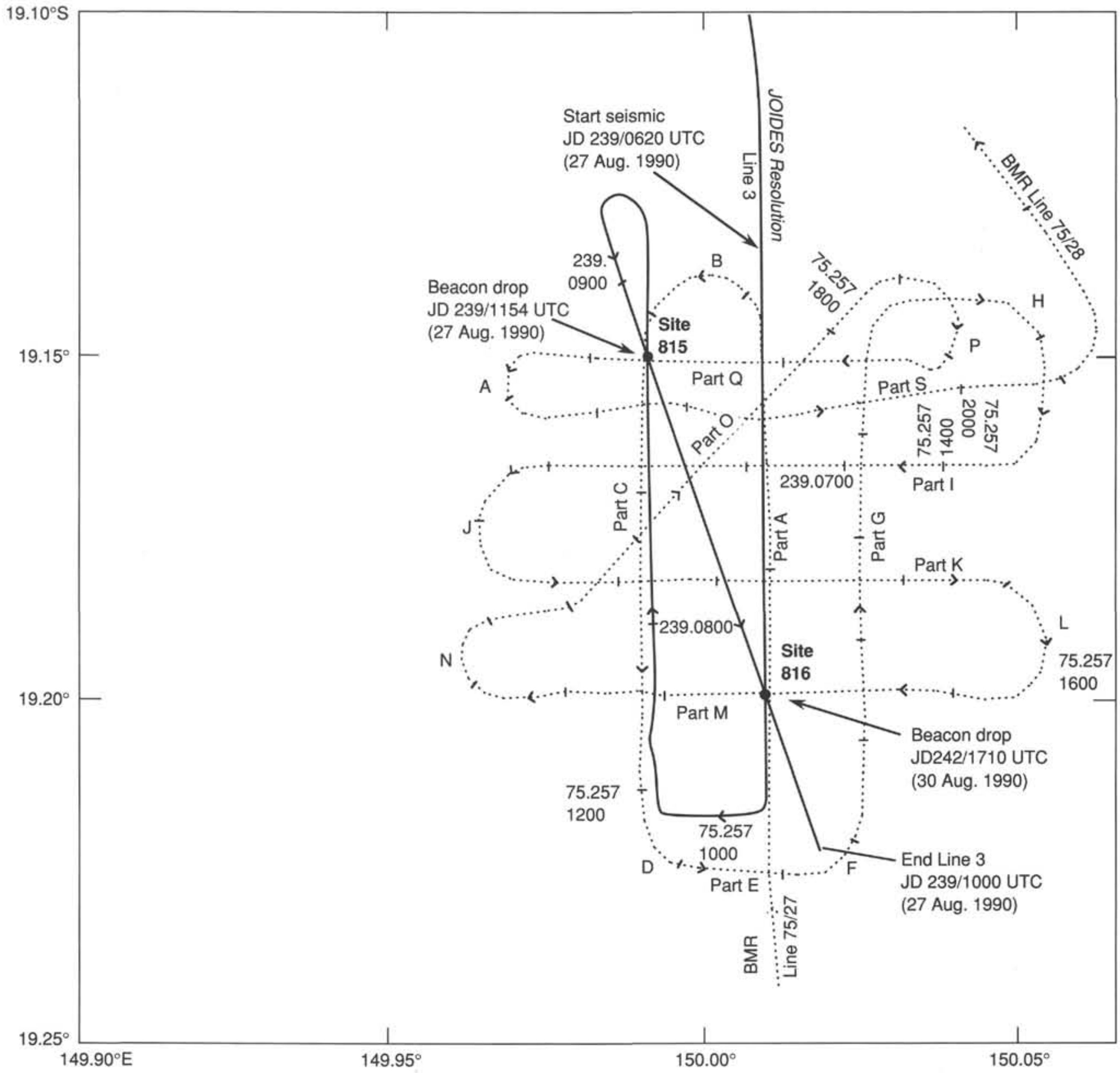

Figure 8. *JOIDES Resolution* Leg 133 site location tracks (solid line) and *Rig Seismic* 1987 site-survey tracks (dotted line) around Sites 815 and 816.

current. In general, shipboard analog records of good quality were obtained (Fig. 9), and excellent correlation existed at both sites between the *Rig Seismic* and *JOIDES Resolution* seismic profiles (Fig. 10; see Fig. 4, "Site 816" chapter, this volume), as well as the vessels' respective GPS positions.

Following the site-location survey, the *JOIDES Resolution* returned to the confirmed GPS position of Site 815 at JD 239/1050UTC on 27 August 1990. Her thrusters were lowered and final positioning of the ship over the site was achieved using dynamic positioning. A beacon was dropped at JD 239/1154UTC; final coordinates of Hole 815A are 19°9.034′S, 149°59.508′E, in a water depth of 465.5 m (drill-pipe measurement [DPM] from sea level).

Site 815 is the most northerly site of the two locations (Sites 815 and 816) on the northern Marion Plateau, and was positioned in front of a carbonate platform (Fig. 9). Good correlation at the site was found between the intersecting *JOIDES Resolution* single-channel seismic profiles and the *Rig Seismic* multichannel seismic profiles (Fig. 10). Basement is not visible on the water-gun data across the site owing to multiple reflections, which could not be removed by processing from the BMR multichannel data because of the short (450 m) streamer used during the site survey; however, normal resolution air-gun seismic data in the area indicate that basement is about 1.15 s two-way traveltime (TWT) below seafloor. Site 815 is underlain by an upper, thin (0.07 s TWT; 60 m) (?)pelagic drape sequence and overlies a relatively thick (0.28 s TWT; 250 m), onlapping and downlapping (?)contourite unit (Figs. 9 and 10). The underlying unit is about 0.09 s TWT thick (100 m) and contains a basinal

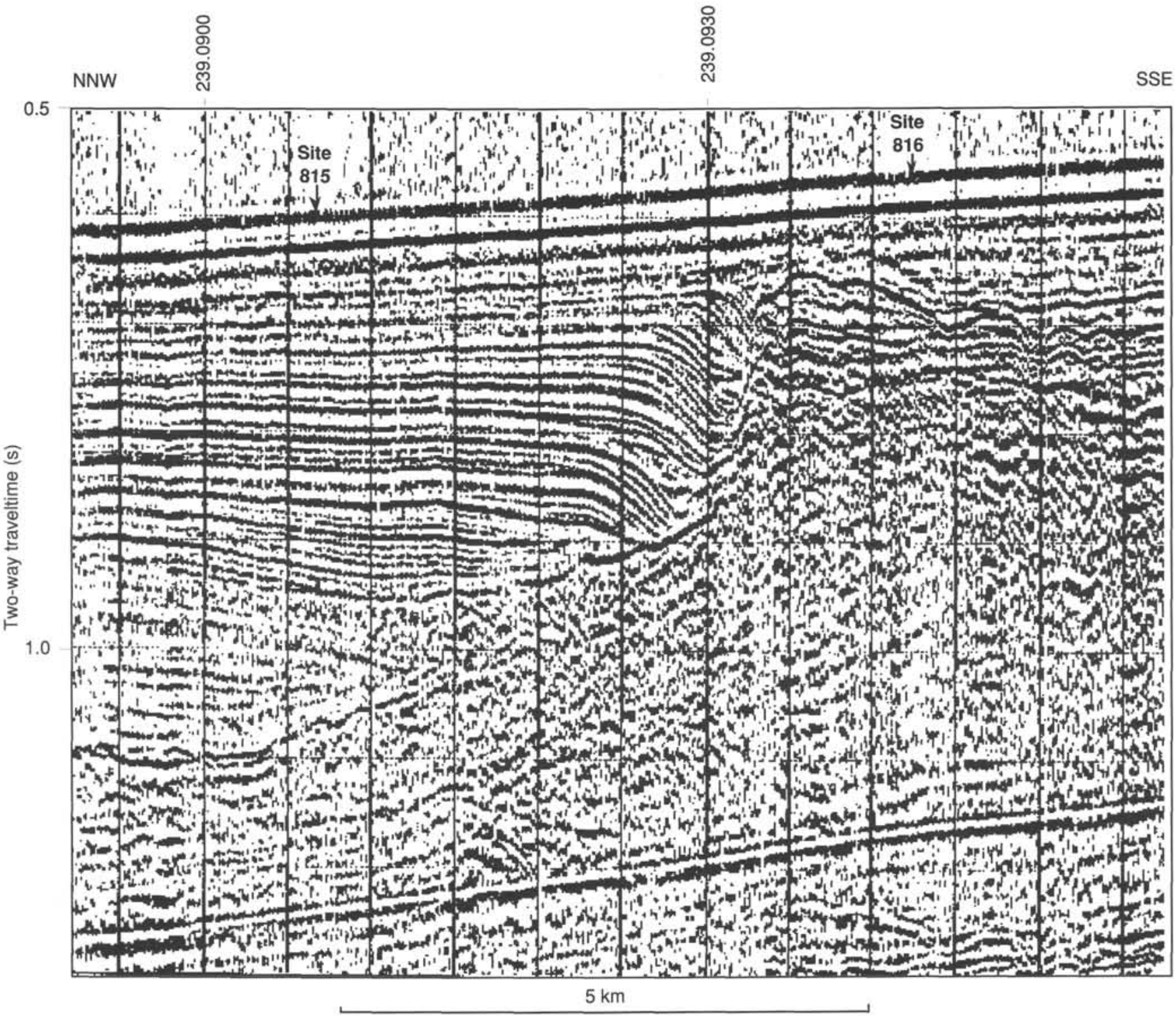

Figure 9. *JOIDES Resolution* shipboard analog single-channel seismic profile collected during Sites 815/816 site-location survey using two 80-in.^{3} water guns. The profile represents a seismic tie between the two sites.

facies that thickens away from the platform and an interfingering facies having a disrupted and contorted reflection configuration that thickens toward the platform margin. This latter facies and a similar seismic facies at and below TD were interpreted (pre-drilling) as representing distal, carbonate-platform debris aprons or foot-of-slope facies.

To provide some predictive capability during drilling at Site 815, we estimated the TWT/depth relationship below the seafloor, using stacking-derived interval velocities from the BMR site-survey seismic lines across the site, as well as from 1987 BMR air-gun data in the area. In Figure 11, this relationship is compared with similarly derived TWT/depth relationships for other off-platform sites on the Queensland Plateau (Sites 811, 813, and 814) and for DSDP Site 209 (Andrews, 1973). The section at Site 815 has a velocity that is intermediate between the lower-velocity section of DSDP Site 209, which is more than 100 km from a carbonate platform, and the higher-velocity platform margin sites (Sites 813 and 814).

LITHOSTRATIGRAPHY

Site 815 is situated along the southern margin of Townsville Trough, about 3 km north of a buried Miocene carbonate margin that underlies the western Marion Plateau (see "Principal Results" section, this chapter). Two holes were drilled at this site: Hole 815A reached 473.5 mbsf and Hole 815B was terminated at 36.4 mbsf (Fig. 12). In Hole 815A, APC coring was replaced by XCB at about 226 mbsf (Core 133-815A-26X).

Drilling disturbance with the XCB was prevalent below Section 133-815A-26X-5 through Core 133-815A-32X and was manifested by alternating hard and soft intervals approximately 8 to 10 cm apart (see core photographs). Discrete drilling biscuits or blocks of chalk are separated by darker, unlithified homogeneous to locally convoluted, laminated sands below about 290 mbsf (e.g., Core 133-815A-33X). Figure 13 shows how we reconstructed burrows and a pyrite vein by moving together adjacent biscuit edges and illustrates that these biscuits are artifacts of drilling. However, in some

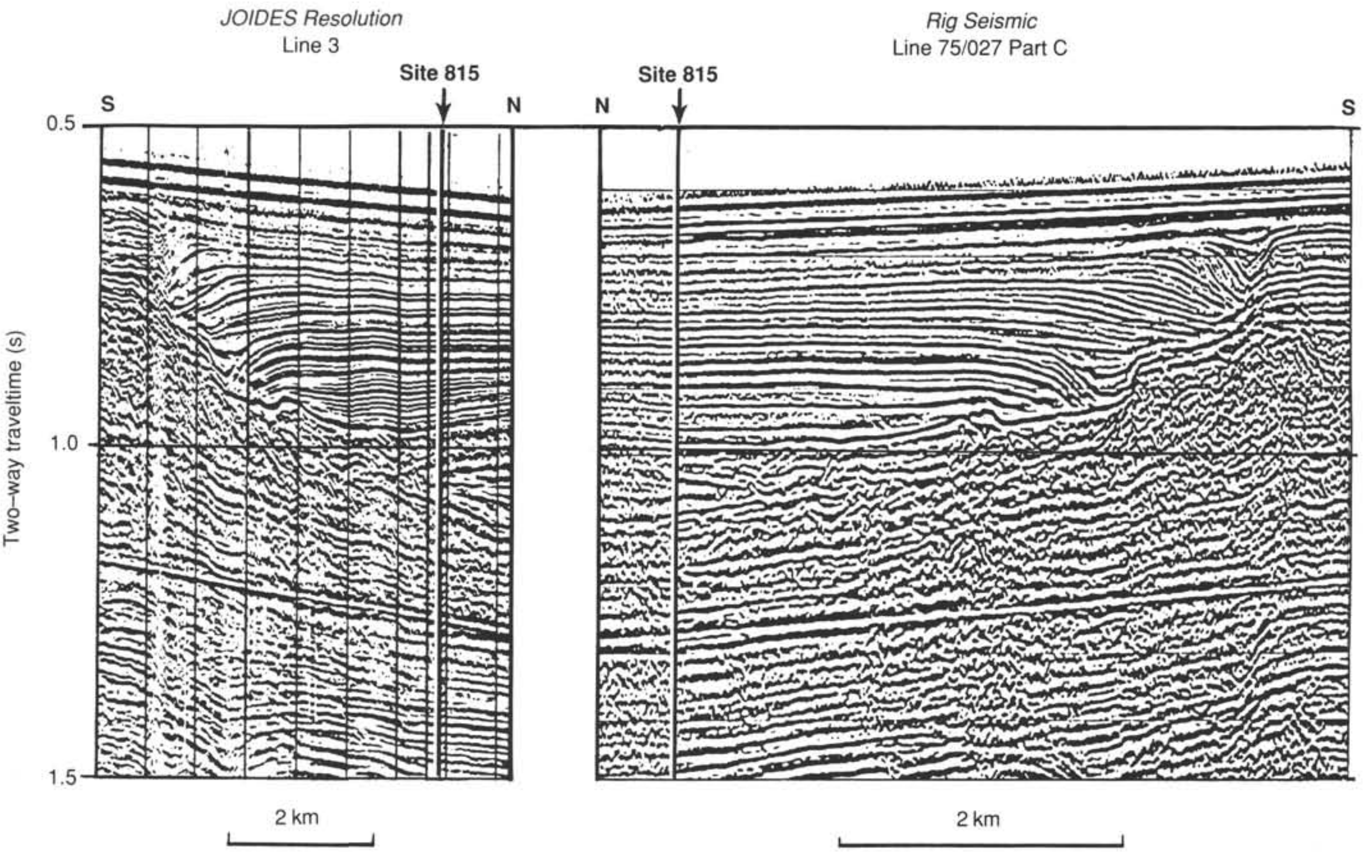

Figure 10. Comparison of *JOIDES Resolution* and *Rig Seismic* 80-in.^{3} water-gun seismic profiles across Site 815.

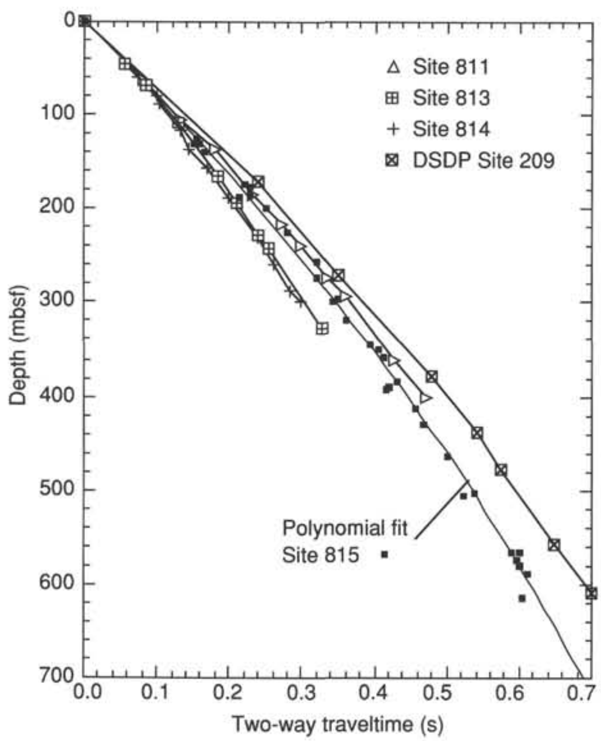

Figure 11. Comparison of TWT/depth curves estimated for Site 815 with those for Sites 811, 813, and 814, and DSDP Site 209 on Queensland Plateau.

cores, several burrows near the top of a given chalk biscuit have been filled with lithified sediment of similar lithology as the soft interbiscuit, suggesting that some drilling disturbance may have been influenced by lithologic variation.

Lithologic Units

Lithologic units have been defined and, in places, further subdivided by changes in color, carbonate content, fossil constituents and their relative abundance, lithification, and structure. Several of the lithologic boundaries coincide well with seismic sequence boundaries (Fig. 14). Six lithologic units were identified (Fig. 12); only part of the uppermost unit was penetrated in Hole 815B. Five major lithologies were encountered: (1) foraminifer nannofossil ooze with little or no clay (Subunit IA); (2) nannofossil ooze with clay to clayey nannofossil mixed sediment (Subunit IB through Unit II), documenting considerable variation in clay content (up to 60%); (3) nannofossil chalk with evidence of slumping (Unit III); (4) foraminifer nannofossil chalk to nannofossil foraminifer chalk, showing preservation of a densely distributed burrows (Unit IV); and (5) dolomitized foraminifer packstone to rudstone (Units V and VI).

Unit I (Sections 133-815A-1H-1 through -8H-CC and 133-815B-1H-1 through -4H-CC; depth, 0–73.3 mbsf; age, Pleistocene to late early Pliocene)

In Holes 815A and 815B, Unit I is predominantly foraminifer nannofossil to nannofossil foraminifer ooze, with color that alternates from white to pale brown and shades of gray, coincident with variation in clay content and bioturbation. Unit I can be subdivided on the basis of color and clay content.

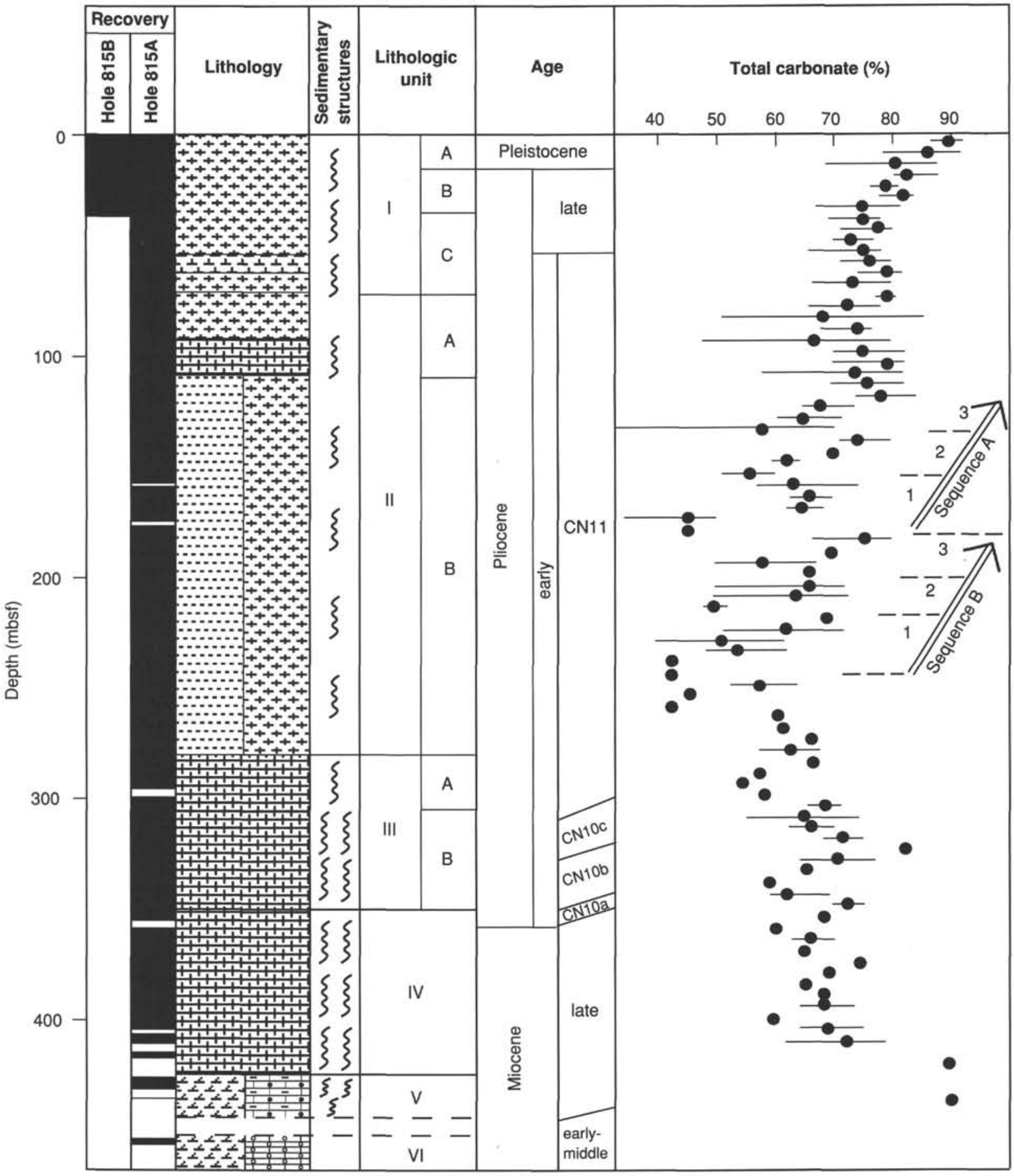

Figure 12. Lithostratigraphy, age, core recovery (cross-hatched = 100%), and total carbonate for Site 815. See text for further explanation; key to lithologic patterns appears in "Explanatory Notes" chapter (this volume).

Subunit IA (Sections 133-815A-1H-1 through -2H-CC and 133-815B-1H-1 through -2H-CC; depth, in Hole 815A, 0–16.3 mbsf; in Hole 815B, 0–17.4 mbsf; age, Pleistocene)

This subunit is predominantly foraminifer nannofossil to nannofossil foraminifer ooze having varying amounts of micrite and bioclast debris, and a total carbonate content commonly >85% (Fig. 12; see "Inorganic Geohemistry" section, this chapter). A well-defined repetitive (40–50 cm intervals) and alternating color variation (white to pale brown or gray) is found in Core 133-815A-1H, which becomes less well-defined and more patchy downward by Core 133-815A-2H. This may result from either increased clay content and/or increased mixing of sediment by bioturbation. A similar variation between white and pale brown ooze occurs in Hole 815B. Carbonate mineralogy is predominantly low-Mg calcite with aragonite below 20% and minor dolomite (<3%) over thin intervals (see "Inorganic Geochemistry" section, this chap-

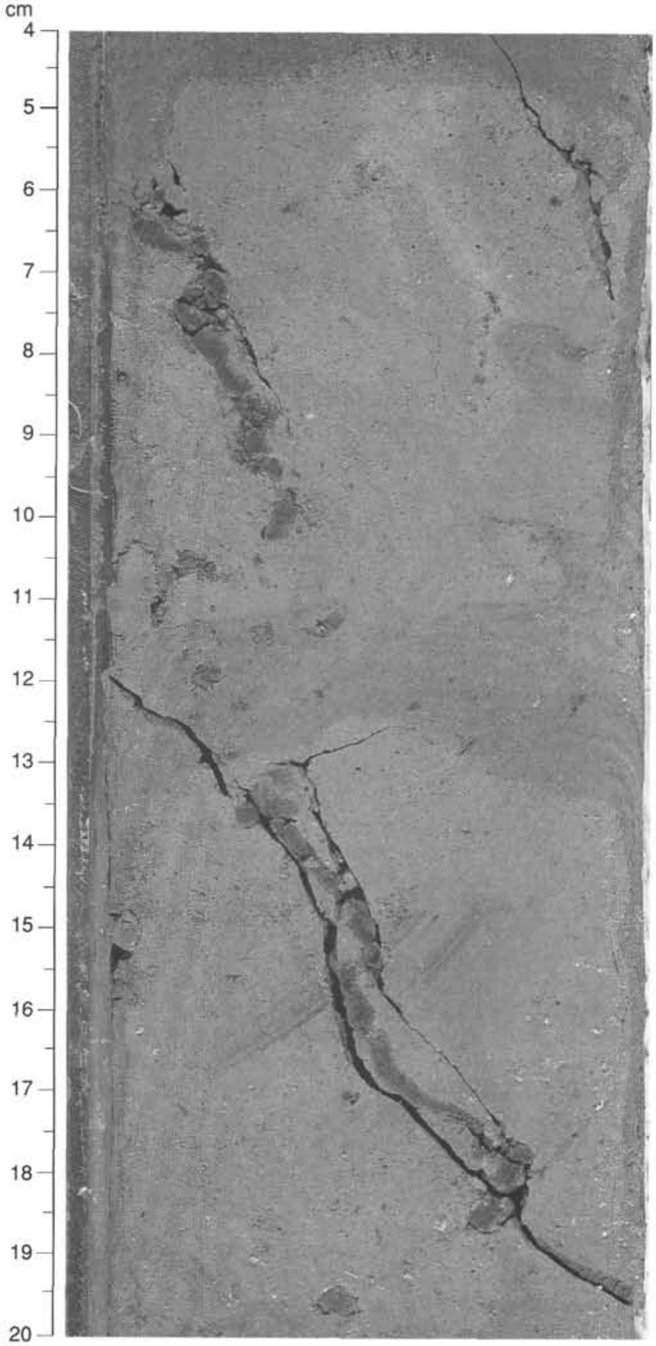

Figure 13. Drilling chalk "biscuits" separated by fluidized, homogeneous ooze in Unit III, from 4 to 20 cm in Section 133-815A-33X-4. The pyrite vein can be reconstructed across the ooze "interbed," thereby illustrating that biscuits are drilling artifacts.

ter). We are uncertain whether dolomite is authigenic or detrital.

Subunit IB (Sections 133-815A-3H-1 through -4H-CC and 133-815B-3H-1 through -4H-CC; depth, in Hole 815A, 16.3–35.3 mbsf; in Hole 815B, 17.4–36.4 mbsf; age, late late Pliocene)

This subunit differs from Subunit IA in having a carbonate content that is commonly about 80% and predominantly all low-Mg calcite with <10% aragonite and <2% dolomite. In addition, color varies over larger intervals (about 60–80 cm thick) and is commonly patchy in distribution. From 26 to 110 cm in Section 133- 815A-4H-6, a change to darker colored sediment is associated with a predominance of nannofossil ooze. This suggests that an association may exist with change in grain size, in contrast to the lighter nannofossil foraminifer ooze above and below this interval.

Subunit IC (Sections 133-815A-5H-1 through -8H-CC; depth, 35.3–73.3 mbsf; age, early late Pliocene to late early Pliocene)

This subunit is separated from Subunit IB by a slight darkening of color to darker gray. Lithologically, the unit is similar to Subunit 1B and predominantly consists of nannofossil foraminifer to foraminifer nannofossil ooze. However, Core 133-815A-7H contains nannofossil ooze. This subunit contains clay percentages that vary from about 83% to 67%, and carbonate mineralogy comprises aragonite (<5%–20%), dolomite (<8%), and the remainder is low-Mg calcite.

Unit II (Core 133-815A-9H through Section 133-815A-31X-CC; depth, 73.3–280.5 mbsf; age, early Pliocene)

This unit represents an expanded lower Pliocene section and consists predominantly of homogeneous to slightly bioturbated, nannofossil ooze to unlithified nannofossil mixed sediment. Chalk and lithified mixed sediment are locally present. The unit varies in color from greenish-gray to gray, with subtle to marked alternating light- to darker-colored intervals. Boundaries between these intervals are abrupt to commonly transitional. Each color unit is on the order of 60 to 100 cm thick, but considerable variation occurs. Changes in color may be related to variation in grain size and/or carbonate content. Within a dark greenish-gray zone at 90.3 mbsf, the percentage of total organic carbon is about 1%, which is coincident with a slightly reduced carbonate content (see "Organic Geochemistry" section, this chapter). Percentages of carbonate content exhibit considerable intersample variation (up to 55%), superimposed on an overall decrease downward between about 70% to 80% and 40% to 60% from 100 to 280 mbsf (Fig. 12; see "Inorganic Geochemistry" section, this chapter). Carbonate mineralogy comprises aragonite (<25%), dolomite (commonly <15%), and low Mg-calcite to about 230 mbsf, the depth at which aragonite disappears. Smear slide analyses suggest that aragonitic needles occur in Unit II; however, the origin of the aragonite requires much more work. This unit can be subdivided on the basis of the state of lithification and on varying percentages of foraminifers and nannofossils.

Subunit IIA (Sections 133-815A-9H-1 through -12H-CC; depth, 73.3–111.3 mbsf; age, early Pliocene)

This subunit is characterized by soft to very firm, dark gray to gray, foraminifer nannofossil and nannofossil foraminifer ooze and appears to mark the top of the clay-rich lower Pliocene section (in comparison to lower clay content in the overlying Subunit IC). Bioclasts and quartz also are present. Thin patchy chalk to lithified intervals occur in Cores 133-815A-11H and -12H. Carbonate content generally ranges from 70% to 80%; black monosulfides(?) occur as specks to tiny patches (<few millimeters to 1 cm) throughout the section. Some burrows are filled with foraminiferal packstones that contain both benthic and planktonic forms; black monosulfides occur both as stains and void-fill precipitates within foraminifer tests.

Subunit IIB (Cores 133-815A-13H through -31X; depth, 111.3–280.5 mbsf; age, early Pliocene)

This thick interval is dominated by dark to light greenish-gray to varying gray nannofossil ooze with clay to clayey

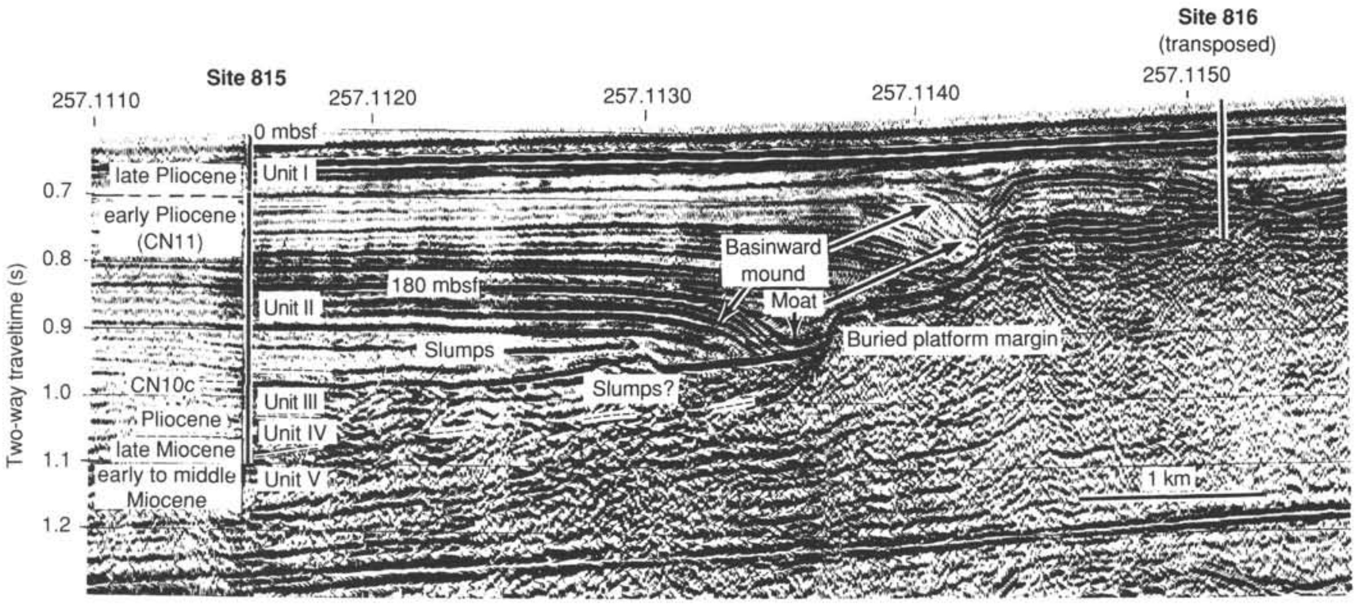

Figure 14. Seismic reflection profile (ODP Line 75/027) from Sites 815 to 816 showing basin-to-platform change in seismic sequence geometry. Basinward mounds and moats are evident along the abrupt change in paleobathymetry associated with the paleomargin between the two sites. Several near parallel reflectors at Site 815 coincide with lithologic boundaries and changes in carbonate content within Unit II. Reflector at 180 mbsf coincides with the boundary between two depositional sequences displaying upward increases in carbonate content (see Fig. 12).

nannofossil mixed sediment. Local partial lithification takes place within this subunit. Downward color variation in light to dark intervals is apparent (e.g., Cores 133-815A-19H and -20H); boundaries between color variations are abrupt, bioturbated, and transitional. As considerable intersample variation in carbonate content occurs (up to 60%, Fig. 12; see "Inorganic Geochemistry" section, this chapter), color variation suggests a repetitive to even cyclic control of carbonate content. At this time, control is indeterminate. Foraminifer-filled burrows (stained with monosulfides) and specks to patches of monosulfides occur throughout the section. Burrow fills of foraminifer packstone with benthic and planktonic forms are present, although generally these have been sparsely distributed. Sand- to gravel-size fragments of pelecypod shells (<1–2 mm) are scattered throughout the subunit. Some are friable and break into lustrous sheets, which suggests *in-situ* alteration and loss of structural integrity of the original aragonitic shell.

Unit III (Cores 133-815A-32X through -38X; depth, 280.5–348.4 mbsf; age, early Pliocene)

This unit is characterized by greenish-gray to gray chalks and lithified mixed sediment and by intervals of contorted and convoluted bedding that have been interpreted as slump features (Figs. 15 and 16). Clay content exceeds 60% at 131 and 172 mbsf, coincident with thin claystones that have been interbedded with the mixed sediment. Bioturbated textures become well preserved, or increase in abundance with depth within Unit III. Slump textures are not drilling disturbance, as shown by horizontal drilling-induced fractures that are filled with unlithified homogeneous calcareous muddy sand that crosscuts contorted bedding. The top of the most obvious structurally disturbed section (Subunit IIIB) occurs at 25 cm in Section 133-815A-34X-5. Mineralogy is predominantly low Mg-calcite, with dolomite percentages variable (up to 13%, but most often less than 5%).

Subunit IIIA (Core 133-815A-32X through Section 133-815A-34X-4; depth, 280.5–306.25 mbsf; age, early Pliocene)

This subunit contains foraminifer nannofossil and nannofossil foraminifer chalks. Burrow structures become more numerous, are better preserved, and locally display a greater density than those in overlying units. As such, better separation of this subunit is defined by changes in ichnofacies, rather than lithification. At this time, however, the contrast in lithification is an obvious boundary.

Successive intervals tens of centimeters thick display a common upward lithologic change from darker, clay-rich, nannofossil-dominated chalks to lighter, greenish-gray foraminifer-rich intervals. The boundary between light and dark sediment can be gradual or, in some examples, abrupt and well-bioturbated, which suggests a hiatus (Fig. 15). These transitions become better developed in this unit and in Unit IV. Carbonate content shows a marked increase, probably diagenetic and related to increased calcite cement across the Unit II/UNit III contact; however, the carbonate content is still only about 60% to 70%. Variations in percentage occur from a change of dark- to light-colored chalks and generally are higher in the chalks.

Subunit IIIB (from 25 cm in Section 133-815A-34X-5 through Core 133-815A-38X; depth, 306.25–348.4 mbsf; age, early Pliocene)

The top of this subunit coincides with the first obvious occurrence of contorted and convoluted bedding, which has been interpreted as a product of slumping (Fig. 16). The unit forms part of a regional seismic sequence, dish-shaped in one section, that contains wavy, discontinuous reflectors of variable amplitude; the sequence abuts part of the buried carbonate platform that underlies the Marion Plateau (Fig. 14). Subunit IIIB generally contains a slightly higher percentage of total carbonate (about 70%) than Subunit IIIA (Fig. 12).

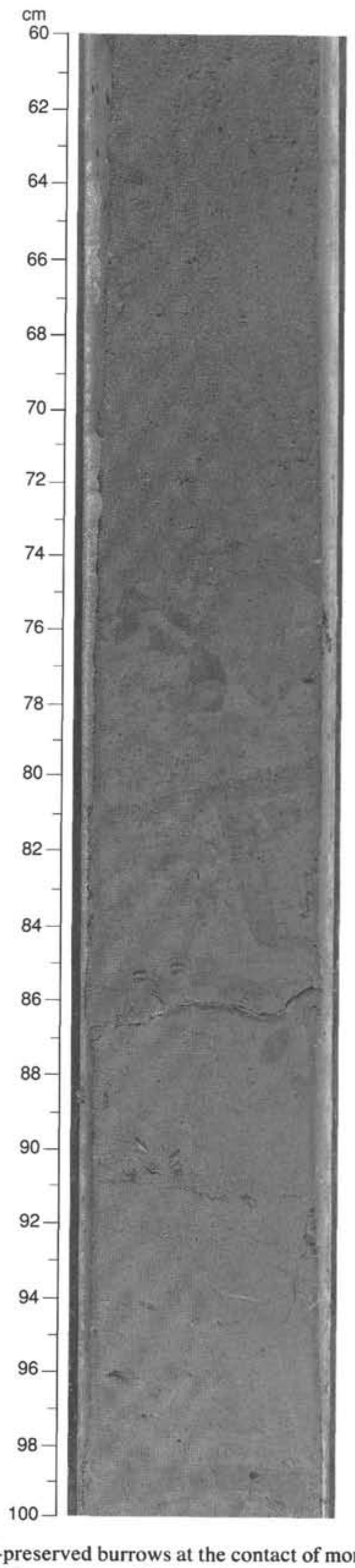

Figure 15. Well-preserved burrows at the contact of more argillaceous nannofossil chalk overlying lighter-colored, more carbonate-rich, nannofossil-foraminifer chalk; from 60 to 100 cm in Section 133-815A-34X-2 (Subunit IIIA). This contact (at about 305 mbsf) coincides with base of an interval about 30 m thick that displays an upward decrease in clay content (see Fig. 12).

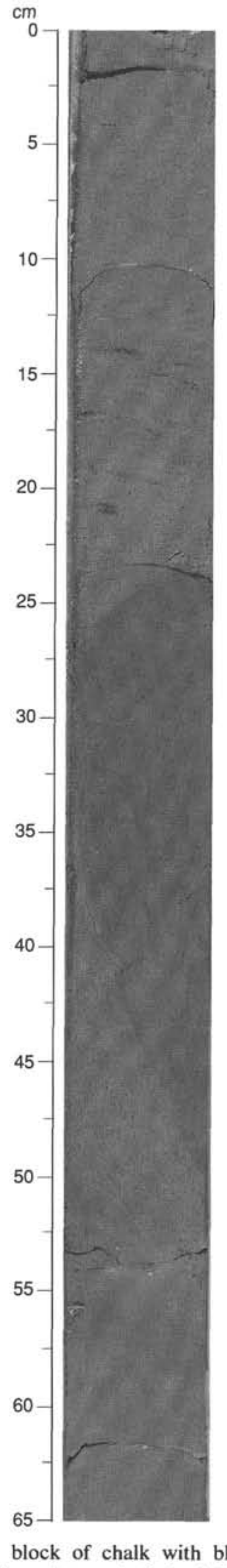

Figure 16. Slumped block of chalk with block (**A**) within sandy foraminifer lithoclastic packstone in Subunit IIIB; from 0 to 65 cm in Section 133-815A-34X-5. Contorted bedding also occurs in matrix sediment; both contorted and microfaulted bedding and laminations occur within the chalk block, indicating that slumping occurred during early lithification of the sediment.

At the upper boundary, at least one large (50-cm-thick) block of nannofossil foraminifer chalk occurs within a matrix of lighter, sandier, and in part laminated, partially lithified foraminifer packstone and chalk (Fig. 16). This lithology is similar to some of the drilling-disturbed interbiscuit sediments, but is equally as lithified (not fluidized) as the nannofossil chalk. The matrix bedding dips are up to 45° relative to core orientation.

Bedding within individual chalk blocks, excluding those that may have rotated within the core barrel, vary from horizontal to vertical; adjacent blocks in core may display markedly different bedding orientations (Fig. 17). In many blocks, a higher amplitude of folding and microfaults separating folds are superimposed on bedding trends. Many of these features, together with their stratigraphic juxtaposition, are good indicators of soft-sediment deformation during slumping or slide/glide transport along deep-water slopes of carbonate, mixed, and clastic sediments (see Pickering et al., 1989, p. 125). With superimposed drilling disturbance, however, one finds it difficult to delineate discrete slumped stratigraphic sections and their bounding slide or glide planes, or to determine whether the entire subunit has deformed internally during one slump event. Evidence for slumping is found at several depths: from 25 cm in Sections 133-815A-34X-5 through -34X-7; Section 133-815A-36X-2; and from Sections 133-815A-37X-4 through -37X-6. We placed Core 133-815A-38X in this lithologic unit because of the presence of possible convoluted slump structures in Section 133-815A-38X-3.

Unit IV (Sections 133-815A-39X-1 through -46X-CC; depth, 348.4–425.3 mbsf; age, late late Miocene to early early Pliocene)

This unit also is greenish-gray to gray in color and is predominantly a foraminifer nannofossil and nannofossil foraminifer chalk. Carbonate mineralogy is mostly low-Mg calcite with low (<8%) percentages of dolomite (see "Inorganic Geochemistry" section, this chapter); carbonate content varies between about 60% and 75%. The unit is characterized by an apparent increased preservation of bioturbated textures, in comparison to overlying units (Fig. 18). Recognized trace fossils include *Condrites*, *Zoophycos*, and *Planolites*, but others (indeterminate at this time) are also common. Burrows appear to increase in size with depth. In general, the unit is sandier than Unit III and is locally controlled by the abundance of foraminifers.

As in the above units, repetitive changes in lithology and color are controlled by varying percentages of foraminifers, nannofossils, and trace fossils. Carbonate content shows a downward profile similar to that in Subunit IIIB, with percentages of about 60% to 75% and a similar intersample variation associated with the short-interval variation in lithologic changes (as shown in Fig. 15). However, percentages of total organic carbon are slightly higher than in the above units, but still are only about 0.5%.

Unit V (Cores 133-815A-47X to -48X; depth, 425.3–444.5 mbsf; age, late Miocene)

This unit consists of mostly pale brown, calcareous to dolomitized, lithified foraminifer (small benthic and planktonic) packstones and minor chalk. Well-preserved and abundant trace fossils are present in the upper part of this unit. Mineralogy is predominantly low-Mg calcite (Fig. 19). With depth, the unit becomes more brownish-gray in color, while trace fossils become less abundant, and by Core 133-815A-48X the rocks are pale brown. In Sample 133-815A-48X-CC, a thin, subsucrosic dolomite occurs as a drilling biscuit within the base of suspected downhole contamination. Its true strati-

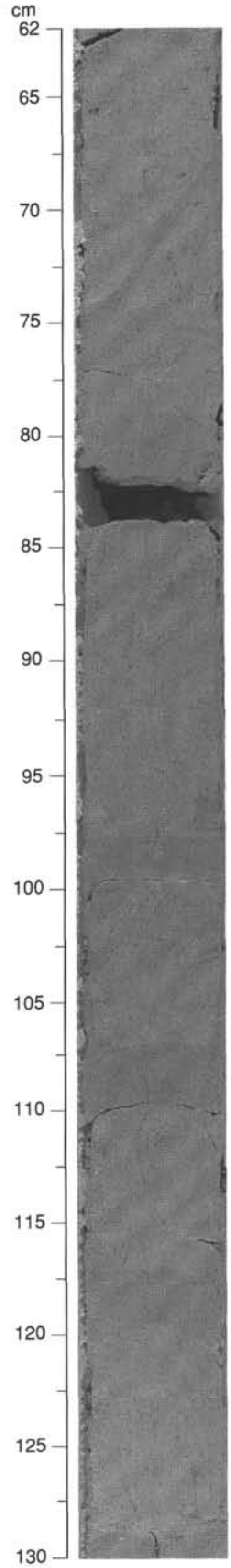

Figure 17. Variable orientations of bedding within slumped chalk in Subunit IIIB, from 62 to 130 cm in Section 133-815A-37X-3. Because of drilling disturbance, we do not know whether some of this fluidized interbiscuit ooze represents sediment deposited between discrete slump blocks.

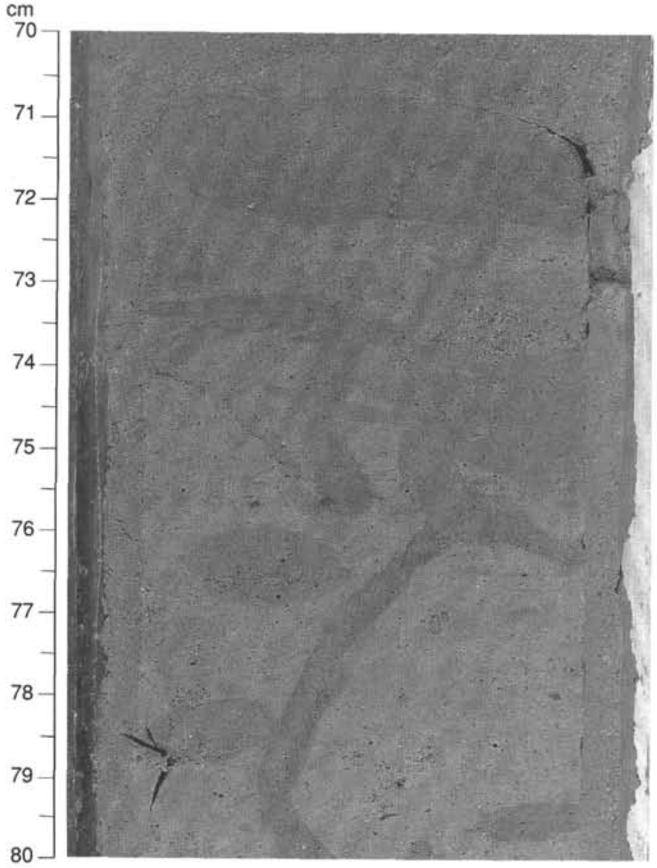

Figure 18. Well-bioturbated foraminifer nannofossil chalk in Unit IV, from 70 to 80 cm in Section 133-815A-41X-4.

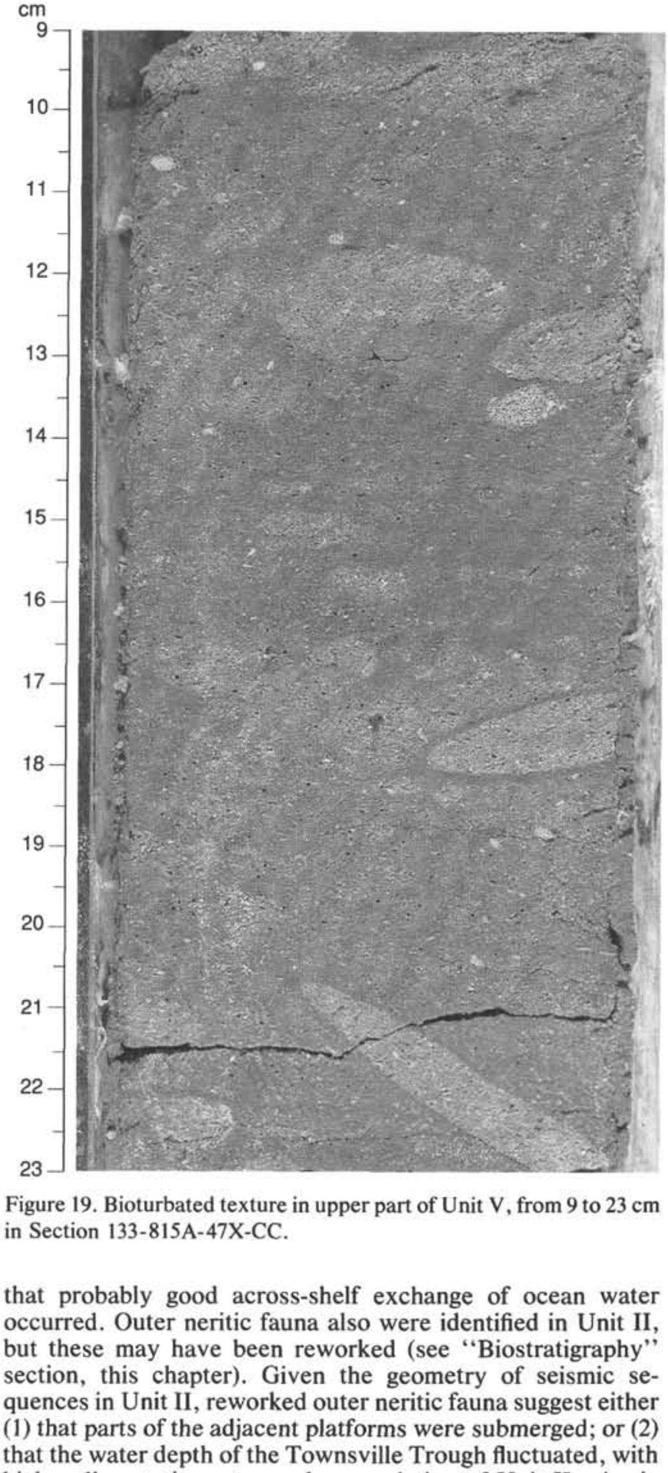

Figure 19. Bioturbated texture in upper part of Unit V, from 9 to 23 cm in Section 133-815A-47X-CC.

graphic or depositional relationship with Unit V is uncertain. In addition, because of poor core recovery in Core 133-815A-46X (13%), the top of this unit is tentatively placed at the top of Core 133-815A-47X. The upper part of this unit (Core 133-815A-47X) may represent a transition in lithology between Unit IV and the pale brown dolomites in the lower part. An algal rhodolith about 3 cm in diameter is present in Core 133-815A-48X. Porosity is about 5% to 10% and consists of intercrystalline (dolomite) cavities.

Unit VI (Section 133-815A-50X-CC only; depth, 454.2–463.8 mbsf; age, latest early to early middle Miocene)

A gap occurs between Units V and VI, represented by the unrecovered interval from 444.5 to 454.2 cm (i.e., Core 133-815A-49X was empty). This unit is represented only by Section 133-815A-50X-CC and consists of dolomitized, white benthic (large) foraminifer rudstones to floatstones within a foraminifer (planktonic) packstone. Porosity is about 5% to 10%, with cavities that form intercrystalline, intergranular, and intraskeletal pore spaces.

Depositional Environments and Processes

Benthic foraminifer assemblages from core-catchers in Units I through the middle of IV indicate a predominantly upper bathyal setting (see "Biostratigraphy" section, this chapter) to at least 370 mbsf. In Section 133-815A-45X-CC, near the base of Unit IV, outer neritic fauna were identified and considered *in-situ*. Sediments of Units V and VI also may have been deposited within a neritic setting. The abundance of planktonic foraminifers within these units suggests that such a setting possessed no barrier along the platform margin and that probably good across-shelf exchange of ocean water occurred. Outer neritic fauna also were identified in Unit II, but these may have been reworked (see "Biostratigraphy" section, this chapter). Given the geometry of seismic sequences in Unit II, reworked outer neritic fauna suggest either (1) that parts of the adjacent platforms were submerged; or (2) that the water depth of the Townsville Trough fluctuated, with high sedimentation rates and progradation of Unit II seismic sequences (Fig. 14) possibly permitting a periodic build-up of the muddy trough floor into shallow (<200 m) water.

A general change from outer neritic to upper bathyal (shelf to slope) may have occurred within Unit IV, an interval within which the greatest preservation of bioturbated textures occurred. Whether this represents only better preservation or a real increase in number of burrows, reflecting changes in food supply or bottom-water conditions, is unclear at this time. Slightly raised levels of organic carbon, compared with other units, might indicate a paleoenvironment in which a plentiful supply of food permitted a thriving bottom (epifauna and infauna) biologic community. Shifting zones of biologic activity in an outer-margin setting can be greatly influenced by the oxygen minimum zone (OMZ), with greatest biologic activity perhaps occurring along the edges of the OMZ (Mullins et al., 1985).

The expanded lower Pliocene, represented by Unit II to the top of Unit III and having sedimentation rates of >30 cm/k.y. (see "Sedimentation Rates" section, this chapter), is a spectacular component of the stratigraphy at Site 815. Sedimentation rates for the interval deposited during CN11 might have been as high as >80 cm/k.y. (or >800 m/m.y.). Within Subunit IIA, subtle-to-dramatic variations in carbonate content (Fig. 12) and lithology (variations in foraminifer and nannofossil percentages) together with increasing architectural complexity of individual seismic sequences toward the paleomargin (Fig. 14; see also "Seismic Stratigraphy" section, this chapter) underscore a history of complex sedimentation during a short geologic period (about 300,000 yr) of global highstands and lowstands of sea level (Haq et al., 1987). Equivalent-age sediments of at least the upper part of this unit also are found atop shallow-water lower Pliocene carbonates that were drilled at Site 816 (see "Site 816" chapter, this volume), which indicates that mixed carbonate-siliciclastic sediments of early to late Pliocene age abutted and eventually buried the paleomargin of the Marion Plateau in this region. An ancient analog for such an environment (including a similar green basinal sediment) is the upper Devonian (Frasnian) in the subsurface of Alberta, Canada, where the basinal Ireton Formation strata envelop and bury the platform (oil-producing) reefs of the Leduc Formation in a series of prograding and stacked depositional sequences (Stoakes, 1980).

At Site 815, only near-parallel seismic reflectors of high and low amplitudes characterize Unit II. A major reflector at about 180 mbsf (Fig. 14) may correspond with the boundary between two major depositional sequences that display upward-decreasing clay percentages (Fig. 12). However, each of these sequences consists of higher-amplitude fluctuations in carbonate content. Thus, accumulation of sediment within Unit II was characterized by changes in either clay influx, carbonate influx, or both. Tracing major reflectors at Site 815 toward the paleomargin (see Fig. 14) indicates an increasing complexity in seismic sequence architecture. At least three separate stages of deposition have probable moats and adjacent basinward sediment mounds. High sedimentation rates, the location and architecture of the seismic sequences adjacent to the paleomargin, and preliminary evidence for fluctuating clay/carbonate accumulations all suggest that Subunit IIB probably represents a muddy contourite (Pickering et al., 1989). A southeasterly directed ocean current, like the present East Australian Current, flowing along the Queensland Trough might have transported at high rates both planktonic carbonates and fine-grained terrigenous detritus as a suspended or saltating load. Sedimentation and scouring should have occurred where the current was forced to change direction (establishing a lower velocity) to the east, along the paleomargin of the Marion Plateau.

Parts of Unit II may document deposition during the subsequent rise in sea level toward the end of CN11 (Haq et al., 1987) or a rise related to increased rates of subsidence. Certainly, the series of seismic sequences formed during CN11 illustrate high-frequency control of sedimentation, although whether eustatically or tectonically (subsidence) controlled is uncertain. However, using the subsurface Ireton Formation as an analogy, the stacked seismic sequences may reflect preferential deposition of clay-rich intervals during short-term relative stillstands, with the bounding reflectors (unconformities) marking subsea erosional surfaces or hardgrounds (Stoakes, 1980). Hiatal surfaces marked by burrowed carbonate-rich sediment, as shown in Figure 14, clearly illustrate that clay/carbonate influx was shut on and off.

Evidence for the middle-to-upper part of Unit II as having been deposited during relative increases in sea level may come from the overall upward decrease in clay content (see Fig. 12) and by the presence of aragonite between 0 and 230 mbsf. Although fragments of pelecypod shells in this unit may provide trace amounts of aragonite, what appear to be aragonitic needles are present in many smear slides in Unit II. Aragonite might have been derived from three sources: (1) still submerged upper-slope settings along emergent platform tops; (2) submerged platform tops; and (3) eroded from emergent platforms juxtaposed to the Townsville Trough. Further work will require examination in detail of the aragonite detritus and placement within the regional framework of the history of sea level for this area of the Australian margin.

BIOSTRATIGRAPHY

Common-to-abundant, upper Pleistocene through upper Miocene, calcareous microfossils were recovered from 0 to 445 mbsf; the sequence has an extremely expanded lower Pliocene section (~300 m). Preservation of microfossils is generally good in this sequence, which contributed to good, high-resolution biostratigraphy for Hole 815A. Preliminary biostratigraphy and some paleoenvironmental information for Hole 815A are provided in this section.

Calcareous nannofossils indicate that the Pliocene/Pleistocene contact is within Core 133-815A-2H. Three nannofossil subzones can be recognized in the upper Pliocene. The lower Pliocene/upper Pliocene contact (as recognized from nannofossil data) is found in Core 133-815A-8H, which agrees in general with planktonic foraminifer data. Four nannofossil zone/subzones were identified in the lower Pliocene section. The Miocene/Pliocene contact, indicated by nannofossil markers, was observed in Core 133-815A-39X, which is slightly higher than suggested by planktonic foraminifers (in Core 133-815A-41X). (This discrepancy is inherent in inadequate cross-correlation of planktonic foraminifers and nannofossil biostratigraphies.)

Reliable age control is available down to Core 133-815A-48X, which yielded common calcareous nannofossils having an age range of 5.9 to 8.2 Ma (CN9a, late Miocene; Fig. 20). No sediment was recovered in Core 133-815A-49X. Core 133-815A-50X yielded abundant benthic foraminifers and some planktonic foraminifers, which constrain the core's age to the late early Miocene–early middle Miocene. Core 133-815A-51X, the last core of the hole, had no core recovery.

Benthic foraminifers from the upper lower Miocene–lower middle Miocene (Sample 133-815A-50X-CC, the lowest sample available from this hole) have poor preservation and contain no depth-diagnostic taxa. However, an assemblage from the upper Miocene (in Sample 133-815A-45X-CC) indicates an outer neritic environment. Above Core 133-815A-45X, all core-catcher samples examined yielded upper bathyal foraminiferal assemblages, with some neritic elements present in several samples (Samples 133-815A-15H-CC, -20H-CC, and -23H-CC). The presence of these neritic taxa in the otherwise typical upper bathyal assemblages may be the result of downslope transport (as turbidites), because their occurrences correspond to intervals of low abundances of nannofossils (see "Sedimentation Rates" section, this chapter, Fig. 21).

Calcareous Nannofossils

Site 815 yielded abundant upper Pleistocene through upper Miocene calcareous nannofossils from the seafloor to 445

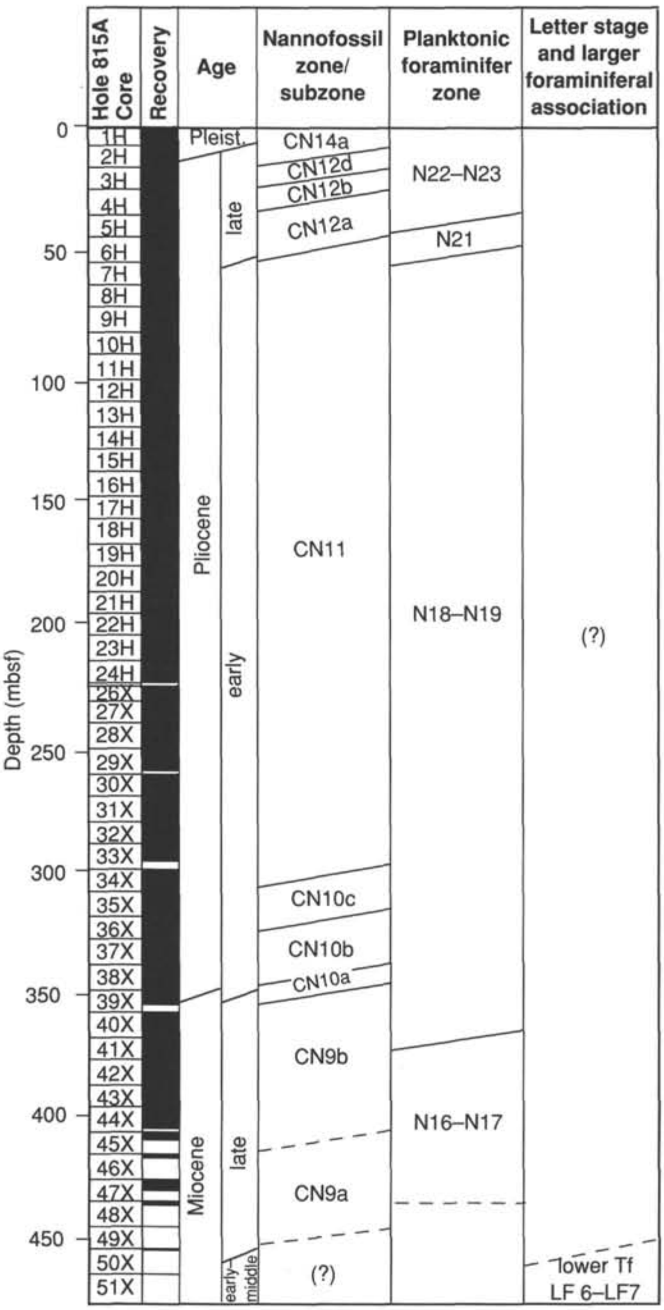

Figure 20. Preliminary nannofossil and foraminifer biostratigraphy, Hole 815A.

mbsf. Preservation of nannofossils is generally good, especially in the expanded lower Pliocene and upper Miocene intervals (54–406 mbsf), in which nannofossils are preserved in pristine condition in many of the samples examined. No sediments were taken from the last core of the hole (Core 133-815A-51X), and the two preceding cores (Cores 133-815A-49X and -50X) yielded few nannofossils, none of which were age-diagnostic species. Consequently, the oldest sediments penetrated in the hole cannot be dated with nannofossil markers; however, these sediments must be older than 5.9 Ma (late Miocene), the youngest age possible for Core 133-815A-48X above the undated interval. A brief summary of the nannofossil biostratigraphy at Site 815, based on examination of mainly core-catcher samples, is given next.

Samples 133-815A-1H-CC and -2H-CC yielded *Pseudoemiliania lacunosa* and *Gephyrocapsa caribbeanica*, among other upper Pleistocene species, and can be assigned to Subzone CN14a (0.465–0.93 Ma). Sample 133-815A-3H-CC contains *Discoaster brouweri* but no *D. pentaradiatus* or other species of *Discoaster* and has been placed in the uppermost Pliocene nannofossil Subzone CN12d (1.88–2.29 Ma). *Discoaster pentaradiatus*, *D. surculus*, and *D. asymmetricus* were found in Sample 133-815A-4H-CC, but *D. tamalis* is absent; thus, this sample was assigned to Subzone CN12b (2.42–2.6 Ma). Samples 133-815A-5H-CC through -7H-CC yielded *D. tamalis*, but no *Sphenolithus abies*, and can be assigned to Subzone CN12a (2.6–3.45 Ma). The highest occurrence of *Reticulofenestra pseudoumbilica* is in Sample 133-815A-8H-CC, while the highest occurrence of *Amaurolithus tricorniculatus* is in Sample 133-815A-34X-CC. The interval between these two biohorizons has been assigned to Zone CN11 and has an age range from 3.51 to 4.24 Ma. *Ceratolithus armatus* occurs in Samples 133-815A-36X-CC through -38X-CC; this interval has an age of 4.6 to 5.06 Ma (Zone CN10). The two preceding samples, Samples 133-815A-34X-CC and -35X-CC, must have an age range of 4.24 to 5.06 Ma, although not all of the markers were discovered in these samples.

The highest occurrence of *Discoaster quinqueramus* is in Sample 133-815A-39X-CC, and *Amaurolithus amplificus* was found in Sample 133-815A-42X-CC. This constrains Samples 133-815A-39X-CC through -41X-CC to an age range of 5.26 of 5.6 Ma (Subzone CN9b, latest Miocene). Sample 133-815A-42X-CC was dated as 5.6 to 5.9 Ma. *Amaurolithus delicatus* occurs in Samples 133-815A-43X-CC through -45X-CC; this interval has an age of 5.9 to 6.74 Ma. Samples 133-815A-46X-CC through -48X-CC contain only trace numbers of nannofossils, among them *D. quinqueramus*, but no amauroliths. The age of these samples is only broadly constrained to 5.9 to 8.2 Ma (Zone CN9, late Miocene). Core-catcher samples below this level yielded no datable nannofossils.

Planktonic Foraminifers

Most of the core-catchers of Hole 815A were investigated for planktonic foraminifers. The upper Pliocene section of the hole (Samples 133-815A-1H-CC through -11H-CC) yields abundant, well-preserved planktonic foraminifers. The upper Pliocene through upper Miocene Samples 133-815A-12H-CC through -47X-CC contain abundant to common specimens having moderate to good preservation, although specimens frequently have been pyritized. In Sample 133-815A-48X-CC, we could not identify the few, badly preserved specimens. In contrast, Sample 133-815A-50X-CC (near the bottom of the hole) contains a few identifiable specimens that are age-diagnostic for the early/middle Miocene transition.

The youngest, easily identifiable biohorizons are the last occurrences of *Globigerinoides fistulosus* (1.6 Ma) and *Globigerinoides obliquus* (1.8 Ma) in Sample 133-815A-3H-CC. The lower limit of the *Globorotalia truncatulinoides* range (Zone N22-N23) occurs in Sample 133-815A-4H-CC. Below this level (Sample 133-815A-6H-CC), we find the last occurrence of *Globoquadrina altispira* (2.9 Ma) and the first occurrence of *G. fistulosus* (2.9 Ma). In addition, the zonal boundary between Zones N21 and N18-N19 can be placed in Section 133-815A-7H-CC, corresponding to the first occurrence of *Globorotalia tosaensis* one core above. The top of the *Sphaeroidinellopsis seminulina* range (3.0 Ma) was found in Sample 133-815A-7H-CC.

The lower limit of Zone N18-N19 was placed in Core 133-815A-41X, based on the first occurrence of *Globorotalia tumida tumida* (5.2 Ma) in Sample 133-815A-40X-CC. Zone N16-N17 extends from Samples 133-815A-40X-CC through

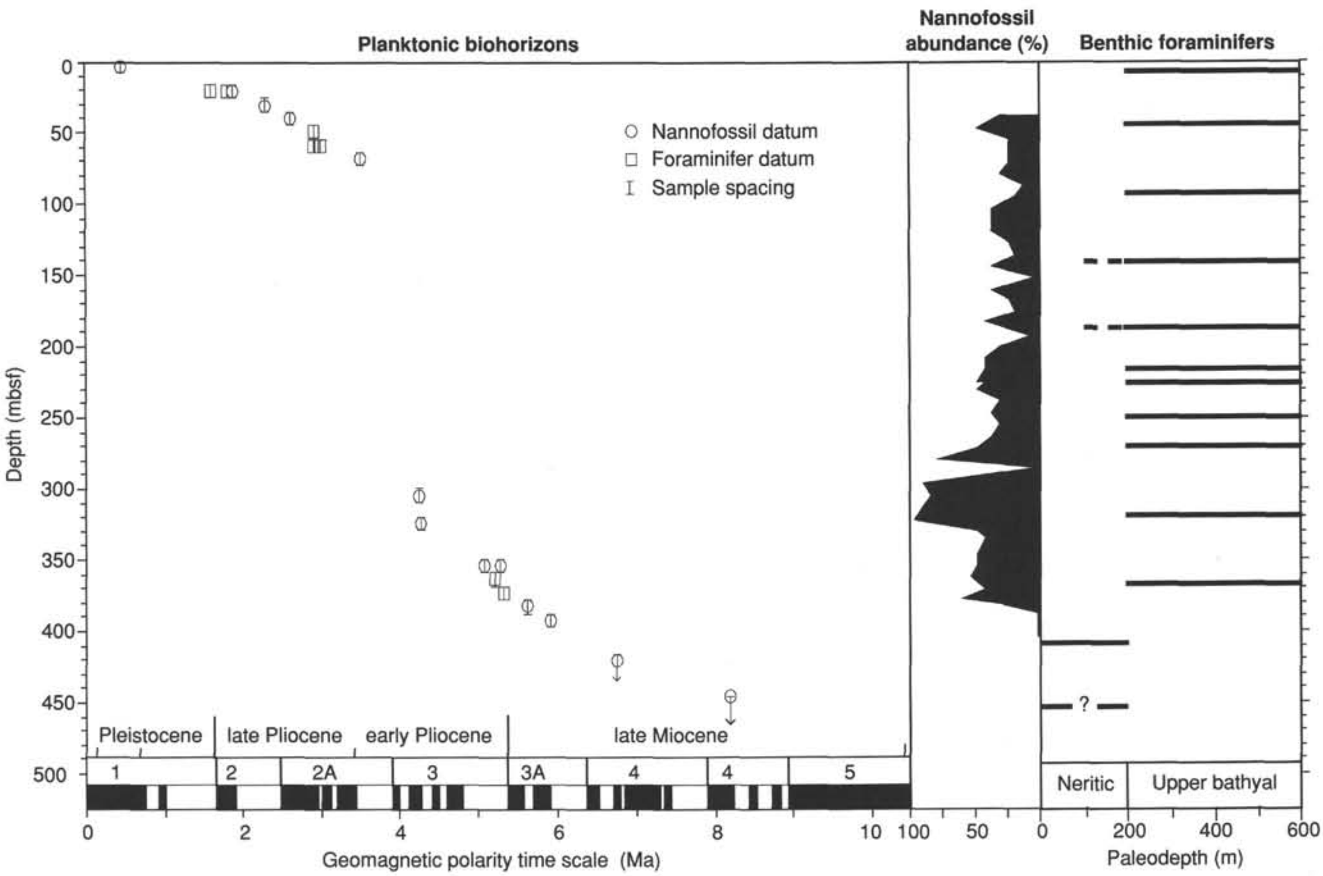

Figure 21. Age-depth plot based on calcareous nannofossils and planktonic foraminifers. Abundance of nannofossils within fine-fraction sediment (%) and paleodepth inferred by benthic foraminifers also are shown.

-47X-CC, although the lower limit is not well constrained because of the absence of planktonic foraminifers in Samples 133-815A-48X-CC and -49H-CC. Interestingly, Sample 133-815A-47X-CC contains abundant *Neogloboquadrina pachyderma*; this species is indicative of the penetration of colder surface waters into the area.

The oldest datable sample (Sample 133-815A-50X-CC) contains poorly preserved specimens of *Globorotalia conoidea*, *Globoquadrina altispira*, *Globoquadrina dehiscens*, *Globoquadrina woodi woodi*. The occurrence of *Globorotalia conoidea* suggests a minimum age of early middle Miocene (according to Jenkins, 1985), which constrains this sample to the transition of the early to middle Miocene.

Benthic Foraminifers

Approximately one of every four core-catcher samples from Hole 815A was examined for benthic foraminifers. Preservation is excellent, except for the bottom of the hole. Benthic foraminiferal assemblages show a deepening from the neritic zone (0–200 m) in the Miocene section to the upper bathyal zone (200–600 m) in the Pliocene.

Sample 133-815A-50X-CC contains poorly preserved benthic foraminifers that lack depth-diagnostic taxa. This sample contains abundant large specimens of the transported reefal benthic foraminifer *Amphistegina* sp. Sample 133-815A-45X-CC yielded a well-preserved benthic foraminiferal assemblage that lacks the exclusively bathyal benthic foraminifer species found in overlying samples, indicating an outer neritic fauna (100–200 m). This sample also contains the transported reefal taxon *Amphistegina* sp.

In and above Core 133-815A-40X, core-catcher samples yielded upper bathyal (200–600 m) benthic foraminiferal assemblages that included *Bulimina marginata*, *B. mexicana*, *C. bradyi*, *Cibicidoides cicatricosus*, *C. dutemplei*, *C. matanzasensis*, *C. mundulus*, *C. pachyderma*, *C. subhaidingerii*, *Hoeglundina elegans*, *Hyalinea balthica*, *Lenticulina peregrina*, *Plectofrondicularia vaughni*, *Rectuvigerina striata*, *Sphaeroidina bulloides*, *Sigmoilopsis schlumbergeri*, and *Uvigerina carapitana*, *U. hornibrooki*, and *U. proboscidea* (van Morkhoven et al., 1986). In addition to typical upper bathyal faunas, Samples 133-815A-15H-CC, -20H-CC, and -23H-CC contain abundant *Ammonia* spp. This taxon consistently is associated with shallow-water facies, such as coastal bays, lagoons, and estuaries (Poag, 1981). The absence of reefal contaminants in these same samples suggests that there may have been a nearby shallow-area source of *Ammonia* spp. that had no associated reef development.

Several samples contain rare specimens of species that were generally observed deeper than 600 m, which suggests that these samples may be from the lower upper bathyal zone. For example, Sample 133-815A-1H-CC contains several specimens of *Pyrgo murrhina*. Samples 133-815A-28X-CC and -40X-CC each contain a single specimen of *Cibicidoides robertsonianus*.

Larger Benthic Foraminifers

Larger benthic foraminifers occur in bioclastic packstones within the core-catcher sample of Core 133-815A-50X. This foraminiferal association consists of abundant *Nephrolepidina* (*N. howchini*?), smaller benthic foraminifers, and planktonic foraminifers. Two specimens of *Nephrolepidina* were mea-

Table 2. Summary of tentative magnetic reversal boundaries in Holes 815A and 815B.

Magnetic boundary	Age (Ma)	Depth (mbsf)	Core
Brunhes/Matuyama	0.73	15.3	/2H
Matuyama/Jaramillo	0.91	16.3	/2H
Jaramillo/Matuyama	0.98	17.5	/3H
Matuyama/Olduvai	1.66	21.7	/3H
Olduvai/Matuyama	1.88	25.2	/3H
Matuayama/Gauss	2.47	34.2	4H/4H
Gauss/Gilbert	3.40	62.5	7H/

sured: parameter dc for one specimen is 31%, for the other, 32%. Parameter F for both specimens is approximately 4. Values of both parameters suggest a latest early Miocene to early middle Miocene age for the analyzed specimens.

PALEOMAGNETISM

Cores from Holes 815A and 815B were measured using a pass-through cryogenic magnetometer. A preliminary reversal stratigraphy, based primarily on changes in inclination, was correlated to the geomagnetic polarity time scale back to the late Pliocene. The upper section of the reversal stratigraphy was compiled from Hole 815B (Cores 133-815B-1H to -4H) and the lower part of Hole 815A (Cores 133-815A-4H to -8H). The overlapping boundaries of the two holes are in close agreement, usually to within 1 m. Considerable scatter in inclination angles remained after AF 15 mT, and many of the reversal boundaries were not sharply defined. In addition, a secondary chemical remanence potentially exists as a result of the diagenetic regimes encountered at this site (see "Inorganic Geochemistry" section, this chapter). Analysis of discrete samples will be necessary to confirm these preliminary shipboard results.

NRM and AF 15-mT demagnetization measurements of the archive halves of Hole 815A and the top 36.4 m of Hole 815B provide a partially resolvable reversal stratigraphy to about 65 mbsf. A composite magnetostratigraphy (Table 2) summarizes the best-defined boundaries between the two holes. Deeper than 65 mbsf, the record becomes unclear, even after the AF 15-mT demagnetization step. With the aid of biostratigraphic tie-points, the following tentative magnetostratigraphic correlation was determined. The normal Brunhes Chron spanned from the top of the hole down to about 15.3 mbsf. The Matuyama reverse chron (0.73–2.47 Ma) ranged from 15.3 to 34.2 mbsf. The Matuyama Chron was punctuated by two normal zones from 16.3 to 17.5 mbsf and 21.7 to 25.2 mbsf. These zones correlated to the Jaramillo and Olduvai subchrons, respectively. The Matuyama/Gauss boundary was placed at 34.2 mbsf in Hole 815B and at 35.0 mbsf in Hole 815A. While having a relatively high sediment accumulation rate, at least one of the two short polarity reversal events within the Gauss normal may perhaps be recorded. A poorly defined normal-to-reverse polarity transition occurs at about 62.5 mbsf, this may perhaps be the Gauss/Gilbert boundary at 3.40 Ma. Much of the section below 70 mbsf retains a steep (>65°) normal polarity even after AF demagnetization at 15 mT.

The downhole NRM intensity profile shows values between 2 and 20 mA/m in the top 45-m, with an abrupt decrease from 0.1 to 1 mA/m by 50 mbsf. Intensities tend to increase downward, to between 0.5 and 5 mA/m by 150 mbsf. This increasing intensity, and several distinct intensity peaks between 125 and 250 mbsf, indicates that either a differential depositional influx and preservation of magnetic minerals occurred, or that a secondary, chemical remanence was recorded. In fact, most of the intensity peaks correspond to zones of steep inclination overprints. Second, traces of fine-grained iron sulfides commonly occur below 50 mbsf. One of these samples (Section 133-815A-39X-4 at 68 cm) analyzed onboard the ship using XRD indicated the presence of pyrite and perhaps greigite. The intermediate iron sulfides usually have a ferrimagnetic moment and occur as transition minerals during sulfurization reactions, which culminate with the formation of pyrite. The occurrence of these secondary minerals suggests that strong reducing conditions may have partially destroyed the depositional iron-oxides.

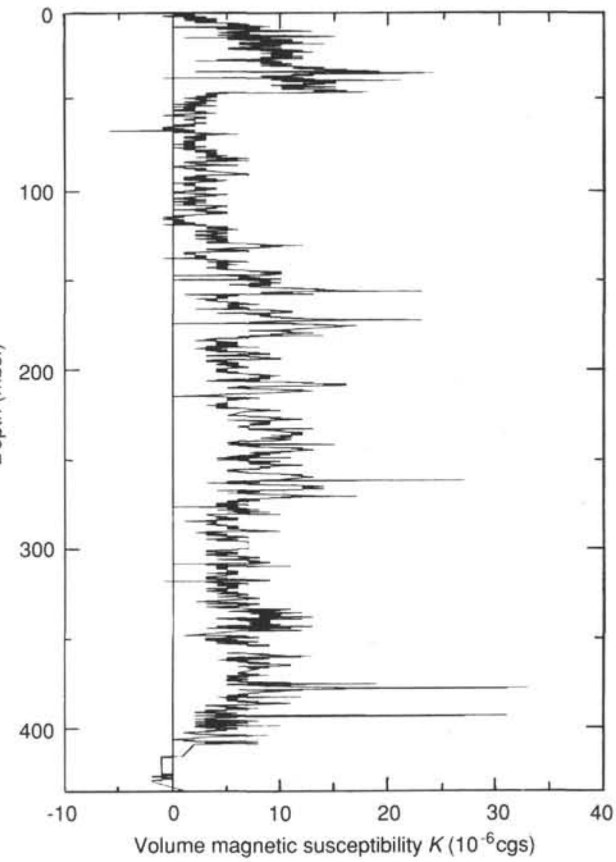

Figure 22. Magnetic susceptibility data from Hole 815A.

Whole-round volume-susceptibility data from Hole 815A exhibit distinct variations with depth (Fig. 22). The top 45 mbsf shows a relatively strong susceptibility that coincides with the strong magnetic intensities measured with the cryogenic magnetometer. From 45 to 125 mbsf, susceptibility is slightly lower, although still positive. A zone of higher volume susceptibility from 125 to about 410 mbsf may correspond to sediments that contain either greigite or pyrite, which have a relatively high specific susceptibility, or to a lesser degree zones of authigenic pyrite and clay minerals, which have considerably lower specific susceptibilities.

A total of 119 discrete oriented samples were collected in the top eight cores (73.3 mbsf) to confirm shipboard magnetic polarity zones. Because of shipboard time constraints, all these samples will be analyzed as part of a shore-based study.

SEDIMENTATION RATES

The sedimentation rate at Site 815 has varied by more than an order of magnitude over the last 6 m.y., the interval for which biostratigraphic control is very good (see Fig. 21). Sediments consist almost entirely of hemipelagic and pelagic

Table 3. Concentrations of minor and trace elements measured in interstitial fluids, Site 815.

Core, section, interval (cm)	Depth (mbsf)	pH	Alk. (mM)	Sal. (g/kg)	Cl^- (mM)	Mg^{2+} (mM)	Ca^{2+} (mM)	SO_4^{2-} (mM)	P (μM)	NH_4 (μM)	Si (μM)	K^+ (mM)	Na^+ (mM)	Rb^{2+} (μM)	Sr^{2+} (μM)
Surface seawater	0	8.24	2.646	35.0	573.01	53.55	10.27	28.12	0	0	0	9.80	466	1.4	86
133-815AH-3, 145–150	4.45	7.67	3.166	35.5	538.71	51.69	10.35	28.01	0	66	90	10.04	436	1.6	193
2H-5, 145–150	14.25	7.28	3.082	35.5	536.70	48.59	10.28	24.16	0	276	105	10.84	435	1.4	335
3H-5, 145–150	23.80	7.35	3.191	35.2	558.89	46.11	10.12	23.01	0	455	107	10.21	462	1.4	431
4H-5, 145–150	33.25	7.32	3.414	35.8	573.01	44.56	10.15	20.09	1	756	107	9.82	477	1.4	526
5H-5, 145–150	42.75	7.32	3.517	35.8	583.10	40.90	10.14	18.36	1	806	113	9.52	493	1.3	610
6H-5, 145–150	52.25	7.25	3.923	35.8	592.18	38.17	10.45	16.21	1	1123	134	8.99	505	1.2	798
7H-5, 145–150	61.75	7.21	4.046	36.0	596.22	35.37	10.85	14.75	1	1289	141	8.75	513	1.1	817
8H-5, 145–150	71.25	7.25	4.162	35.8	607.31	34.13	10.81	12.97	1	1482	138	8.05	526	1.0	897
9H-5, 145–150	80.75	7.32	4.408	36.0	613.37	32.37	10.75	11.26	1	1650	162	7.71	534	1.0	973
10H-5, 140–150	90.20	7.33	4.486	36.0	614.37	30.30	10.58	9.73	1	1774	170	7.04	539	0.9	1063
13H-5, 140–150	118.70	7.25	4.686	36.0	603.28	27.23	10.45	5.76	2	1529	166	6.87	530	0.8	1239
16H-5, 140–150	147.20	7.46	4.511	36.5	637.58	25.31	10.59	2.76	2	1667	189	5.69	566	0.7	1347
19H-5, 140–150	175.70	7.43	4.318	37.8	662.80	25.44	11.16	1.63	2	2072	202	5.54	589	0.6	1445
22H-5, 140–150	204.20	7.35	3.958	39.0	698.11	27.50	12.51	1.52	4	3405	185	5.59	616	0.5	1534
26X-3, 140–150	226.90	7.46	4.144	40.0	705.17	28.68	14.19	2.33	2	3262	227	4.33	620	0.5	1541
28X-3, 140–150	246.20	7.56	4.005	40.0	699.12	30.54	15.24	4.11	2	3262	210	4.62	610	0.5	1412
31X-4, 140–150	276.70	7.38	3.218	42.0	714.25	31.96	20.19	5.69	2	3411	204	4.67	613	0.5	1400
34X-5, 140–150	307.30	7.46	2.575	42.2	742.50	35.49	20.72	7.81	1	3096	214	5.26	634	0.5	1414
37X-5, 140–150	336.40	7.48	2.451	43.2	743.50	37.80	22.14	9.97	0	2900	208	5.85	629	0.6	1261
40X-5, 140–150	365.50	7.17	3.226	44.2	759.65	37.81	24.27	11.38	0	2870	184	5.25	643	0.9	1342
43X-5, 140–150	394.50	7.23	3.105	46.5	769.73	40.06	26.06	13.89	0	2448	265	5.72	648	0.8	1124
47X-5, 140–150	432.70	7.26	3.107	45.5	759.65	42.61	26.82	15.99	0	2299	175	6.43	633	1.1	920

Alk. = alkalinity; Sal. = Salinity

ooze, and planktonic microfossils constitute a large proportion (perhaps from 10% to 75%) of these sediments. Within a biochronological framework, based on core-catcher samples only, the section can be divided into four distinct units on the basis of sedimentation rate. The topmost unit extends from 0 to 44.8 mbsf and spans the time interval from 0 to 2.6 Ma. This interval has a sedimentation rate of about 1.7 cm/k.y., i.e, normal pelagic sedimentation. The next lower unit extends from 44.8 to 73.3 mbsf and spans the time interval from 2.6 to 3.51 Ma. The sediment accumulation rate is 3.2 cm/k.y., about double that of the interval above, but still within range of normal pelagic accumulation rate.

Next, from 73.3 to 309.6 mbsf (3.51–4.24 Ma), the sedimentation rate increases at least 10-fold, to 38.5 cm/k.y. for the upper part (73.3–215.8 mbsf) and to 26 cm/k.y. for the lower part (215.8–309.6 mbsf). To the extent that core-catcher samples are representative, the proportion of pelagic carbonate in the sediment, specifically coccoliths, does not seem to change significantly when averaged for each of the three "units." Apparently, dilution of normal pelagic influx by allochthonous detritus did not cause the increased sediment accumulation.

The lowermost interval, from 309.6 to 396.4 mbsf, perhaps slightly deeper, spans the time period from 4.24 to 5.9 Ma, for an average sedimentation rate of 5.2 cm/k.y. (When calculated in the four shorter increments into which this interval can be divided, the sedimentation rate varies from a minimum of about 3 cm/k.y. to a maximum of about 8.5 cm/k.y.; however, these calculations may contain large errors because of the large sample spacing and short time spans involved.) The proportion of pelagic carbonate may be significantly greater in this lowermost unit, which averages perhaps nearly 40% down to about 400 mbsf.

Given that the high sedimentation rate over much of the section cannot be accounted for by additional detrital influx and recognizing that enhanced productivity, although it probably occurred, cannot reasonably account for a 10-fold increase in pelagic carbonate production, the most attractive explanation is that much of this fine-grained sediment was transported to this site laterally by ocean currents. Therefore, the sediment is best described as a drift deposit or contourite. Interestingly, no sign of redeposition exists among the calcareous nannofossils. Indeed, the chronologic integrity of the sequence seems to have been meticulously preserved.

INORGANIC GEOCHEMISTRY

Interstitial Waters

Interstitial fluids were taken from the first 10 cores of Hole 815A and from Cores 133-815A-13H, -16H, -19H, -22H, -26X, -28X, -31X, -34X, -37X, -40X, -43X, and -47X. Samples were analyzed according to procedures outlined in the "Explanatory Notes" chapter (this volume). As a result of the unusual geochemical signatures observed at this site, K^+, Rb^{2+}, and NH_4+ also were measured. The concentration of Na^+ was determined by difference.

Calcium, Magnesium, Strontium, Rubidium, and Potassium

The concentration of Ca^{2+} remains approximately constant with increasing sub-bottom depth between the sediment/seawater interface and 147.2 mbsf. From this depth to the base of the cored section, a gradient of 0.057 mM/m reaches a maximum concentration of 26.82 mM at 432.7 mbsf (Table 3 and Fig. 23). In contrast, the concentration of Mg^{2+} decreases from values of 53.55 mM at 4.45 mbsf to a minimum of 25.31 mM at 147.20 mbsf. From 147.20 to 432.70 mbsf, the Mg^{2+} increases at a rate of 0.06 mM/m, approximately the same rate as the increase in Ca^{2+}. Concentrations of K^+ and Rb^{2+} mirror the changes observed in Mg^{2+}, although the minima for both elements occur at a slightly deeper depth (226.9 mbsf; Fig. 23). Concentrations of Sr^{2+} increase rapidly from 86 μM at 4.45 mbsf to a maximum of 1541 μM at 226.9 mbsf. From this depth, Sr^{2+} decreases to 920 μM at a depth of 432.7 mbsf.

Sulfate, Alkalinity, Phosphate, and Ammonia

The concentration of sulfate decreases dramatically with increasing sub-bottom depths and reaches a minimum of 1.52 mM at 204.2 mbsf (Table 3 and Fig. 24A). Below this depth, concentrations increase at a rate of 0.06 mM/m, which is identical to the change in Mg^{2+} over the same interval. This decrease in sulfate is accompanied by an increase in the concentration of NH_4^+ to 3.4 μM at 204.2 mbsf. Only a very

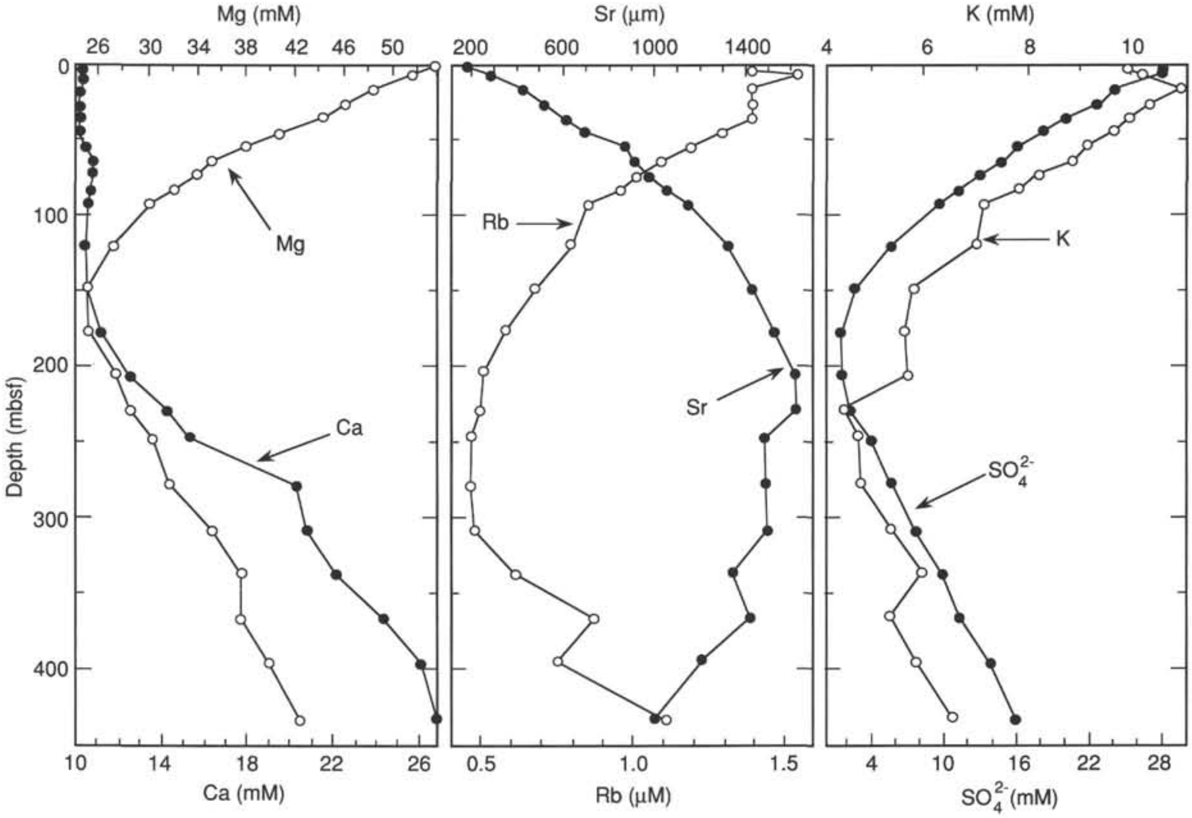

Figure 23. Concentrations of Ca^{2+}, Mg^{2+}, Sr^{2+}, Rb^{2+}, K^{+}, and SO_4^{2-} as a function of depth at Site 815. Note the sharp decrease in the concentration of Mg^{2+}, SO_4^{2-}, K^{+}, and Rb^{2+} with increasing sub-bottom depth.

small increase occurs in concentrations of phosphate (2 μM). Alkalinity reaches a maximum value of 4.69 mM at 118.7 mbsf, then decreases to 2.45 mM at 336.4 mbsf.

Salinity, Chlorinity, and Sodium

Throughout the cored interval, concentrations of chloride and sodium increase, from 573 and 466 mM, respectively, at 4.45 mbsf, to 769.73 and 633 mM at 394.5 mbsf. Although a small decrease occurs in the deepest sample analyzed at 432.7 mbsf, this increase may have resulted from a small degree of contamination and therefore should not be considered indicative of further trends at this site (Table 3 and Fig. 24B).

Interpretation

The overall geochemistry of Site 815 is dominated by the increasing salinity of pore fluids with increasing depth. This trend produces similar concentration-vs.-depth gradients for Mg^{2+}, Ca^{2+}, and SO_4^{2-} over the lower portion of Hole 815A. However, trends in the concentrations of trace and minor elements cannot be related to simple salinity changes. To investigate these variations, the effect of salinity can be removed by normalizing the concentration of a minor or trace element to chloride and then comparing its ratio to that of seawater.

$$[M/Cl_{sample} - M/Cl_{seawater}] \cdot Cl_{seawater} \qquad (1)$$

In this equation, the variable M represents the concentration of a minor or trace element under consideration. Results of this calculation are shown in Table 4 and Figure 24B for Ca^{2+}, Mg^{2+}, and K^{+}. As can be seen in this figure, in spite of the large increase in Cl^{-}, no change occurs in the amount of excess Ca^{2+} between 4.45 and 204.2 mbsf. Hence, Ca^{2+} is being removed from pore waters at a rate equal to the increase resulting from the change in salinity. Over the same interval, Mg^{2+} and K^{+} have been removed, but at greater rates than those for Ca^{2+}. Below 204.2 mbsf, Ca^{2+} is being added to the system in excess of that expected from any change in the chlorinity. This increase may result from the dissolution of a Ca-bearing mineral phase or alternatively, the presence of $CaSO_4$ brines at a greater depth. The loss of Ca^{2+} resulting from the precipitation of calcium carbonate in the upper portion of Site 815 is supported by the large increase in the concentration of Sr^{2+}. The removal of sulfate from the pore fluids controls the solubility product of celestite, which normally limits upper Sr^{2+} concentrations (Fig 24C). Consequently, a maximum Sr^{2+} concentration of 1541 μM is significantly higher than that usually measured in marine sediments.

A decrease in the concentrations of Mg^{2+}, K^{+}, and Rb^{2+} over the upper portion of Hole 815A is the result of clay mineral diagenesis. These elements typically are consumed during this process, while Ca^{2+} is released.

The decrease in the concentration of SO_4^{2-} over the upper interval results from oxidation of organic material during the sulfate reduction of bacteria. The low concentration of organic material throughout the interval (see "Organic Geochemistry" section, this chapter) and the fact that sulfate has not been completely removed indicate that oxidation of organic material is almost complete. Confirmation of the original presence of organic material is provided by the concentration of ammonia, which reaches 3.4 mM in Core 133-815A-22H. However, phosphate is present at only very low concentrations, indicating its possible removal, either through precipitation or adsorption onto clay minerals. Of further interest is the apparent absence of H_2S, which probably is consumed during formation of pyrite. However, the presence of elemen-

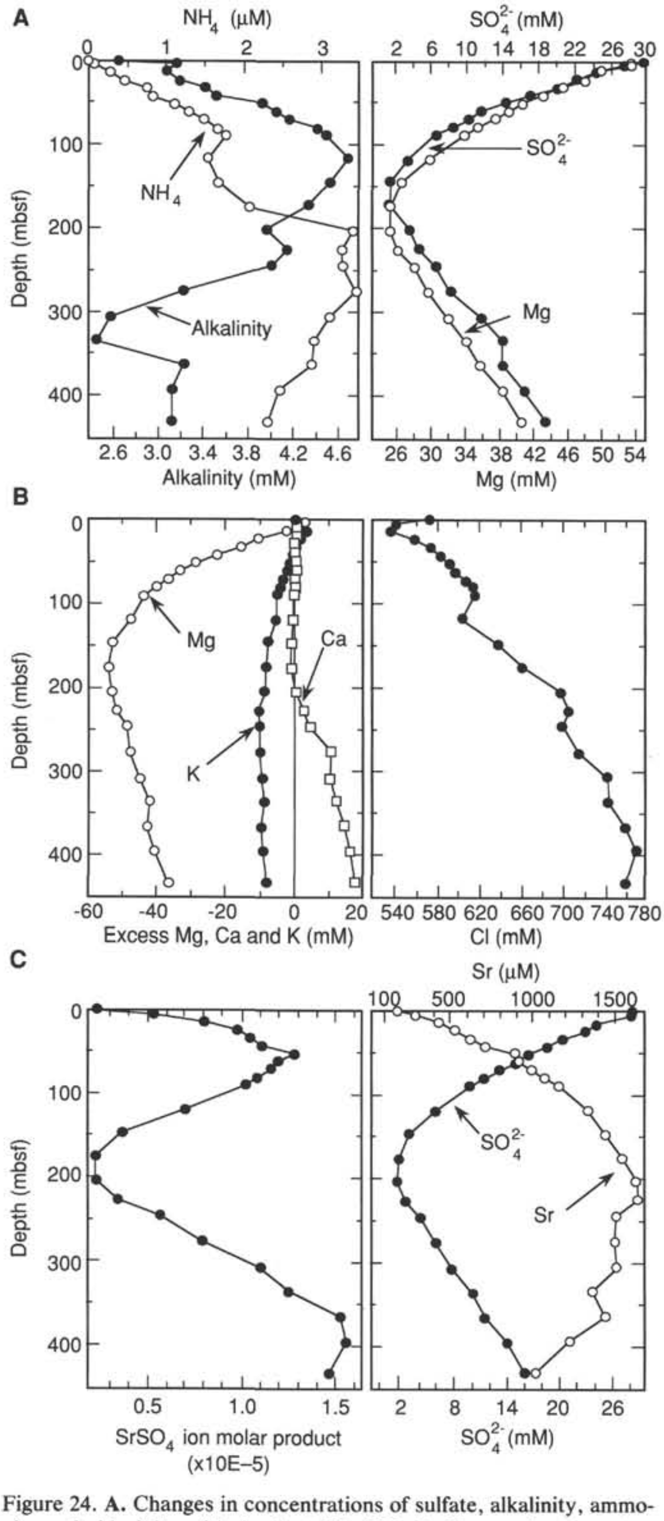

Figure 24. **A.** Changes in concentrations of sulfate, alkalinity, ammonia, and chlorinity with depth at Site 815. **B.** Changes in concentrations of Ca^{2+}, Mg^{2+}, and K^+ relative to seawater Cl^- concentrations at Site 815 calculated using Equation 1. **C.** Changes in concentrations of sulfate, strontium, and the ion molar product of celestite ($SrSO_4$) with increasing depth at Site 815.

Table 4. Changes in excess Ca^{2+}, Mg^{2+} K^+, and Mg/Ca ratio with depth for Site 815.

Depth (mbsf)	Mg (mM)	Ca (mM)	K (mM)	Mg/Ca
00.00	0.00	0.00	5.22	
4.45	1.53	1.30	2.49	4.99
14.25	3.10	1.24	−2.92	4.73
23.80	1.17	0.20	−10.96	4.55
33.25	0.03	−0.21	−15.70	4.39
42.75	−0.78	−0.53	−23.31	4.03
52.25	−1.92	−0.26	−29.00	3.65
61.75	−2.43	0.28	−34.13	3.26
71.25	−3.85	−0.12	−37.25	3.16
80.75	−4.53	−0.39	−40.69	3.01
90.20	−5.64	−0.69	−44.14	2.86
118.70	−5.71	−0.60	−48.32	2.61
147.20	−8.18	−1.31	−53.76	2.39
175.70	−8.74	−1.08	−55.08	2.28
204.20	−9.10	0.01	−54.07	2.20
226.90	−10.96	2.20	−52.79	2.02
246.20	10.49	3.88	−49.77	2.00
276.70	−10.56	10.36	−48.70	1.58
307.30	−10.02	9.98	−45.66	1.71
336.40	−9.23	11.87	−42.62	1.71
365.50	−10.19	14.03	−43.68	1.56
394.50	−9.67	15.94	−41.41	1.54
432.70	−8.64	17.39	37.36	1.59

tal sulfur was noted only by using the CHNS analyzer below Core 133-815A-33X, and although pyrite must be present in the upper portion of the section, it is probably being localized in discrete nodules.

The origin of the increase in salinity in pore waters from the lowerportion of the core is not known at present, but one might speculate that it results from the presence of an evaporite unit at some depth below the cored interval. Such a deposit has not as yet been identified in the Townsville Trough, but is known from sediments of Oligoceneage in the Capricorn Basin approximately 300 to 400 km to the south (Ericson, 1976).

Carbonate and X-Ray Diffraction

The percentage of calcium carbonate and relative mineralogy of selected interstitial-water sediments and physical property samples is shown in Figure 25 and Tables 5 and 6. To compare the percentage of calcium carbonate as a function of age, the depth of the samples has been assigned an age based on sedimentation rate (see "Sedimentation Rates" section, this chapter). Data have been interpolated to a constant sampling interval of 100,000 yr. These data then were treated with a five-point weighted filter. Results of these calculations are shown in Figure 26.

Percentages of calcium carbonate exhibit a large range of variation: from more than 90% to as low as 34.3% at 171.8 mbsf. A general trend of decreasing calcium carbonate with increasing depth (200 and 250 mbsf) reaches a minimum in Unit II (See "Lithostratigraphy" section, this chapter). These percentages then increase with depth from this interval and reach a mean value of 75% in Unit V (415.7–444.5 mbsf). The highest concentrations of carbonate are found in the dolomitized interval at the base of Hole 815C. The smoothed interpolated carbonate curve (Fig. 26) exhibits some systematic variations with age that might indicate changes in sea level. The most important decrease in percentage of carbonate may be associated with the large decline in sea level that occurred between 4.2 and 3.8 Ma and is marked by a rate of sedimentation in excess of 300 m/m.y.

The thick Pliocene section at Site 815 appears to be dominated by clays, yet based on carbonate data, only rarely does the insoluble fraction make up more than 50% of these

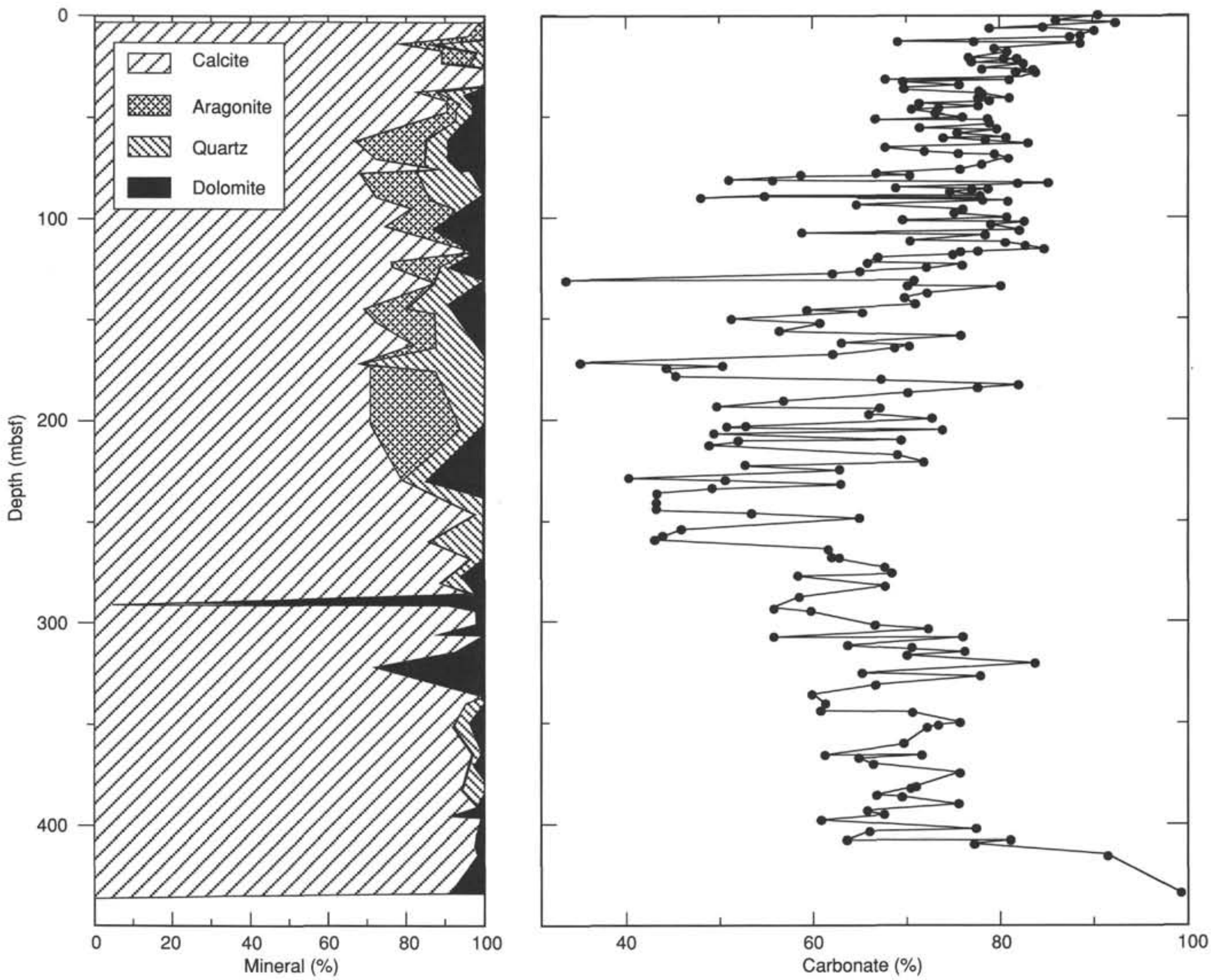

Figure 25. Changes in percentages of carbonate and mineralogy as a function of depth at Site 815.

sediments. A small fraction of the nonacidic, soluble portion of the sediment (10%–20%) was quartz. Dolomite was present in concentrations of less than 5% throughout the site, although the core-catcher sample from Core 133-815A-33X contained an interval of 100% dolomite. Although aragonite disappeared rapidly from the Pleistocene section of Site 815, this mineral reappears in the upper Pliocene sediments that make up between 10% and 20% of the acid-soluble fraction as deep as 204 mbsf in lower Pliocene sediments. The disappearance of aragonite marks the boundary between lithologic Units II and III.

ORGANIC GEOCHEMISTRY

In addition to safety monitoring for hydrocarbons, the main purpose of shipboard organic geochemistry studies at Site 815 was to assess the amount and type of organic matter preserved in the Pleistocene to lower middle Miocene sediments of the southern margin of the Townsville Trough.

We determined the total nitrogen, sulfur, and carbon, and the total organic carbon contents of 50 samples collected for chromatographic analyses of volatile hydrocarbons (headspace samples) using an NA 1500 Carlo Erba NCS analyzer. Detailed descriptions of methods are outlined in the "Explanatory Notes" chapter (this volume).

Volatile Hydrocarbons

Light hydrocarbon gases (C_1–C_3) in sediments were analyzed routinely as part of the ODP safety and pollution-prevention monitoring program, using the headspace technique and the Carle gas chromatograph. The results are presented in Table 7.

The sediments at Site 815 contained low concentrations of hydrocarbon gases and presented no safety problems. Concentrations of methane in headspace gas were from 2 to 9 ppm. In two intervals (183–231 mbsf and 328–408 mbsf), where methane concentrations were greater than 5 ppm, rare trace amounts of ethane and propane were detected.

Organic Carbon Contents

Total organic carbon (TOC) contents and total nitrogen and sulfur concentrations recorded in Hole 815A are presented in Table 8. We observed low but variable TOC values in these sediments, and total nitrogen and sulfur concentrations were below detection limits of the NCS analyzer, except in Unit IV (Fig. 27).

In Unit I (Pleistocene to upper lower Pliocene foraminifer nannofossil ooze), TOC values were very low and ranged

Table 5. Concentrations of minerals determined using X-ray diffraction, Site 815.

Core, section, interval (cm)	Depth (mbsf)	Calcite (%)	Aragonite (%)	Quartz (%)	Dolomite (%)
133-815A-					
1H-2, 101–102	2.51	95.6	0.0	4.4	0.0
1H-3, 90–92	3.90	83.7	7.2	6.6	2.4
1H-3, 145–150	4.45	100.0	0.0	0.0	0.0
2H-2, 101–103	9.31	96.6	0.0	3.4	0.0
2H-5, 80–82	13.60	79.1	18.5	2.4	0.0
2H-5, 145–150	14.25	77.7	9.0	11.7	1.6
3H-2, 100–102	18.80	90.5	7.6	0.0	1.9
3H-5, 145–150	23.75	89.4	7.7	1.9	0.9
4H-2, 100–102	28.30	99.9	0.0	0.0	0.1
4H-5, 145–150	33.25	100.0	0.0	0.0	0.0
5H-2, 101–103	37.81	81.6	6.8	7.1	4.5
5H-5, 145–150	42.75	91.0	4.7	2.6	1.6
6H-2, 102–103	47.32	91.3	2.0	5.2	1.5
6H-5, 145–150	52.25	82.3	11.9	3.6	2.3
7H-5, 145–150	61.75	66.2	20.0	5.2	8.6
8H-5, 145–150	71.25	72.4	13.4	5.9	8.4
9H-2, 102–103	75.82	88.8	0.0	6.0	5.2
9H-2, 145–150	76.25	67.9	15.7	14.4	2.0
10H-5, 145–150	90.25	72.7	13.3	13.8	0.2
11H-3, 90–92	96.20	81.2	12.5	2.4	3.9
12H-3, 80–82	105.6	73.3	14.3	0.0	12.4
13H-4, 90–92	116.7	96.9	0.0	0.0	3.1
13H-5, 145–150	118.7	79.0	14.8	3.5	2.7
14H-3, 80–82	124.6	75.9	13.3	2.8	8.0
15H-2, 80–82	132.6	88.0	0.0	12.0	0.0
16H-3, 130–132	144.1	68.0	13.1	10.2	8.6
16H-5, 145–150	147.2	68.9	18.8	4.5	7.8
18H-3, 94–96	162.7	81.7	7.0	10.2	1.2
19H-3, 50–52	171.8	66.0	0.0	34.0	0.0
19H-5, 145–150	175.7	70.9	16.7	12.4	0.0
22H-5, 145–150	204.2	70.8	23.3	5.7	0.2
26X-3, 145–150	230.2	78.9	0.0	7.2	13.9
27X-5, 101–103	239.2	87.1	0.0	12.9	0.0
28X-3, 145–150	246.2	97.5	0.0	1.7	0.8
29X-5, 101–103	258.5	83.5	0.0	16.5	0.0
30X-5, 101–103	268.2	96.1	0.0	3.9	0.0
31X-4, 145–150	276.7	90.4	0.0	3.9	5.7
32X-1, 60–62	281.1	87.6	0.0	8.5	3.9
32X-4, 60–62	285.6	95.9	0.0	2.8	1.3
33X-1, 13–15	290.3	2.4	0.0	0.0	97.6
33X-1, 80–82	291.0	90.9	0.0	4.6	4.5
33X-4, 80–82	295.5	97.3	0.0	1.9	0.8
34X-1, 90–92	300.8	97.7	0.0	0.0	2.3
34X-5, 90–92	306.8	82.5	0.0	13.4	4.1
34X-5, 145–150	307.3	98.9	0.0	0.0	1.1
35X-1, 78–80	310.3	95.0	0.0	0.0	5.0
35X-4, 78–80	314.8	91.1	0.0	4.2	4.7
36X-2, 101–103	321.8	69.9	0.0	0.0	30.1
37X-5, 140–150	336.4	100.0	0.0	0.0	0.0
38X-2, 51–53	340.7	94.5	0.0	5.5	0.0
39X-2, 62–64	350.5	91.4	0.0	4.8	3.9
40X-5, 140–150	365.5	96.5	0.0	2.6	0.9
41X-2, 72–74	370.0	95.2	0.0	2.3	2.5
42X-4, 69–72	382.5	93.6	0.0	6.4	0.0
43X-3, 74–76	390.8	97.7	0.0	0.0	2.3
43X-5, 140–150	394.5	86.4	0.0	7.5	6.0
44X-1, 115–117	397.5	98.7	0.0	0.0	1.3
45X-2, 59–61	408.0	97.1	0.0	2.9	0.0
46X-1, 68–70	416.3	96.9	0.0	0.0	3.1
47X-5, 140–150	432.7	90.4	0.0	2.3	7.4

between 0% (Subunit IA) and 0.20% (Subunits IB and IC).

In Unit II (lower Pliocene foraminifer nannofossil ooze), TOC values ranged between 0% and 0.1% (in light greenish-gray, carbonate-rich sediments), 0.3% to 0.5% (in dark greenish-gray sediments of Subunit IIB), and 1% (in dark gray, clay-rich sediments of Subunit IIA). Repetitive color changes, controlled by short-term fluctuations in both grain size and clay/carbonate contents, suggest cyclic sedimentation (see "Lithostratigraphy" section, this chapter), together with cyclic preservation of the organic content in the darker and more clay-rich sediments. Rock-Eval pyrolysis results of the most organic-rich sediment (Sample 133-815A-10H-5, 149–150 cm), presented in Table 9, characterize a very immature (T_{max} = 392°C), hydrogen-depleted (HI = 91 mg HC/g TOC) and well-oxygenated (OI = 288 mg CO_2/g TOC) kerogen of primarily terrestrial origin (?).

In Unit III (lower Pliocene foraminifer nannofossil chalk), TOC values were very low and ranged between 0.10% and 0.25%.

In Unit IV (upper upper Miocene to lower lower Pliocene, largely burrowed foraminifer nannofossil chalk, with nodules of pyrite), TOC values and total nitrogen and sulfur concentrations abruptly increased below 350 mbsf. TOC values were low and ranged between 0.45% and 0.60%, total nitrogen concentrations did not exceed 0.05%, and total sulfur concentrations reached as high as 0.46% (Sample 133-815A-43X-5, 149–150 cm). On the basis of the TOC/nitrogen ratios (Fig. 27), the origin of the organic matter seems to be predominantly terrestrial. Rock-Eval pyrolysis results of nine bulk sediments (Samples 133-815A-26X-3, 149–150 cm, to -48X-1, 68–69 cm), presented in Table 9, characterize a very immature (T_{max} 405°C), moderately hydrogenated (most of the HI values ranged between 150 and 350 mg HC/g TOC) and largely oxygenated kerogen (most of the OI values were very high: greater than 400 mg CO_2/g TOC).

More detailed shore-based studies (elemental analysis and optical investigations for extracted kerogens) will permit characterization of the short-term fluctuations in the vertical distribution and preservation of different components of the organic matter in the sediments encountered at Site 815.

PHYSICAL PROPERTIES

Physical properties analyzed in cores from this site included bulk density, *P*-wave velocity, and magnetic susceptibility on unsplit cores and *P*-wave velocity, electrical resistivity formation factor, shear strength, and index properties (including bulk density, grain density, water content, porosity, and void ratio) on split cores. The methods used are described in detail in the "Explanatory Notes" chapter (this volume).

Bulk Density

Bulk densities for Site 815 were determined from volume and mass measurements of discrete core samples and from gamma-ray absorption by whole-round cores (Figs. 28A, 29, and 30A; Table 10). One must use caution with the GRAPE density data because cores obtained using the XCB tend to be smaller in diameter than cores obtained with the APC. We suggest that the user consult core photos to obtain evidence of varying diameter and beware of the formation of drilling biscuits in XCB cores, which will appear as rhythmic variation in density.

P-Wave Velocity

P-wave velocities were measured for whole-round cores using the multisensor track (MST) and for discrete core samples using the Hamilton frame (Table 11 and Figs. 28B, 29, 30D, and 31). Note that we often failed to obtain *P*-wave velocity data from cores that were obtained during XCB drilling because these cores were smaller in diameter than APC cores and thus did not fill the plastic core-barrel liner. As a result, poor acoustic coupling occurred between the core and the core liner. This accounts for the loss of *P*-wave data between 220 and 360 mbsf in Hole 815A (Fig. 28). Note also that density apparently decreases at the same depth. Again, this occurred because core diameter was narrower and absorbed fewer gamma rays.

Table 6. Percentages of carbonate, Site 815.

Core, section interval (cm)	Depth (mbsf)	Carbon (%)	Carbonate (%)
133-815A-			
1H-1, 101–103	1.01	10.92	91.00
1H-2, 101–102	2.51	10.77	89.70
1H-3, 101–102	4.01	10.32	86.00
1H-3, 149–150	4.49	10.84	90.30
1H-4, 101–102	5.51	11.09	92.40
1H-5, 41–43	6.41	10.14	84.50
2H-1, 101–103	7.81	9.46	78.80
2H-2, 101–103	9.31	10.84	90.30
2H-3, 101–103	10.81	10.64	88.60
2H-4, 101–103	12.31	10.47	87.20
2H-5, 82–84	13.62	8.27	68.90
2H-5, 149–150	14.29	9.25	77.10
2H-6, 101–103	15.31	10.67	88.90
3H-1, 100–102	17.30	9.54	79.50
3H-2, 100–102	18.80	9.69	80.70
3H-3, 100–102	20.30	9.55	79.60
3H-4, 100–102	21.80	9.18	76.50
3H-5, 82–84	23.12	9.25	77.10
3H-5, 149–150	23.79	9.92	81.70
3H-6, 100–102	24.80	9.75	81.20
3H-7, 58–60	25.88	9.85	82.10
4H-1, 118–120	26.98	9.41	78.40
4H-2, 100–102	28.30	10.03	83.50
4H-3, 100–102	29.80	10.07	83.90
4H-4, 100–102	31.30	9.82	81.80
4H-5, 100–102	32.80	8.14	67.80
4H-5, 149–150	33.29	9.81	81.10
4H-6, 100–102	34.30	8.35	69.60
5H-1, 101–103	36.31	9.08	75.60
5H-2, 101–103	37.81	8.39	69.90
5H-3, 101–103	39.31	9.35	77.90
5H-4, 101–103	40.81	9.41	78.40
5H-5, 101–103	42.31	9.74	81.10
5H-5, 149–150	42.79	9.53	78.50
5H-6, 101–103	43.81	8.57	71.40
6H-1, 102–104	45.82	9.30	77.50
6H-2, 102–104	47.32	8.47	70.60
6H-3, 102–104	48.82	8.85	73.70
6H-4, 102–104	50.32	8.77	73.10
6H-5, 82–84	51.62	9.13	76.10
6H-5, 149–150	52.29	8.10	66.70
6H-6, 102–104	53.32	9.44	78.60
7H-1, 101–104	55.31	9.41	78.40
7H-2, 101–104	56.81	8.58	71.50
7H-3, 101–104	58.31	9.56	79.60
7H-4, 101–104	59.81	9.07	75.60
7H-5, 101–104	61.31	9.69	80.70
7H-5, 149–150	61.79	9.05	73.90
7H-6, 101–104	62.81	9.42	78.50
8H-1, 101–102	64.81	9.95	82.90
8H-2, 100–102	66.30	8.13	67.70
8H-3, 100–102	67.80	8.61	71.70
8H-4, 100–102	69.30	9.05	75.40
8H-5, 100–102	70.80	9.63	80.20
8H-5, 149–150	71.29	9.59	79.10
8H-6, 100–102	72.30	9.70	80.80
9H-1, 102–104	74.32	9.40	78.30
9H-2, 102–104	75.82	9.39	78.20
9H-3, 102–104	77.32	9.09	75.70
9H-4, 102–104	78.82	8.00	66.60
9H-5, 82–84	80.12	8.45	70.40
9H-5, 149–150	80.79	7.28	58.70
9H-6, 103–105	81.83	6.16	51.30
10H-1, 17–19	82.97	6.67	55.60
10H-1, 137–139	84.17	9.84	82.00
10H-2, 7–9	84.37	10.21	85.00
10H-2, 70–72	85.00	9.34	77.80
10H-2, 147–149	85.77	8.26	68.80
10H-3, 44–46	86.24	9.43	78.60
10H-4, 15–17	87.45	9.31	77.60
10H-4, 74–76	88.04	8.91	74.20
10H-5, 40–42	89.20	9.27	77.20
10H-5, 149–150	90.29	7.57	54.80
10H-6, 19–21	90.49	5.77	48.10
10H-6, 107–109	91.37	9.27	77.20
10H-7, 21–23	92.01	9.36	78.00
11H-1, 0–1	92.30	7.96	65.80

Table 6 (continued).

Core, section interval (cm)	Depth (mbsf)	Carbon (%)	Carbonate (%)
11H-1, 90–93	93.20	9.70	80.80
11H-2, 90–93	94.70	7.78	64.80
11H-3, 90–93	96.20	9.07	75.60
11H-4, 90–93	97.70	9.02	75.10
11H-5, 90–93	99.20	9.10	75.80
11H-6, 90–93	100.70	9.72	81.00
12H-1, 80–83	102.60	8.36	69.60
12H-1, 149–150	103.29	9.93	82.60
12H-2, 80–83	104.10	9.56	79.60
12H-3, 80–83	105.60	9.46	78.80
12H-4, 80–83	107.10	9.87	82.20
12H-5, 80–83	108.60	7.07	58.90
12H-6, 80–83	110.10	9.40	78.30
13H-1, 90–93	112.20	8.45	70.40
13H-2, 90–93	113.70	9.68	80.60
13H-3, 90–93	115.20	9.94	82.80
13H-4, 90–93	116.70	10.14	84.50
13H-5, 90–93	118.20	9.31	77.60
13H-5, 149–150	118.79	9.29	75.80
13H-6, 90–93	119.70	8.94	74.50
14H-1, 80–84	121.60	8.00	66.60
14H-1, 149–150	122.29	8.30	67.80
14H-2, 80–84	123.10	7.90	65.80
14H-3, 80–84	124.60	9.07	75.60
14H-4, 80–84	126.10	8.67	72.20
14H-5, 80–84	127.60	7.75	64.60
14H-6, 80–84	129.10	7.42	61.80
15H-1, 80–83	131.10	4.03	33.60
15H-2, 80–83	132.60	8.49	70.70
15H-3, 80–83	134.10	8.42	70.10
15H-4, 80–83	135.60	9.61	80.10
15H-5, 149–150	137.79	8.71	72.00
15H-6, 130–133	139.10	8.63	71.90
16H-1, 130–133	141.10	8.37	69.70
16H-3, 130–133	144.10	8.47	70.60
16H-5, 130–133	147.10	7.13	59.40
16H-5, 149–150	147.29	8.04	65.00
17H-1, 130–133	150.60	6.17	51.40
17H-3, 130–133	153.60	7.30	60.80
17H-5, 130–133	156.60	6.78	56.50
17H-5, 149–150	156.79	6.89	56.60
18H-1, 94–97	159.74	9.07	75.60
18H-3, 94–97	162.74	7.55	62.90
18H-4, 149–150	164.79	8.43	70.10
18H-5, 94–97	165.74	8.22	68.50
19H-1, 50–53	168.80	7.44	62.00
19H-3, 50–53	171.80	4.19	34.90
19H-4, 149–150	174.29	6.32	50.30
19H-5, 50–53	174.80	5.33	44.40
20H-1, 80–83	178.60	5.44	45.30
20H-3, 80–83	181.60	8.07	67.20
20H-4, 149–150	183.79	9.93	81.90
20H-5, 80–83	184.60	9.28	77.30
21H-1, 80–83	188.10	8.39	69.90
21H-3, 80–83	191.10	6.79	56.60
21H-5, 80–83	194.10	5.96	49.60
21H-5, 149–150	194.79	8.25	67.10
22H-1, 80–82	197.60	7.92	66.00
22H-3, 80–82	200.60	8.69	72.40
22H-5, 80–82	203.60	6.08	50.60
22H-5, 149–150	204.29	6.64	52.60
22H-7, 11–13	205.91	8.84	73.60
23H-1, 100–102	207.30	5.92	49.30
23H-3, 100–102	210.30	8.31	69.20
23H-3, 149–150	210.79	6.34	51.80
23H-5, 41–44	212.71	5.86	48.80
24H-2, 100–102	218.30	8.30	69.10
24H-4, 149–150	221.79	8.85	71.70
24H-5, 100–102	222.80	6.32	52.60
25H-1, 0–2	225.40	7.52	62.60
26H-2, 100–102	228.30	4.86	40.50
26H-3, 149–150	230.29	6.56	50.40
26H-5, 41–44	232.21	7.51	62.60
27H-2, 101–104	234.71	5.87	48.90
27H-3, 149–150	236.69	5.48	43.10
27H-5, 101–104	239.21	5.18	43.10
28H-2, 101–104	244.31	5.18	43.10
28H-3, 149–150	246.29	6.54	53.10

Table 6 (continued).

Core, section interval (cm)	Depth (mbsf)	Carbon (%)	Carbonate (%)
28H-5, 101–104	248.81	7.77	64.70
29H-2, 101–103	254.01	5.48	45.60
29H-5, 101–103	258.51	5.21	43.40
29H-5, 149–150	258.99	5.40	42.60
30H-2, 101–103	263.71	7.37	61.40
30H-5, 101–103	268.21	7.50	62.50
30H-5, 149–150	268.69	7.42	61.60
31H-2, 101–103	273.31	8.11	67.60
31H-4, 149–150	276.79	8.33	68.10
31H-5, 101–103	277.81	6.99	58.20
32H-2, 67–71	282.67	8.09	67.40
32H-5, 149–150	287.99	7.11	58.10
33H-3, 0–2	293.20	6.90	55.60
33H-4, 66–68	295.36	7.15	59.60
34H-2, 29–32	301.69	8.00	66.60
34H-3, 113–114	304.03	8.63	71.90
34H-5, 140–141	307.30	6.80	55.70
34H-6, 109–110	308.49	9.06	75.50
35H-2, 120–124	312.30	7.62	63.50
35H-3, 120–121	313.80	8.43	70.20
35H-5, 0–2	315.60	9.29	75.80
35H-5, 120–121	316.80	8.36	69.60
36H-2, 101–104	321.81	10.01	83.40
36H-5, 62–66	325.92	7.80	65.00
36H-6, 149–150	328.29	9.36	77.50
37H-2, 105–108	331.55	7.94	66.10
37H-5, 111–113	336.11	7.16	59.60
37H-5, 149–150	336.49	7.32	59.90
38H-2, 51–52	340.71	7.30	60.80
38H-3, 149–150	343.19	7.39	60.50
38H-5, 27–30	344.97	8.43	70.20
39H-2, 62–64	350.52	9.06	75.50
39H-2, 149–150	351.39	9.25	72.90
39H-4, 38–42	353.28	8.61	71.70
40H-2, 87–89	360.47	8.28	69.00
40H-5, 149–150	365.59	7.81	61.10
40H-6, 92–94	366.52	8.56	71.30
41H-1, 0–1	367.80	8.11	64.30
41H-2, 72–74	370.06	7.92	66.00
41H-6, 31–39	375.72	9.04	75.30
42H-3, 149–150	381.89	8.99	70.40
42H-4, 69–71	382.59	8.39	69.90
42H-6, 59–61	385.49	8.01	66.70
42H-7, 47–48	386.87	8.87	69.10
43H-3, 74–76	390.84	9.02	75.10
43H-5, 72–75	393.82	7.87	65.60
43H-5, 149–150	394.59	8.60	66.90
44H-1, 115–118	397.55	7.27	60.60
44H-5, 91–94	403.31	9.23	76.90
44H-6, 0–2	403.90	8.29	65.60
45H-2, 0–2	407.50	8.15	63.20
45H-2, 59–61	408.09	9.69	80.70
45H-1, 0–2	409.00	9.22	76.80
46H-1, 79–80	416.49	11.49	91.20
48H-1, 68–69	435.58	12.32	98.90

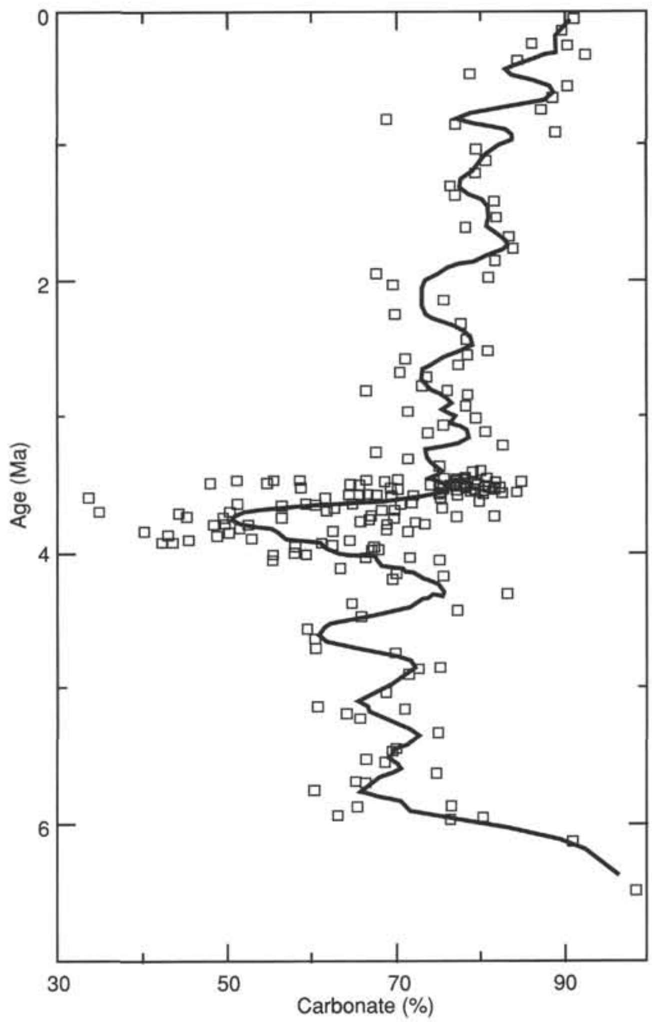

Figure 26. Changes in percentages of carbonate content as a function of age. Line represents a five-point, weighted average of data interpolated to a common sampling interval of 100,000 yr.

Porosity

Porosity was one index property determined from discrete core samples using a mass balance and a pycnometer (Table 10). A graph of porosity vs. depth is shown in Figure 30B. Similarly, water content, derived from the same set of index property measurements, is plotted in Figure 30C. Water content plotted vs. porosity is depicted in Figure 32. The tight linear clustering of data points indicates fairly high precision in our measurements of wet volume, which is the most uncertain of the mass and volume measurements that are used for calculating porosity.

Unique Distribution Pattern of Index Properties

In general, bulk density of sediment increases with burial depth because porosity and water content decrease continuously with overburden pressure. The index properties in Site 815 reveal an unusual distribution pattern. In the top 40 mbsf, bulk density decreases downward, while porosity and water content remain constant at a rate proportional to the degree of compaction. Between 40 and 117 mbsf, seawater was expelled; thus, index properties change with a continuous pattern downward. Between 117 and 320 mbsf (covering most of the section at Site 815), index properties remain more or less constant. This unusual feature indicates a sedimentary sequence that was rapidly deposited, such as a thick turbidite or slumped sequence. In combination with the overlying section, this sequence has a sufficiently low permeability for the sediment to be almost undrained and for compaction to be inhibited. In other words, the uniform distribution of index properties between 117 and 320 mbsf is the result of a high sedimentation rate. Below 320 mbsf, index properties exhibit a normal pattern.

Electrical Resistivity Formation Factor

We measured the formation factor at three intervals in core sections from Hole 815A (see Table 12 and Figs. 30 and 32). The scatter in the plot of formation factor vs. porosity (Fig. 32B) raises a concern that formation factor, as we measured it,

Table 7. Volatile hydrocarbon data from headspace analysis at Site 815.

Core, section, interval, (cm)	Depth (mbsf)	Sample	Volume (mL)	Gas chromato.	C_1 (ppm)	C_2 (ppm)	C_3 (ppm)
133-815A-							
1H, 149–150	4.49	HS	5	CAR132	2	0	0
2H-5, 149–150	14.29	HS	5	CAR132	2	0	0
3H-5, 149–150	23.79	HS	5	CAR132	2	0	0
4H-5, 149–150	33.29	HS	5	CAR132	2	0	0
5H-5, 149–150	42.79	HS	5	CAR132	3	0	0
6H-5, 149–150	52.29	HS	5	CAR132	2	0	0
7H-5, 149–150	61.79	HS	5	CAR132	2	0	0
8H-5, 149–150	71.29	HS	5	CAR132	2	0	0
9H-5, 149–150	80.79	HS	5	CAR132	2	0	0
10H-5, 149–150	90.29	HS	5	CAR132	2	0	0
11H-1, 0–1	92.3	HS	5	CAR132	2	0	0
12H-1, 149–150	103.29	HS	5	CAR132	2	0	0
13H-5, 149–150	118.79	HS	5	CAR132	3	0	0
14H-1, 149–150	122.29	HS	5	CAR132	2	0	0
15H-5, 149–150	137.79	HS	5	CAR132	3	0	0
16H-5, 149–150	147.29	HS	5	CAR132	2	0	0
17H-5, 149–150	156.79	HS	5	CAR132	3	0	0
18H-4, 149–150	164.79	HS	5	CAR132	4	0	0
19H-4, 149–150	174.29	HS	5	CAR132	4	0	0
20H-4, 149–150	183.79	HS	5	CAR132	5	1	0
21H-5, 149–150	194.79	HS	5	CAR132	5	1	0
22H-5, 149–150	204.29	HS	5	CAR132	7	1	0
23H-3, 149–150	210.79	HS	5	CAR132	5	0	0
24H-4, 149–150	221.79	HS	5	CAR132	9	1	0
25H-CC, 0–2	225.4	HS	5	CAR132	4	0	0
26X-3, 149–150	230.29	HS	5	CAR132	7	1	0
27X-3, 149–150	236.69	HS	5	CAR132	4	0	0
28X-3, 149–150	246.29	HS	5	CAR132	5	0	0
29X-5, 149–150	258.99	HS	5	CAR132	3	0	0
30X-5, 149–150	268.69	HS	5	CAR132	2	0	0
31X-4, 149–150	276.79	HS	5	CAR132	2	0	0
32X-5, 149–150	287.99	HS	5	CAR132	2	0	0
33X-3, 1–2	293.21	HS	5	CAR132	2	0	0
33X-CC, 0–2	296.1	HS	5	CAR132	2	0	0
34X-5, 140–141	307.3	HS	5	CAR132	4	0	0
35X-5, 0–2	315.6	HS	5	CAR132	3	0	0
36X-6, 149–150	328.29	HS	5	CAR132	6	0	2
37X-5, 149–150	336.49	HS	5	CAR132	8	0	2
38X-3, 149–150	343.19	HS	5	CAR132	5	0	0
39X-2, 149–150	351.39	HS	5	CAR132	7	1	0
40X-5, 149–150	365.59	HS	5	CAR132	4	0	0
41X-1, 0–1	367.8	HS	5	CAR132	3	0	0
42X-3, 149–150	381.89	HS	5	CAR132	7	1	0
42X-7, 47–48	386.87	HS	5	CAR132	3	0	0
43X-5, 149–150	394.59	HS	5	CAR132	3	0	0
44X-6, 0–2	403.9	HS	5	CAR132	1	0	0
45X-2, 0–2	407.5	HS	5	CAR132	7	1	0
45X-CC, 0–2	409.0	HS	5	CAR132	1	0	0
46X-1, 79–80	416.49	HS	5	CAR132	2	0	0
48X-1, 68–69	435.58	HS	5	CAR132	5	0	0

HS = headspace sample.

may not be a good substitute for porosity. One should compare this plot with Figure 124 from Leg 131 (Shipboard Scientific Party, 1991), where scientists during Leg 131, apparently using the same apparatus that we used, obtained more clearly the expected logarithmic relationship described in the "Explanatory Notes" chapter (this volume). In spite of the large scatter in our data, we plotted log formation factor vs. log porosity and were able to fit a linear curve to these data with a slope of −0.4 (Fig. 32C). Not only is there large scatter in the data, but the value of −0.4 is not in the expected range of −1 to −2. Part of the problem may be that we did not measure the great range of porosities encountered during Leg 131, where porosities ranged from 0.25 to 0.75. If one compares only the portion of Figure 124 with porosities in the range of 0.45 to 0.65 to the range of porosities observed at Site 815, then the two plots are similar. In fact, Figure 124 shows twice the scatter of formation factor at a porosity of 45%, compared with that in our Figure 32B.

Shear Strength

We measured shear strength in the upper section of this hole (Table 13 and Fig. 30F). The great amount of variability deep in the section may possibly result from rapid draining of some lithologies of the split cores.

DOWNHOLE MEASUREMENTS

Reliability of Logs

Problems with the Schlumberger data acquisition system limited logging of Hole 815A to the seismic stratigraphy combination tool string and prevented our running normal upgoing logs for part of the hole. Downgoing logs were satisfactory for resistivity, sonic, and spectral gamma-ray tools (Figs. 33 and 34). However, the design of the density tool only allows for continuous pad contact for upgoing logs. Consequently, density data were unusable for these downgo-

Table 8. Concentrations of total organic carbon, inorganic carbon, total carbon, total nitrogen, and sulfur in headspace samples from Site 815.

Core, section, interval (cm)	Depth (mbsf)	Sample	Total organic carbon (%)	Total inorganic carbon (%)	Total carbon (%)	Total nitrogen (%)	Total sulfur (%)	TOC/N ratio	TOC/S ratio
133-815A-									
1H-3, 149–150	4.49	HS	0	10.8	10.8	0	0		
2H-5, 149–150	14.29	HS	0	9.25	9.25	0			
3H-5, 149–150	23.79	HS	0.1	9.8	9.9	0	0		
4H-5, 149–150	33.29	HS	0.1	9.7	9.8	0	0		
5H-5, 149–150	42.79	HS	0.1	9.4	9.5	0	0		
6H-5, 149–150	52.29	HS	0.1	8	8.1	0	0		
7H-5, 149–150	61.79	HS	0.2	8.9	9.1	0	0		
8H-5, 149–150	71.29	HS	0.1	9.5	9.6	0	0		
9H-5, 149–150	80.79	HS	0.25	7.05	7.3	0	0		
10H-5, 149–150	90.29	HS	1	6.6	7.6	0	0		
11H-1, 0–1	92.3	HS	0.05	7.9	7.95	0	0		
12H-1, 149–150	103.29	HS	0	9.9	9.9	0	0		
13H-5, 149–150	118.79	HS	0.2	9.1	9.3	0	0		
14H-1, 149–150	122.29	HS	0.15	8.14	8.3	0	0		
15H-5, 149–150	137.79	HS	0.05	8.65	8.7	0	0		
16H-5, 149–150	147.29	HS	0.25	7.8	8.05	0	0		
17H-5, 149–150	156.79	HS	0.1	6.8	6.9	0	0		
18H-4, 149–150	164.79	HS	0	8.4	8.4	0	0		
19H-4, 149–150	174.29	HS	0.3	6	6.3	0	0		
20H-4, 149–150	183.79	HS	0.1	9.8	9.9	0	0		
21H-5, 149–150	194.79	HS	0.2	8.05	8.25	0	0		
22H-5, 149–150	204.29	HS	0.35	6.3	6.65	0	0		
23H-3, 149–150	210.79	HS	0.1	6.2	6.3	0	0		
24H-4, 149–150	221.79	HS	0.25	8.6	8.85	0	0		
25H-CC, 0–2	225.4	HS	0.2	7.5	7.7	0	0		
26X-3, 149–150	230.29	HS	0.5	6.05	6.55	0	0		
27X-3, 149–150	236.69	HS	0.3	5.2	5.5	0	0		
28X-3, 149–150	246.29	HS	0.15	6.4	6.55	0	0		
29X-5, 149–150	258.99	HS	0.3	5.1	5.4	0	0		
30X-5, 149–150	268.69	HS	0.05	7.4	7.45	0	0		
31X-4, 149–150	276.79	HS	0.15	8.2	8.35	0	0		
32X-5, 149–150	287.99	HS	0.15	7	7.15	0	0		
33X-3, 0–2	293.2	HS	0.25	6.65	6.9	0	0		
34X-5, 140–141	307.3	HS	0.1	6.7	6.8	0	0		
35X-5, 0–2	315.6	HS	0.2	9.1	9.3	0	0		
36X-6, 149–150	328.29	HS	0.05	9.3	9.35	0	0		
37X-5, 149–150	336.49	HS	0.15	7.2	7.35	0	0		
38X-3, 149–150	343.19	HS	0.15	7.25	7.4	0	0		
39X-2, 149–150	351.39	HS	0.5	8.75	9.25	0.04	0.24	12	2.1
40X-5, 149–150	365.59	HS	0.45	7.35	7.8	0.03	0.29	15	1.6
41X-1, 0–1	367.8	HS	0.4	7.7	8.1	0.01	0.33	39	1.2
42X-3, 149–150	381.89	HS	0.55	8.45	9	0.01	0.31	54	1.7
42X-7, 47–48	386.87	HS	0.6	8.3	8.9	0	0.25		2.3
43X-5, 149–150	394.59	HS	0.55	8.05	8.6	0.02	0.46	28	1.2
44X-6, 0–2	403.9	HS	0.4	7.9	8.3	0	0.33		1.3
45X-2, 0–2	407.5	HS	0.55	7.6	8.15	0.01	0.31	56	1.8
45X-CC, 0–2	409	HS	0.5	9.2	9.7	0.01	0.12	50	4.1
46X-1, 79–80	416.49	HS	0.55	10.95	11.5	0.02	0	27	
48X-1, 68–69	435.58	HS	0.45	11.85	12.3	0	0		

HS = headspace sample.

ing logs, which resulted in gaps in coverage, as seen in Figure 33. Problems with the Schlumberger unit permitted only a few meters of uncalibrated geochemical logging. Furthermore, these problems precluded our use of the FMS because of our inability to control the opening of the caliper and the side-wall resistivity pads.

Hole size and condition are the most important controls for accuracy of logs from Hole 815A, and caliper is the best indication of these parameters. Most of the logged interval is less than 14 in. (36 cm), only slightly larger than a bit size of 12 in.; these were the best conditions encountered during Leg 133. Consequently, most of the lithodensity run obtained only satisfactory pad contact against the borehole wall. However, the density log does show some swings to unreliably low values (Fig. 33). We observed that when we used the density compensation factor, which attempts to correct for inadequate pad contact, we applied corrections so large that compensation was only approximate. These swings correlate with the caliper high points that indicated washout in these regions. This loss of strength/cohesion correlates with resistivity and velocity cycles, which indicate a change in porosity and/or composition.

Most other logs did not require pad contact and thus are relatively insensitive to changes in borehole size. Two minor exceptions are the gamma-ray and resistivity logs, which may have changed slightly before post-cruise borehole correction.

As is often the case with ODP holes, the initial sonic logs from Hole 815A exhibited several zones in which cycle skipping caused unreliable swings in apparent velocity. Reprocessing (see "Explanatory Notes" chapter, this volume) appears to have removed all unreliable data, and we think that the reprocessed velocity log in Figure 33 is of very good quality.

Velocity, Resistivity, and Density

Velocity, resistivity, and formation factor correlate strongly throughout most of the logged interval at Hole 815A

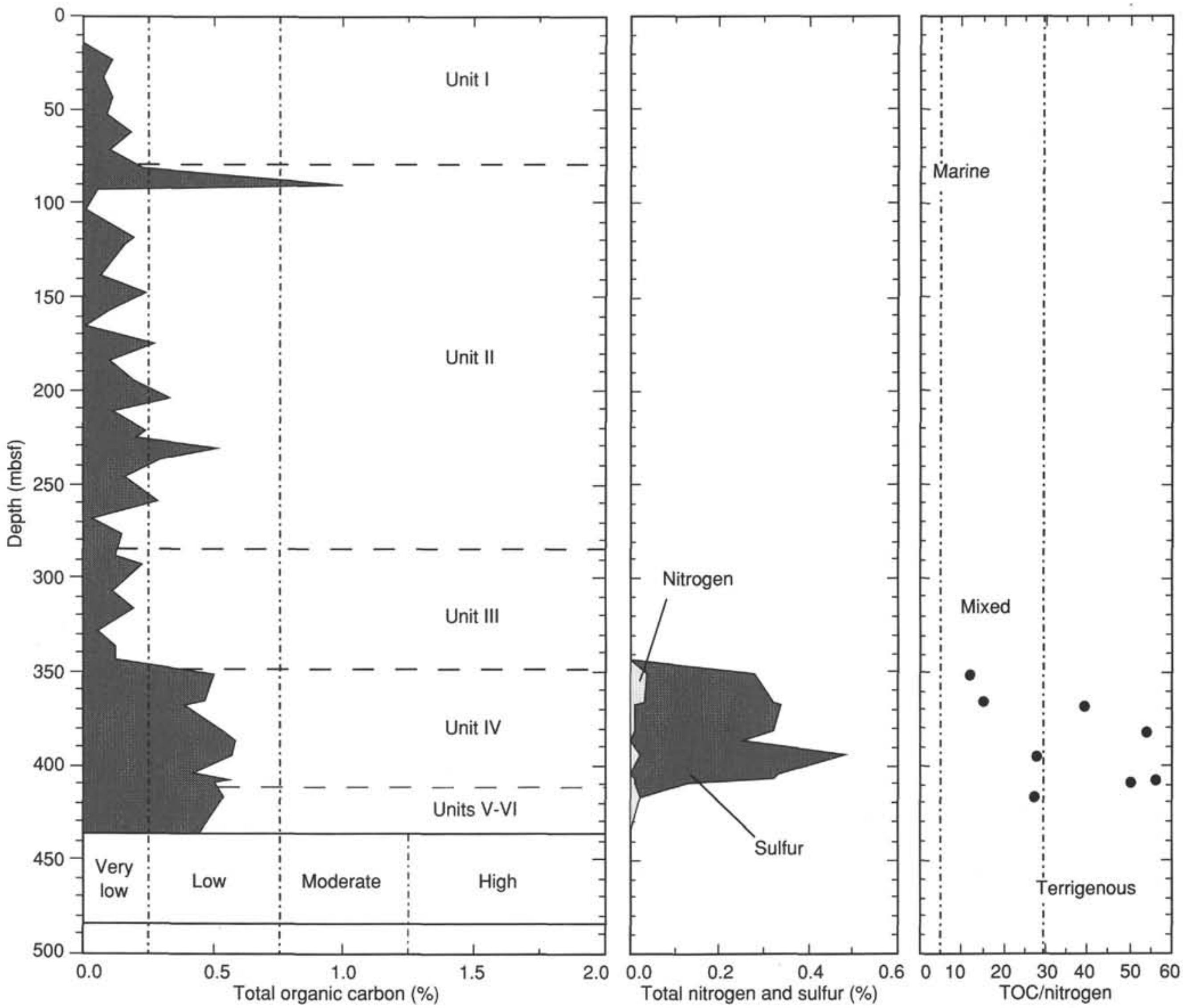

Figure 27. Distribution with depth of concentrations of total organic carbon, nitrogen, and sulfur in headspace samples from Site 815.

Table 9. Rock-Eval pyrolysis data from headspace samples at Site 815.

Core, section, interval (cm)	Depth (mbsf)	Sample	Weight (mg)	T_{max} (°C)	S_1 (kg HC/t)	S_2 (kg HC/t)	S_3 (kg CO_2t)	TOC (%)*	Hydrogen index (mg HC/g TOC)	Oxygen index (mg CO_2/g TOC)
133-815A-										
10H-5, 149–150	90.29	HS	99.5	392	0.02	0.88	2.85	0.99	91	288
26X-3, 149–150	230.29	HS	99.7	400	0.07	1.5	2.9	0.51	308	569
39X-2, 149–150	351.39	HS	101.4	376	0	0.8	2.26	0.5	160	452
40X-5, 149–150	365.59	HS	102.1	315	0.04	0.95	2.72	0.47	211	579
42X-3, 149–150	381.89	HS	100.1	363	0.11	1.47	2.47	0.54	293	457
42X-7, 47–48	386.87	HS	97.3	405	0.01	0.95	2.65	0.58	166	457
43X-5, 149–150	394.59	HS	103.9	405	0.08	1.92	2.59	0.57	351	454
45X-2, 0–2	407.5	HS	100.7	366	0.02	0.96	2.7	0.56	175	482
46X-1, 79–80	416.49	HS	99	385	0.13	1.29	1.05	0.54	263	194
48X-1, 68–69	435.58	HS	99.1		0.06	0.38	0.57	0.45	110	127

HS = headspace sample; TOC*: total organic carbon = total carbon (NCS Analyzer) − total inorganic carbon (Coulometer).

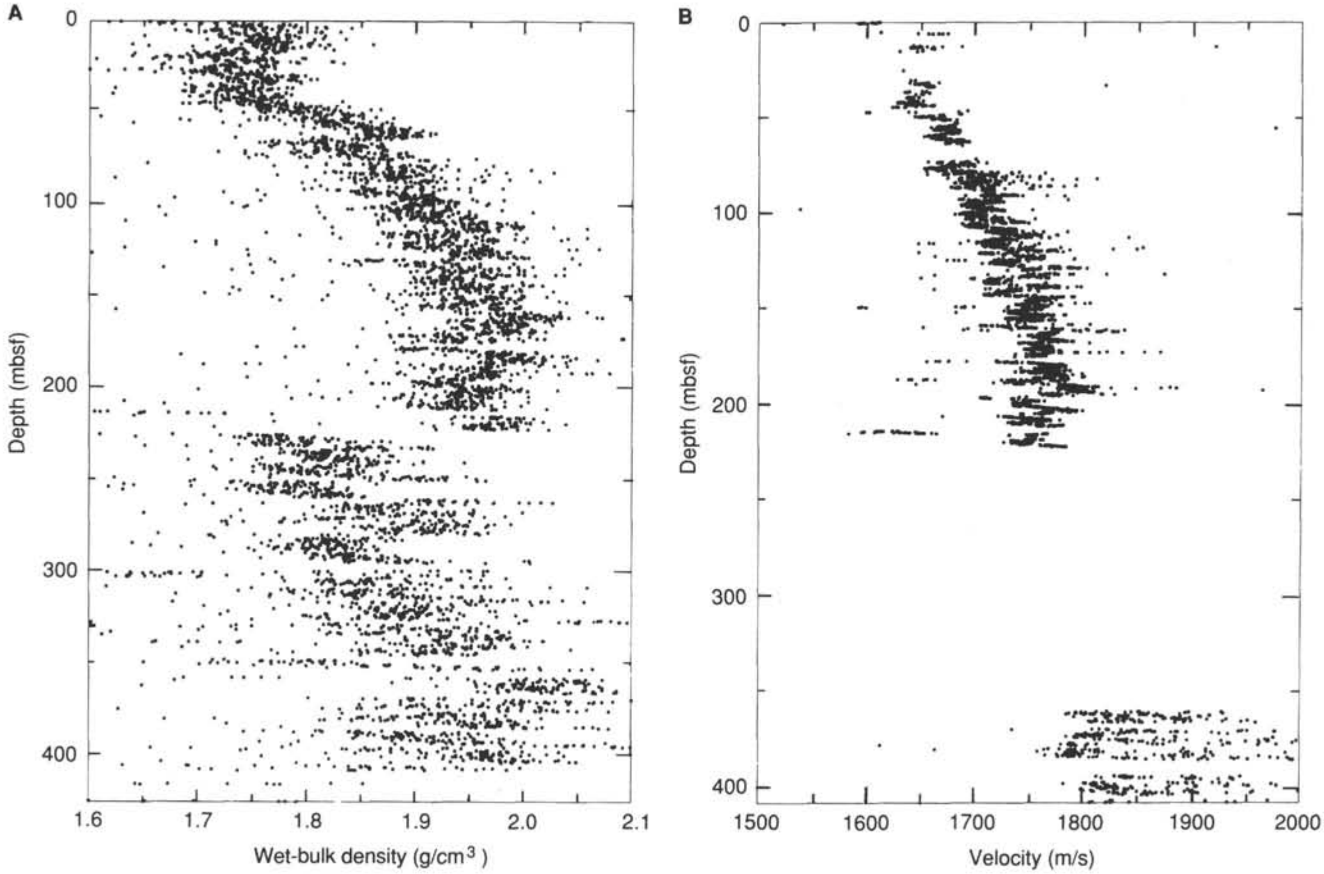

Figure 28. **A.** Unfiltered GRAPE bulk-density measurements for Site 815. Because of varying rates of motion of the core through the GRAPE system, multiple measurements often occurred at the same position in the core. All data points displayed in Figures 28 and 29 are averages of all data in 7.5-cm blocks along the core. **B.** MST sonic velocity for whole-round cores from Hole 815.

(Figs. 33 and 35). Log responses here have been controlled more by changes in porosity than by lithologic variability.

Increases in velocity and density with depth (Fig. 33) generally follow a simple compaction profile, suggesting that mechanical compaction is dominant over diagenesis and grain-size fluctuations for controlling the overall porosity profile at this site.

At this site, the feature most worthy of note is the cyclicity in the three logs in the interval from 130 to 270 mbsf. Density values have been degraded by washouts, which can be seen in the caliper log; this is unfortunate, but serves to confirm that substantial petrophysical changes occurred within this interval and are controlled by porosity. These changes are similar in amplitude and style to the cyclicity seen in resistivity and sonic logs that were obtained at Site 646 during Leg 105, which were shown to be climatically controlled (Jarrard and Arthur, 1989).

The reprocessed sonic log has been converted to an integrated traveltime log (Fig. 36) to facilitate depth-to-time conversion for comparison with Site 815 data having seismic facies. For the unlogged interval between the seafloor and 88.5 mbsf, we used a simple linear interpolation between water velocity at the seafloor and the first log value at 88.5 mbsf. We subjectively estimated an error of less than 5 ms that is associated with uncertainties of velocities in the top 88.5 mbsf.

The reprocessed sonic and density logs were used to calculate a synthetic seismogram, based on the algorithm described in the "Explanatory Notes" chapter (this volume). This synthetic seismogram is shown and interpreted in the "Seismic Stratigraphy" section (this chapter).

Resistivity

The resistivity logs shown in Figure 33 have been divided into six distinct zones, using criteria of log value and character as follows:

1. A cyclic zone between 110 and 271 mbsf, where resistivity alternates from approximately 0.6 to 1.0 ohm-m. These cycles can be seen in the velocity, caliper, and density logs, in addition to the resistivity logs, confirming that these responses indicate porosity variations. This zone has been identified as having a high rate of sedimentation, with 210 m being deposited in 730 k.y. (see "Biostratigraphy" section, this chapter).

2. Between 271 and 355 mbsf, values are 0.8 to 1.0 ohm-m, with only slight variability, with the exception of an isolated peak at 295 m that has been identified as dolomite in the geochemical analysis, but is not evident in core descriptions.

3. From 355 to 408 mbsf, resistivity rises by 10%, but does not change in character compared to the zone above. A similar resistivity/velocity peak from 382 to 383 mbsf to that at 295 mbsf, described as dolomite above, was not detected by geochemical core analysis or lithological description.

4. From 408 to 415 mbsf, resistivity increases, suggesting a major lithological change.

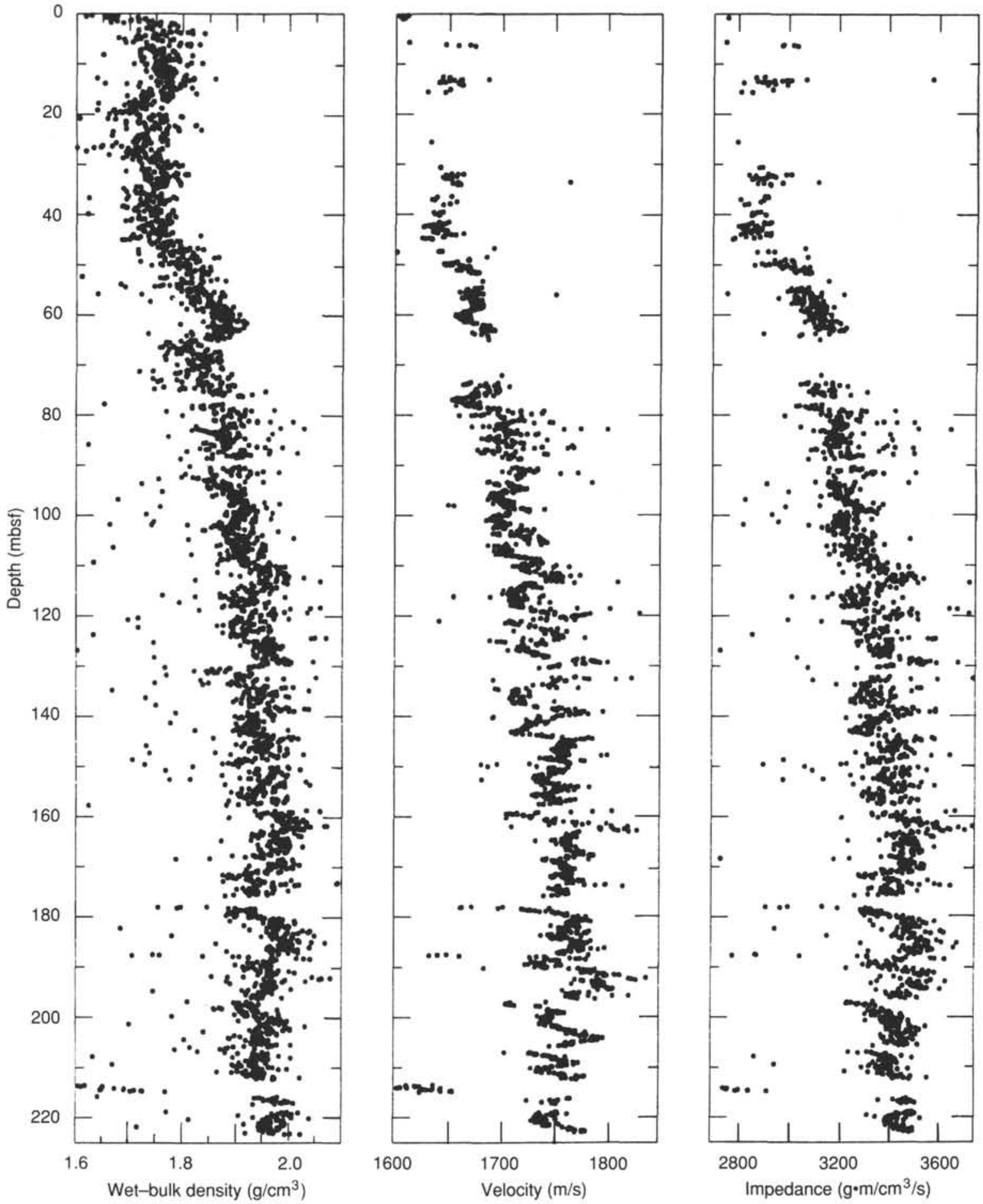

Figure 29. MST sonic velocity and bulk density data for the upper 220 m of Hole 815A along with computed impedance (the product of velocity and density). These data are plotted at an expanded scale (compared to Figure 31) to show the signal that lies within the downhole cluster of data values.

5. From 415 to 425 mbsf, resistivity decreases dramatically to below the average value of Zones 2 and 3 above, whereas velocity is less affected, which clearly suggests another lithological change at a higher porosity.

6. Below 425 mbsf, resistivity increases to a level that suggests a return to the lithology of Zone 4 above, although the record is curtailed.

The differences between these three resistivity log types have been attributed to different responses of the three sondes. This effect has been accentuated by the large hole diameter. The general relative position of these three logs is similar to the situation at Sites 812 and 814, where deep induction provides the highest resistivities and the SFL the lowest, with the medium induction log providing intermediate

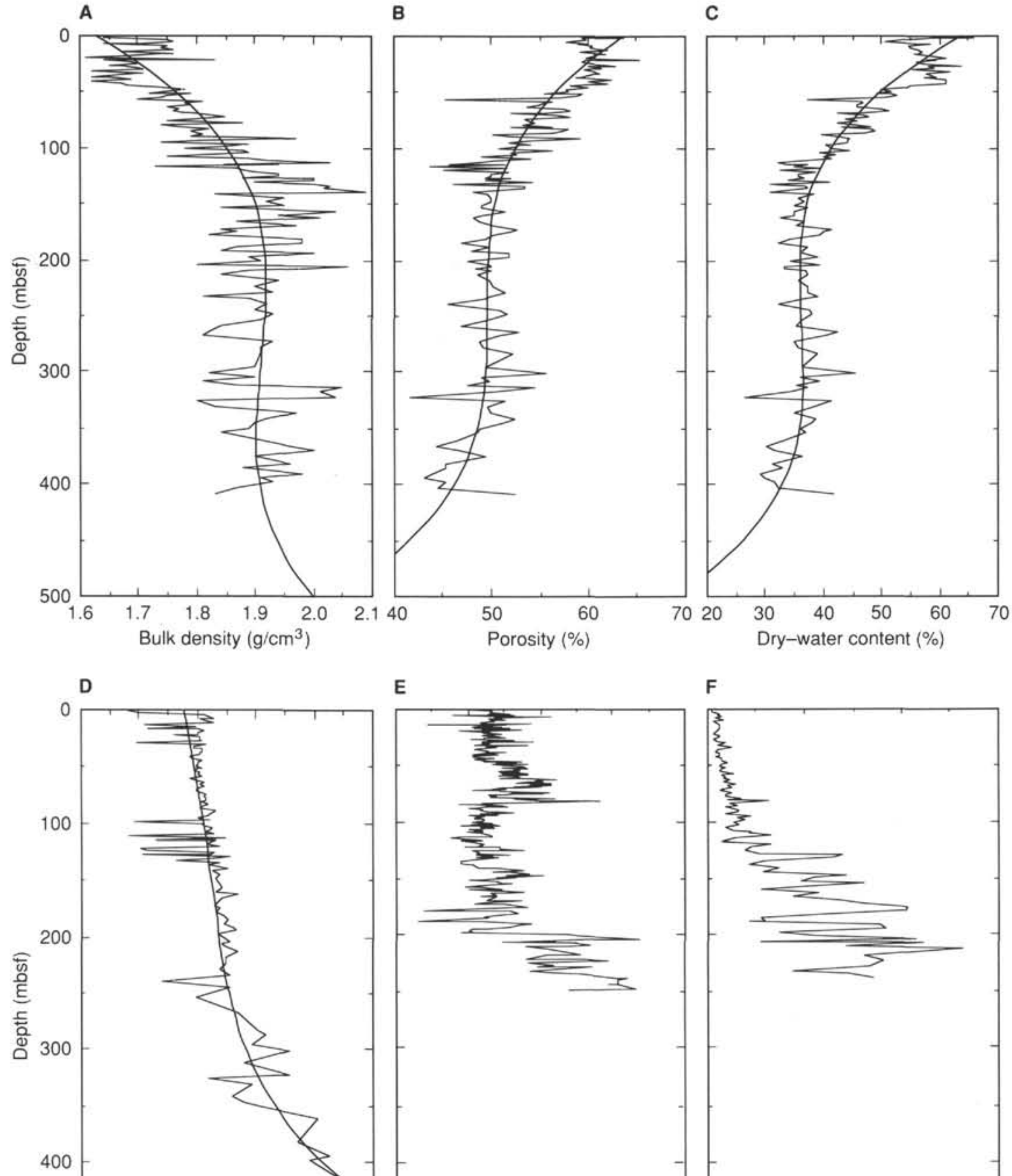

Figure 30. Physical properties data vs. depth, Site 815. **A.** Wet bulk density derived from mass and volume measurements of discrete core samples (pycnometer). The third-order least-squares regression is $Y = 1.6280 + 3.3407 \times 10^{-3}X - 1.2215 \times 10^{-5}X^2 + 1.4052 \times 10^{-8}X^3$, where Y = bulk density (g/cm^3), X = depth (mbsf), and regression coefficient, $R = 0.78$. **B.** Porosity; third-order, least-squares regression is $Y = 63.747 - 0.17392X + 7.1169 \times 10^{-4}X^2 - 9.6777 \times 10^{-7}X^3$, where Y = porosity (%), X = depth (mbsf), and regression coeficient, $R = 0.858$. **C.** Dry-water content; dry water content is water mass/dry sediment mass. Data are derived from mass measurements of discrete samples from cores before and after drying. The third-order, least-squares regression is $Y = 64.009 - 0.34638X + 1.3855 \times 10^{-3}X^2 - 1.7878 \times 10^{-6}X^3$, where Y = dry-water content (%), X = depth (mbsf), and regression coefficient, $R = 0.911$. **D.** *P*-wave velocity; data were derived from Hamilton frame measurements of discrete samples from cores. Values of less than 1.5 km/s probably result from rapid draining of permeable sands. The fourth-order, least-squares regression is $Y = 1.5571 + 5.7484 \times 10^{-4}X + 1.5897 \times 10^{-6}X^2 - 1.5266 \times 10^{-8}X^3 + 3.7584 \times 10^{-11}X^4$, where Y = *P*-wave velocity (km/s), X = depth (mbsf), and regression coefficient, $R = 0.798$. **E.** Electrical resisitivity formation factor. **F.** Shear strength.

Table 10. Index properties data for Site 815.

Core, section, interval (cm)	Depth (mbsf)	Bulk density (g/cm^3)	Grain density (g/cm^3)	Porosity (%)	Water content (%)	Void ratio
133-815A-						
1H-1, 101–104	1.01	1.64	2.61	63.7	66.0	1.76
1H-2, 101–104	2.51	1.64	2.59	59.4	58.9	1.47
1H-3, 101–104	4.01	1.75	2.72	59.7	53.7	1.48
1H-4, 101–104	5.51	1.76	2.70	57.7	50.7	1.37
1H-5, 31–34	6.31	1.71	2.61	60.0	56.3	1.50
2H-1, 101–104	7.81	1.64	2.46	58.9	58.3	1.43
2H-2, 101–104	9.31	1.75	2.43	60.4	54.7	1.52
2H-3, 101–104	10.81	1.74	2.62	60.3	55.0	1.52
2H-4, 101–104	12.31	1.76	2.74	62.0	56.3	1.63
2H-5, 81–84	13.61	1.67	2.68	59.1	57.0	1.45
2H-6, 101–104	15.31	1.76	2.83	61.8	56.3	1.62
2H-7, 41–44	16.21	1.74	2.67	60.7	55.7	1.54
3H-1, 101–104	17.31	1.69	2.53	60.8	58.4	1.55
3H-2, 101–104	18.81	1.61	2.64	59.8	61.3	1.49
3H-3, 101–104	20.31	1.83	2.65	65.4	57.8	1.89
3H-4, 101–104	21.81	1.64	2.50	59.8	59.6	1.49
3H-5, 81–84	23.11	1.69	2.52	59.3	55.9	1.46
3H-6, 101–104	24.81	1.70	2.67	60.7	57.5	1.54
3H-7, 58–61	25.88	1.65	2.79	62.8	63.9	1.69
4H-1, 118–121	26.98	1.67	2.50	60.1	58.2	1.51
4H-2, 101–104	28.31	1.70	2.70	61.5	59.1	1.60
4H-3, 101–104	29.81	1.71	2.65	59.6	55.5	1.48
4H-4, 101–104	31.31	1.62	2.63	60.7	62.0	1.54
4H-5, 101–104	32.81	1.71	2.44	61.2	57.7	1.58
4H-6, 101–104	34.31	1.70	2.65	60.8	57.7	1.55
5H-1, 101–104	36.31	1.62	2.49	59.2	59.6	1.45
5H-2, 101–104	37.81	1.65	2.76	58.8	57.5	1.43
5H-3, 101–104	39.31	1.69	2.72	62.5	61.0	1.67
5H-4, 101–104	40.81	1.62	2.61	60.0	61.0	1.50
5H-5, 101–104	42.31	1.67	2.47	62.1	61.3	1.64
5H-6, 101–104	43.81	1.68	2.72	58.2	55.0	1.39
6H-1, 101–104	45.81	1.74	2.68	60.1	54.5	1.51
6H-2, 101–104	47.31	1.78	2.63	57.8	49.9	1.37
6H-3, 101–104	48.81	1.75	2.64	58.0	51.5	1.38
6H-4, 101–104	50.31	1.72	2.55	55.5	49.4	1.25
6H-5, 101–104	51.81	1.79	2.79	59.4	51.7	1.47
6H-6, 101–104	53.31	1.75	2.69	59.0	52.7	1.44
7H-1, 101–104	55.31	1.74	2.63	57.2	50.6	1.34
7H-2, 101–104	56.81	1.70	2.69	45.4	37.5	0.83
7H-3, 101–104	58.31	1.81	2.71	56.3	46.7	1.29
7H-4, 101–104	59.81	1.78	2.70	55.6	47.0	1.25
7H-5, 101–104	61.31	1.79	2.76	54.8	45.8	1.21
7H-6, 101–104	62.81	1.75	2.73	53.7	46.0	1.16
8H-1, 101–104	64.81	1.77	2.62	57.6	49.9	1.36
8H-2, 101–104	66.31	1.76	2.53	58.2	51.3	1.39
8H-3, 101–104	67.81	1.78	2.68	55.7	47.0	1.26
8H-4, 101–104	69.31	1.79	2.65	52.1	42.5	1.09
8H-5, 101–104	70.81	1.82	2.61	56.7	47.0	1.31
8H-6, 101–104	72.31	1.85	2.52	58.2	47.8	1.40
9H-1, 101–104	74.31	1.80	2.76	53.4	43.8	1.14
9H-2, 101–104	75.81	1.75	2.71	53.8	46.0	1.16
9H-3, 101–104	77.31	1.88	2.63	54.5	42.4	1.20
9H-4, 101–104	78.81	1.74	2.53	53.2	45.8	1.14
9H-5, 91–94	80.21	1.77	2.74	56.3	48.3	1.29
9H-6, 101–104	81.81	1.77	2.69	52.1	43.2	1.09
10H-1, 50–53	83.30	1.82	2.61	57.9	48.3	1.38
10H-2, 50–53	84.80	1.79	2.39	57.4	48.9	1.35
10H-3, 50–53	86.30	1.80	2.71	56.3	47.3	1.29
10H-4, 50–53	87.80	1.81	2.72	50.2	39.7	1.01
10H-5, 50–53	89.30	1.79	2.58	52.3	42.6	1.10
10H-6, 50–53	90.80	1.97	2.33	59.1	44.5	1.44
11H-1, 90–93	93.20	1.81	2.63	54.1	44.3	1.18
11H-2, 90–93	94.70	1.74	2.43	51.8	44.0	1.08
11H-3, 90–93	96.20	1.89	2.74	54.1	41.6	1.18
11H-4, 90–93	97.70	1.88	2.68	52.8	40.5	1.12
11H-5, 90–93	99.20	1.85	2.55	52.7	41.2	1.11
11H-6, 90–93	100.70	1.78	2.35	50.9	41.4	1.04
12H-1, 80–83	102.60	1.88	2.71	56.3	44.4	1.29
12H-2, 80–83	104.10	1.89	2.53	52.1	39.4	1.09
12H-3, 80–83	105.60	1.82	2.30	52.6	42.0	1.11
12H-4, 80–83	107.10	1.75	2.72	48.9	40.1	0.96
12H-5, 80–83	108.60	1.89	2.65	54.1	41.4	1.18
12H-6, 80–83	110.10	1.92	2.60	50.4	36.7	1.01
13H-1, 90–93	112.20	2.03	2.47	48.5	32.4	0.94
13H-2, 90–93	113.70	1.85	2.70	45.8	34.1	0.84
13H-3, 90–93	115.20	1.94	2.76	51.5	37.2	1.06
13H-4, 90–93	116.70	1.73	2.69	43.7	35.0	0.78
13H-5, 90–93	118.20	1.87	2.77	51.6	39.4	1.07
13H-6, 90–93	119.70	1.88	2.70	45.1	32.6	0.82

Table 10 (continued).

Core, section, interval (cm)	Depth (mbsf)	Bulk density (g/cm^3)	Grain density (g/cm^3)	Porosity (%)	Water content (%)	Void ratio
14H-1, 80–83	121.60	1.90	2.60	51.8	38.7	1.07
14H-2, 80–83	123.10	1.94	2.54	50.0	35.8	1.00
14H-3, 80–83	124.60	1.94	2.75	49.9	35.7	0.99
14H-4, 80–83	126.10	1.88	2.69	49.3	36.8	0.97
14H-5, 80–83	127.60	2.00	2.68	52.1	36.3	1.09
14H-6, 80–83	129.10	2.00	2.50	49.4	33.8	0.98
15H-1, 80–83	131.10	1.90	2.74	54.2	41.2	1.19
15H-2, 80–83	132.60	2.00	2.65	46.2	31.0	0.86
15H-3, 80–83	134.10	2.03	2.88	53.5	37.1	1.15
15H-4, 80–83	135.60	2.02	2.51	53.5	37.3	1.15
15H-6, 80–83	138.60	2.09	2.74	48.2	31.0	0.93
16H-1, 130–133	141.10	1.83	2.67	49.5	38.4	0.98
16H-3, 130–133	144.10	1.95	2.65	50.1	35.6	1.00
16H-5, 130–133	147.10	1.92	2.53	50.1	36.5	1.00
17H-1, 130–133	150.60	1.95	2.76	49.0	34.8	0.96
17H-3, 130–133	153.60	1.84	2.67	48.9	37.4	0.96
17H-5, 130–133	156.60	2.04	2.60	51.4	34.8	1.06
18H-1, 94–97	159.74	1.94	2.47	49.0	34.9	0.96
18H-3, 94–97	162.74	2.01	2.73	48.1	32.5	0.93
18H-5, 94–97	165.74	1.87	2.68	48.8	36.5	0.95
19H-1, 50–53	168.80	1.97	2.65	50.2	35.4	1.01
19H-3, 50–53	171.80	1.84	2.44	52.6	41.3	1.11
19H-5, 50–53	174.80	1.87	2.68	52.1	40.1	1.09
20H-1, 80–83	178.60	1.82	2.72	50.2	39.5	1.01
20H-3, 80–83	181.60	1.98	2.62	49.3	34.2	0.97
20H-5, 80–83	184.60	1.98	2.42	46.9	32.1	0.88
21H-1, 80–83	188.10	1.87	2.76	49.7	37.5	0.99
21H-3, 80–83	191.10	1.84	2.73	47.9	36.4	0.92
21H-5, 80–83	194.10	2.00	2.77	51.9	36.3	1.08
22H-1, 80–83	197.60	1.89	2.70	51.9	39.1	1.08
22H-3, 80–83	200.60	1.91	2.64	47.6	34.3	0.91
22H-5, 80–83	203.60	1.80	2.44	49.8	39.5	0.99
22H-7, 11–14	205.91	2.06	2.72	50.0	33.1	1.00
23H-1, 101–104	207.31	1.99	2.74	48.3	33.1	0.94
23H-3, 101–104	210.31	1.89	2.69	49.9	37.0	1.00
23H-5, 41–44	212.71	1.84	2.42	48.6	37.3	0.95
24H-2, 101–104	218.31	1.94	2.75	49.8	35.7	0.99
24H-5, 101–104	222.81	1.90	2.75	50.3	37.3	1.01
26X-2, 101–104	228.31	1.93	2.62	51.5	37.5	1.06
26X-5, 41–44	232.21	1.81	2.53	49.8	39.2	0.99
27X-2, 101–104	234.71	1.89	2.79	49.4	36.5	0.98
27X-5, 91–94	239.11	1.92	2.68	45.6	32.2	0.84
28X-2, 101–104	244.31	1.90	2.55	50.9	37.7	1.04
28X-5, 101–104	248.81	1.93	2.71	51.7	37.9	1.07
29X-2, 101–104	254.01	1.91	2.69	49.5	36.3	0.98
29X-5, 101–104	258.51	1.84	2.52	47.0	35.3	0.89
30X-2, 101–103	263.71	1.82	2.69	52.8	42.3	1.12
30X-5, 101–103	268.21	1.81	2.70	50.9	40.5	1.04
31X-2, 101–103	273.31	1.93	3.15	48.7	34.8	0.95
31X-5, 101–103	277.81	1.91	2.10	49.1	35.7	0.96
32X-2, 67–71	282.67	1.91	2.69	52.3	39.0	1.10
33X-4, 66–68	295.36	1.90	2.63	49.3	36.3	0.97
34X-2, 29–32	301.69	1.82	2.57	55.7	45.6	1.26
34X-3, 112–113	304.02	1.90	2.35	48.9	35.9	0.96
34X-6, 108–110	308.48	1.81	2.43	49.8	39.3	0.99
35X-2, 120–124	312.30	1.87	2.57	47.5	35.3	0.91
35X-3, 118–120	313.78	2.05	2.87	54.5	37.4	1.20
35X-5, 118–120	316.78	2.01	2.64	50.6	34.7	1.03
36X-2, 100–104	321.80	2.04	2.68	41.6	26.4	0.71
36X-5, 62–66	325.92	1.80	2.52	51.4	41.4	1.06
37X-2, 103–108	331.53	1.83	2.53	49.5	38.3	0.98
37X-5, 111–113	336.11	1.97	2.75	49.9	35.1	1.00
38X-2, 52–53	340.72	1.92	2.57	52.4	38.6	1.10
38X-5, 27–31	344.97	1.90	2.85	51.2	38.1	1.05
39X-2, 62–64	350.52	1.89	2.69	48.8	36.1	0.95
39X-4, 38–41	353.28	1.84	2.64	48.6	37.0	0.95
40X-2, 87–90	360.47	1.91	2.74	46.6	33.4	0.87
40X-6, 100–103	366.60	1.96	2.79	44.3	30.1	0.80
41X-2, 72–74	370.06	2.00	2.77	46.7	31.4	0.88
41X-6, 31–39	375.72	1.90	2.73	49.4	36.3	0.98
42X-4, 69–72	382.59	1.96	2.64	45.4	31.1	0.83
42X-6, 59–61	385.49	1.88	2.52	45.4	32.8	0.83
43X-3, 74–76	390.84	1.98	2.79	43.9	29.3	0.78
43X-5, 72–75	393.82	1.91	2.70	43.0	29.9	0.75
44X-1, 114–117	397.54	1.93	2.61	45.4	31.7	0.83
44X-5, 91–94	403.31	1.87	2.70	44.5	32.3	0.80
45X-2, 57–60	408.07	1.83	2.89	52.4	41.6	1.10

Table 11. Compressional-wave velocity data at Site 815.

Core, section, interval (cm)	Depth (mbsf)	Distance (mm)	Traveltime (μs)	Velocity (m/s)
133-815A-				
1H-1, 101–104	1.01	27.67	22.54	1366
1H-2, 101–104	2.51	26.97	21.61	1397
1H-3, 101–104	4.01	28.72	20.17	1623
1H-5, 31–34	6.31	27.63	19.18	1655
2H-1, 101–104	7.81	29.02	20.50	1609
2H-2, 101–104	9.31	28.07	19.72	1628
2H-3, 101–104	10.81	27.89	19.32	1657
2H-4, 101–104	12.31	27.97	22.09	1415
2H-5, 81–84	13.61	29.19	20.77	1594
2H-6, 101–104	15.31	27.58	21.65	1428
2H-7, 41–44	16.21	28.76	20.39	1604
3H-1, 101–104	17.31	28.81	20.23	1623
3H-2, 101–104	18.81	28.98	20.55	1602
3H-3, 101–104	20.31	29.11	20.67	1599
3H-4, 101–104	21.81	27.76	20.71	1517
3H-5, 81–84	23.11	29.33	20.71	1608
3H-6, 101–104	24.81	28.67	20.26	1611
3H-7, 58–61	25.88	29.37	20.72	1609
4H-1, 118–121	26.98	28.76	20.28	1615
4H-2, 101–104	28.31	27.45	22.00	1394
4H-3, 101–104	29.81	28.33	19.88	1628
4H-4, 101–104	31.31	28.85	20.61	1589
4H-5, 101–104	32.81	29.41	21.00	1586
4H-6, 101–104	34.31	29.20	20.58	1612
5H-1, 101–104	36.31	27.98	19.76	1618
5H-2, 101–104	37.81	29.11	20.57	1608
5H-3, 101–104	39.31	27.58	19.62	1607
5H-4, 101–104	40.81	28.50	20.53	1576
5H-5, 101–104	42.31	27.72	19.98	1581
5H-6, 101–104	43.81	28.67	20.20	1617
6H-1, 101–104	45.81	28.89	20.53	1599
6H-2, 101–104	47.31	28.98	20.56	1601
6H-3, 101–104	48.81	28.91	20.59	1595
6H-4, 101–104	50.31	28.20	19.92	1616
6H-5, 101–104	51.81	29.50	20.89	1601
6H-6, 101–104	53.31	28.50	20.39	1589
7H-1, 101–104	55.31	29.07	20.56	1607
7H-2, 101–104	56.81	29.68	20.99	1602
7H-3, 101–104	58.31	29.20	20.58	1612
7H-4, 101–104	59.81	29.07	20.88	1577
7H-5, 101–104	61.31	28.85	20.53	1597
7H-6, 101–104	62.81	26.67	18.91	1622
8H-1, 101–104	64.81	28.59	20.26	1607
8H-2, 101–104	66.31	28.81	20.25	1621
8H-3, 101–104	67.81	29.15	20.67	1601
8H-4, 101–104	69.31	28.12	20.02	1601
8H-5, 101–104	70.81	27.97	20.01	1593
8H-6, 101–104	72.31	28.67	20.32	1606
9H-1, 101–104	74.31	29.50	20.59	1629
9H-2, 101–104	75.81	28.98	20.33	1623
9H-3, 101–104	77.31	28.37	19.89	1629
9H-4, 101–104	78.81	27.85	19.57	1629
9H-5, 91–94	80.21	29.41	20.75	1609
9H-6, 101–104	81.81	28.20	19.85	1623
10H-1, 50–53	83.3	29.24	20.36	1636
10H-2, 50–53	84.8	29.37	20.63	1618
10H-3, 50–53	86.3	29.51	20.80	1610
10H-4, 50–53	87.8	29.20	20.04	1665
10H-5, 50–53	89.3	29.59	20.37	1656
10H-6, 50–53	90.8	30.62	21.17	1640
11H-1, 90–93	93.2	29.42	20.49	1634
11H-2, 90–93	94.7	30.85	21.73	1602
11H-3, 90–93	96.2	30.24	21.11	1623
11H-4, 90–93	97.7	30.24	20.91	1642
11H-5, 90–93	99.2	30.02	23.99	1384
11H-6, 90–93	100.7	31.03	21.70	1615
12H-1, 80–83	102.6	30.86	21.55	1618
12H-2, 80–83	104.1	30.59	21.04	1650
12H-3, 80–83	105.6	29.15	20.27	1639
12H-4, 80–83	107.1	30.71	21.32	1631
12H-5, 80–83	108.6	29.51	20.33	1655
12H-6, 80–83	110.1	30.23	24.41	1366
13H-1, 90–93	112.2	31.28	20.94	1699
13H-2, 90–93	113.7	30.07	23.02	1456
13H-3, 90–93	115.2	30.59	20.94	1659
13H-4, 90–93	116.7	30.38	20.98	1643
13H-5, 90–93	118.2	30.98	21.41	1638

Table 11 (continued).

Core, section, interval (cm)	Depth (mbsf)	Distance (mm)	Traveltime (μs)	Velocity (m/s)
13H-6, 90–93	119.7	30.24	20.53	1678
14H-1, 80–83	121.6	30.91	24.30	1406
14H-2, 80–83	123.1	30.42	23.66	1427
14H-3, 80–83	124.6	30.53	20.92	1658
14H-4, 80–83	126.1	30.76	21.20	1645
14H-5, 80–83	127.6	30.24	23.74	1412
14H-6, 80–83	129.1	30.50	20.35	1711
15H-1, 80–83	131.1	30.11	20.74	1650
15H-2, 80–83	132.6	28.86	21.36	1523
15H-3, 80–83	134.1	29.23	19.97	1673
15H-4, 80–83	135.6	30.33	21.00	1639
15H-6, 80–83	138.6	30.50	20.42	1704
16H-1, 130–133	141.1	30.80	21.15	1652
16H-3, 130–133	144.1	28.91	19.77	1674
16H-5, 130–133	147.1	29.98	20.55	1661
17H-1, 130–133	150.6	30.59	20.81	1672
17H-3, 130–133	153.6	30.37	20.61	1678
17H-5, 130–133	156.6	29.77	20.23	1680
18H-1, 94–97	159.74	30.64	20.95	1661
18H-3, 94–97	162.74	29.94	19.76	1738
18H-5, 94–97	165.74	30.32	20.53	1683
19H-1, 50–53	168.8	30.11	20.51	1673
19H-3, 50–53	171.8	30.50	20.94	1654
19H-5, 50–53	174.8	29.84	20.28	1679
20H-1, 80–83	178.6	29.80	20.45	1660
20H-3, 80–83	181.6	30.02	20.28	1690
20H-5, 80–83	184.6	29.72	19.98	1702
21H-1, 80–83	188.1	29.81	20.17	1688
21H-3, 80–83	191.1	29.80	19.80	1726
21H-5, 80–83	194.1	29.33	19.50	1728
22H-1, 80–83	197.6	29.59	20.25	1667
22H-3, 80–83	200.6	29.34	19.90	1687
22H-5, 80–83	203.6	29.41	19.69	1713
22H-7, 11–14	205.91	28.73	19.58	1683
23H-1, 101–104	207.31	29.68	20.06	1692
23H-3, 101–104	210.31	28.50	19.22	1706
23H-5, 41–44	212.71	28.78	19.11	1736
24H-2, 101–104	218.31	29.50	19.93	1694
24H-5, 101–104	222.81	29.82	20.12	1694
26X-2, 101–104	228.31	29.55	20.14	1676
27X-2, 101–104	234.71	29.99	20.03	1713
27X-5, 91–94	239.11	20.42	16.19	1477
28X-2, 101–104	244.31	13.87	10.54	1708
29X-2, 18–21	253.18	45.91	31.34	1594
30X-5, 31–34	267.51	33.86	22.03	1740
32X-2, 69–72	282.69	17.97	12.42	1806
32X-5, 15–18	286.65	31.83	19.97	1831
33X-4, 66–69	295.36	23.03	15.40	1786
34X-2, 29–32	301.69	25.54	15.92	1911
35X-2, 120–123	312.3	28.41	18.70	1757
36X-2, 101–104	321.81	34.22	20.48	1918
36X-5, 62–65	325.92	35.57	24.24	1638
37X-2, 103–106	331.53	36.11	22.80	1788
38X-2, 52–55	340.72	76.48	47.32	1719
38X-6, 40–43	346.6	70.49	42.88	1760
39X-2, 62–65	350.52	49.40	30.00	1811
40X-3, 67–70	361.77	21.47	13.21	2012
41X-4, 54–57	372.95	24.31	14.89	1971
42X-4, 69–72	382.59	20.05	12.84	1942
43X-5, 72–75	393.82	24.00	14.26	2053
44X-1, 114–117	397.54	18.25	11.70	1984
47X-1, 70–72	426	36.94	19.83	2159

values. Again, this situation suggests that resistivity is increasing with distance away from the tool sondes because of the large diameter of the borehole. Thus, the deepest penetrating devices will provide the most reliable data when beds are thick, but all values are likely to be degraded in the presence of thin beds.

The situation in Zone 1 appears to fit the case above, where an SFL response of greater amplitude, both higher and lower than the other two, suggests the presence of very thin layers. This effect is highlighted in Figure 35, which is further described next.

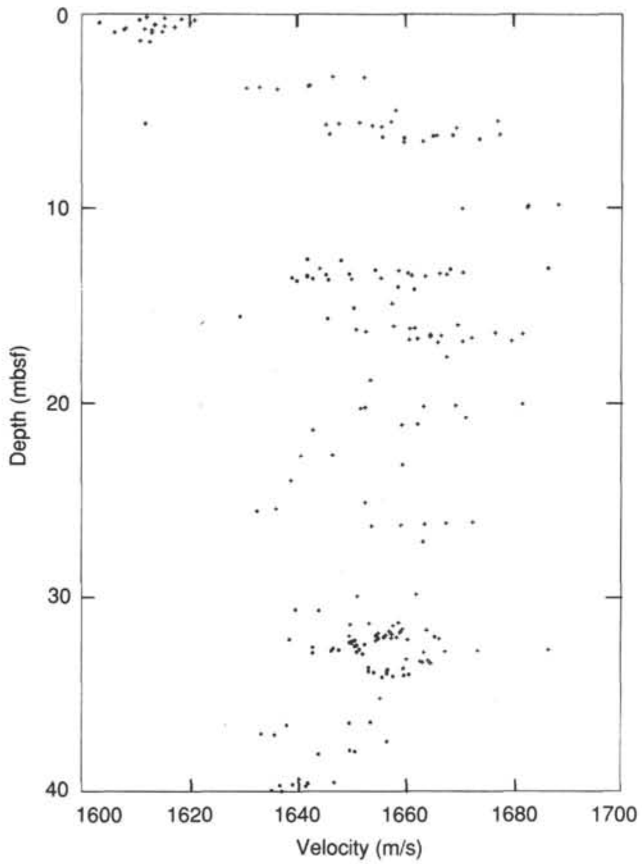

Figure 31. MST sonic velocity from Hole 815B (+) and upper 40 m of Hole 815A (*).

Cyclicity Within Logs

An expanded plot for resistivity, velocity, and gamma rays can be seen in Figure 37. The velocity log follows that of resistivity closely in character, suggesting that the cycles were controlled by porosity without cementation. These inferred porosity changes are similar in magnitude to those identified at Site 646 (Leg 105; Jarrard and Arthur, 1989). At Site 646, a change in sedimentation rate from 95 to 37 m/m.y. was accompanied by a major change in wavelength of the cycles; both these rates resulted in major spectral responses at the 95-k.y. Milankovitch period. Sedimentation rates at Site 815 may quadruple the higher rate described above and are 210 m in 0.730 m.y. (see "Biostratigraphy" section, this chapter).

The gamma-ray log does not exhibit the same close correlation with resistivity as the compressional wave velocity log. Some correlation in cyclicity can be seen at 210 mbsf, although the reverse was observed at 230 mbsf. This indicates that porosity is not controlled by clay, although some clay influence is likely.

The cyclic nature of the caliper and density logs suggests that this decrease in porosity was accompanied by a substantial loss in hole stability. The density log may read too low in these regions, as described in the preceding "Reliability of Logs" section (this chapter). The cyclicity in these logs probably has been controlled by sedimentary fabric and any associated changes in grain morphology. Changes in grain shape, distribution of grain sizes, and compaction all may be contributing factors that should be evaluated collectively.

Cyclicity was not identified in visual core descriptions, but shore-based analysis may detect these changes in porosity that were detected by downhole logging. The FMS is ideal for delineating details of resistivity changes, and we were extremely disappointed that it was not available for this site because of malfunctioning equipment. Far more structure may exist than is evident in the resistivity logs, as the highest resolution is approximately 1 m (SFL), and the character of the log is seen to average the response of thinner layers, for example in the section between 230 and 240 mbsf.

Resistivity-imaging of the core might detect these and even more subtle changes. A prototype core imager was evaluated during Leg 133 and yielded such information over limited sections of core. Section 133-815A-12H-6 was investigated between 38 and 68 cm, where imaging shows abrupt changes in resistivity of 12% over a few millimeters, although the section appears absolutely homogeneous to the naked eye. Thus, the potential exists for laboratory measurement of variations in porosity at a far higher resolution than has been possible to date.

Lithological and Petrophysical Interpretations

Further interpretation of resistivity is shown in Figure 35, where the electrical resistivity formation factor (FF) was plotted using spherically focused log and pore-water resistivities that decreased from 0.25 ohm-m (11.4°C) at the seafloor to 0.20 ohm-m (20°C) at 300 mbsf. Porosity values derived from the density log were used to calculate the component *m* in Archie's equation (1942):

$$FF = (porosity) \times (m), \quad (2)$$

which is probably the most applicable to the unlithified portion of the sediment column. The value of *m* has been shown to be controlled by particle shape for unconsolidated marine sands and clays, with pore spaces in turn being dependent on grain shapes. Thus, *m* may be a useful indicator of changes in lithology, where such changes are accompanied by a change in grain morphology. Some of the density values have been degraded by the large hole size, as this sonde requires contact with the borehole wall for accurate measurements. Values of *m* tend to accentuate these situations and provide an indicator of exactly which portions of the density log are unreliable.

As at Site 812 (see "Site 812" chapter, this volume), "mirror" anomalies are seen between "porosity" and Archie "*m*" logs in Figure 35, caused by the large hole diameter that degraded the density measurements. These anomalies can be identified in Figure 35 using an additional log, "Thin R," which was created especially for detecting the presence of thin resistive layers during Leg 133. This log measures the ratio of shallow, high-resolution SFL with deeper penetrating, but lower resolution, induction log. The computed log indicates an insensitivity to degradation in porosity because of hole enlargement. Velocity and resistivity ratios were measured to display differences between these two porosity logs, which are usually assumed to move together (Fig. 38). Here, positive values have formed when velocity is high and resistivity is low, as should be the case for a highly porous sediment in which grain contacts had been cemented. This appears to be the case for the interval below 415 to 425 mbsf. Positive peaks also can be generated if velocity remains constant and resistivity declines, as might happen should the grains of an unconsolidated sediment become more rounded at a constant porosity.

Log-Based Units

Lithologic Unit II (73.3–280.5 mbsf), a relatively uniform, high-porosity ooze, is seen in the logs to coincide approxi-

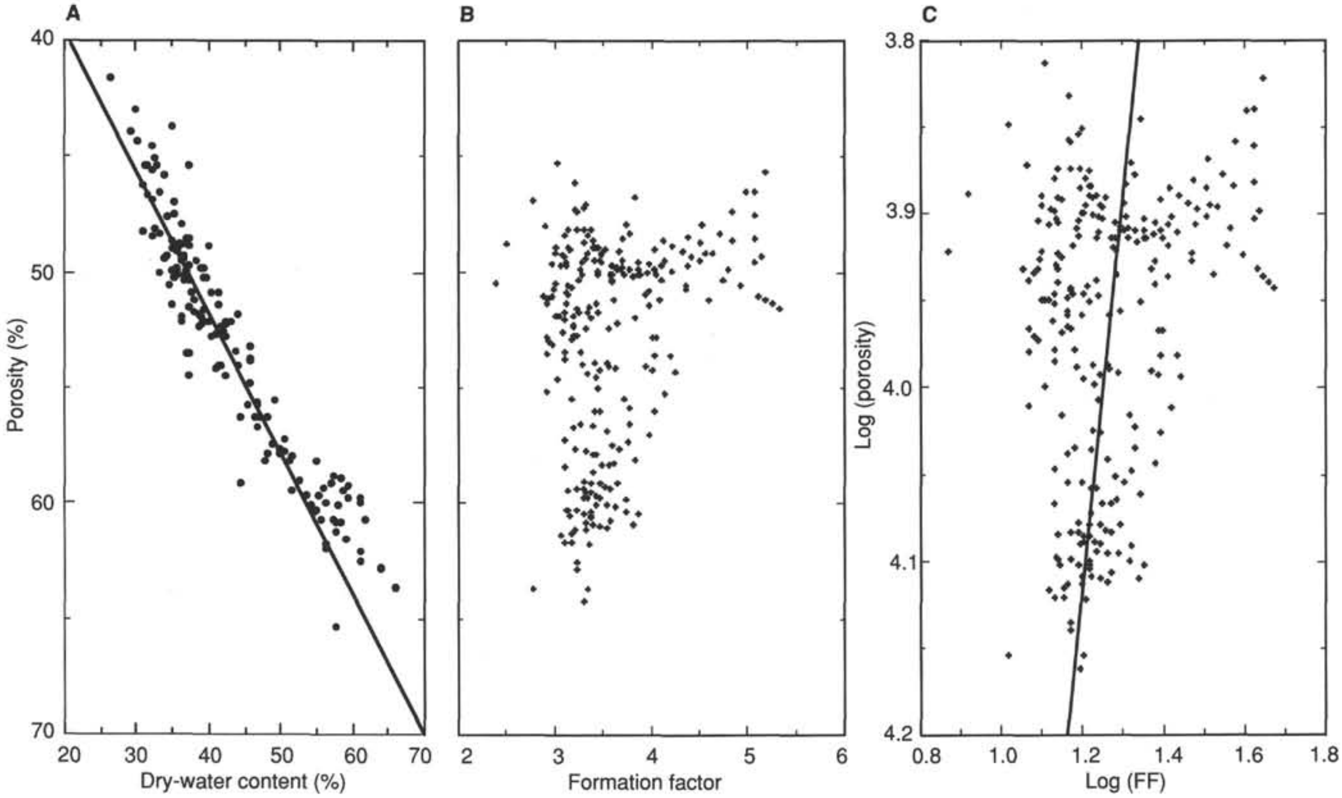

Figure 32. **A.** Dry-water content vs. porosity. Data were derived from mass and pycnometer volume measurements of discrete samples from cores. The linear least-squares regression line is $Y = -47.186 + 1.6997X$, where Y = dry-water content (%), X = porosity (%), and regression coefficient, $R = 0.948$. **B.** Electrical resistivity formation factor vs. porosity at Site 815. Porosity data were obtained from samples at locations in cores that were different from locations of resistivity measurements; thus, we linearly interpolated data values from Tables 10 and 12 to a table of porosity and resistivity at even 1-m spacing before plotting these values. **C.** Log (formation factor) vs. log (porosity) at Site 815. Linear fit to data is $Y = 2.99 - 0.436\ X$, where Y = log (formation factor), X = log (porosity), and regression coefficient, $R = 0.25$.

mately with resistivity Zone 1. Cyclicity within Unit II is evident in the logs and serves to delineate its lower extent. This cyclicity was described previously, and the response of the "Thin R" log (Fig. 35) is seen to delineate this zone of cyclicity, which suggests that thinner layers that are beyond the resolution of the tools deployed may be present.

The contact between Units II and III, at 271 mbsf in the logs and 280.5 mbsf in the cores, is seen as the termination of cyclicity and the beginning of constant values in the resistivity logs, particularly the "Thin R" log mentioned above. A thin bed having high velocity and resistivity at 295 mbsf has been identified by geochemical analyses as containing nearly 100% dolomite. A small increase in the general resistivity level at 355 mbsf coincides approximately with the boundary between Unit III (nannofossil chalk) and Unit IV (nannofossil foraminifer chalk; see "Lithostratigraphy" section, this chapter). We had observed slumping in Unit III, and Unit IV was seen to be sandier and compacted by bioturbation. Thus, Unit IV may be slightly more dense than Unit III, which explains the sedimentological description. Note that the Archie component, *m*, value did not change, indicating similar pore morphology (Fig. 35) in Units III and IV.

Log Unit IV extends to 408 mbsf, at which point resistivity and velocity increase substantially. This horizon is most evident in Figure 38, where ratios with seawater have been plotted. This lower-porosity, cemented zone extends to 415 mbsf. Lithologic Unit V has been described as extending to 444.5 mbsf (see "Lithostratigraphy" section, this chapter), just missing the high-porosity cemented zone between 415 and 425 mbsf, which has the high velocity/resistivity ratio seen in Figure 38. Such properties are consistent with dolomitization where grains have been partially dissolved and cemented, leading to divergence of the resistivity and velocity responses. Thus, Subunit VB may consist of dolomite between 415 and 425 mbsf, an interval of poor core recovery.

Underlying lithologic Unit VI may be similar to Subunit VA, although little log information was obtained from this lowest portion of the hole.

Temperature

Heat flow was not measured at Site 815; thus, the thermal gradient at the site is unknown. The L-DGO temperature tool was run at the bottom of the seismic stratigraphic and geochemical tool strings. Because hole temperatures were reduced by circulation during coring and by hole conditioning immediately prior to logging, we were unable to infer accurately an equilibrium thermal profile from two temperature logging runs. Our recorded maximum temperatures of 24.2° and 25.7°C near the bottom of the hole for these two logging runs thus is a minimum estimate of equilibrium temperature.

The temperature tool was run to determine whether fluid flow could be detected. In Figure 39, a plot measures temperature as a function of pressure, recorded simultaneously by the tool. Depths shown are approximate and may be revised by as much as 5 m during post-cruise merging of the Schlum-

Table 12. Electric resistance formation factor data for Hole 815A.

Core, section, interval (cm)	Depth (mbsf)	Seawater (ohms)	Sample (ohms)	Formation factor
133-815A-				
1H-1, 20–20	0.20	2.9	8.0	2.76
1H-1, 70–70	0.70	2.9	9.6	3.31
1H-1, 120–120	1.20	2.9	9.7	3.34
1H-2, 20–20	1.70	2.9	9.6	3.31
1H-2, 70–70	2.20	2.9	9.6	3.31
1H-2, 120–120	2.7	2.9	9.6	3.31
1H-3, 20–20	3.20	3.0	10.0	3.33
1H-3, 70–70	3.70	2.9	10.4	3.59
1H-3, 120–120	4.20	2.9	9.6	3.31
1H-4, 20–20	4.70	2.9	9.5	3.28
1H-4, 70–70	5.20	2.9	10.5	3.62
1H-4, 120–120	5.70	2.9	8.1	2.79
1H-5, 20–20	6.20	2.9	10.9	3.76
1H-5, 60–60	6.60	2.9	12.0	4.14
2H-1, 20–20	7.00	3.0	10.1	3.37
2H-1, 70–70	7.50	3.0	10.2	3.40
2H-1, 120–120	8.00	3.0	10.4	3.47
2H-2, 20–20	8.50	3.0	9.8	3.27
2H-2, 70–70	9.00	3.0	10.6	3.53
2H-2, 120–120	9.50	3.0	9.9	3.30
2H-3, 20–20	10.00	3.0	10.1	3.37
2H-3, 70–70	10.50	3.0	10.0	3.33
2H-3, 120–120	11.00	3.0	10.1	3.37
2H-4, 70–70	12.00	3.0	9.5	3.17
2H-4, 120–120	12.50	3.0	9.7	3.23
2H-5, 20–20	13.00	3.0	11.6	3.87
2H-5, 70–70	13.50	3.0	9.6	3.20
2H-5, 106–106	13.86	3.0	7.3	2.43
2H-5, 123–123	14.03	3.0	10.6	3.53
2H-6, 20–20	14.50	3.0	9.5	3.17
2H-6, 70–70	15.00	3.0	9.5	3.17
2H-6, 120–120	15.50	3.0	9.2	3.07
2H-7, 20–20	16.00	3.0	10.4	3.47
2H-7, 50–50	16.30	3.0	9.8	3.27
3H-1, 20–20	16.50	3.0	9.3	3.10
3H-1, 70–70	17.00	3.0	10.7	3.57
3H-1, 120–120	17.50	3.0	9.6	3.20
3H-2, 20–20	18.00	3.0	11.2	3.73
3H-2, 70–70	18.50	3.0	10.1	3.37
3H-2, 110–110	18.90	3.0	9.6	3.20
3H-3, 20–20	19.50	3.0	8.6	2.87
3H-3, 70–70	20.00	3.0	9.9	3.30
3H-3, 110–110	20.40	3.0	9.6	3.20
3H-4, 20–20	21.00	3.0	9.7	3.23
3H-4, 70–70	21.50	3.0	9.8	3.27
3H-4, 120–120	22.00	3.0	10.4	3.47
3H-5, 20–20	22.50	3.0	10.0	3.33
3H-5, 60–60	22.90	3.0	9.6	3.20
3H-5, 100–100	23.30	3.0	10.0	3.33
3H-6, 20–20	24.00	3.0	10.3	3.43
3H-6, 70–70	24.50	3.0	9.8	3.27
3H-6, 120–120	25.00	3.0	10.6	3.53
3H-7, 20–20	25.50	3.0	9.7	3.23
3H-7, 60–60	25.90	3.0	9.7	3.23
4H-1, 20–20	26.00	3.0	9.7	3.23
4H-1, 70–70	26.50	3.0	9.1	3.03
4H-1, 120–120	27.00	3.0	10.9	3.63
4H-2, 16–16	27.46	3.0	10.3	3.43
4H-2, 70–70	28.00	3.0	9.6	3.20
4H-2, 120–120	28.50	3.0	11.7	3.90
4H-3, 20–20	29.00	3.0	10.1	3.37
4H-3, 70–70	29.50	3.0	9.6	3.20
4H-3, 120–120	30.00	3.0	9.9	3.30
4H-4, 20–20	30.50	3.1	10.2	3.29
4H-4, 70–70	31.00	3.1	10.2	3.29
4H-4, 120–120	31.50	3.1	9.6	3.10
4H-5, 20–20	32.00	3.1	11.8	3.81
4H-5, 70–70	32.50	3.1	10.1	3.26
4H-5, 120–120	33.00	3.1	10.3	3.32
4H-6, 20–20	33.50	3.1	10.1	3.26
4H-6, 70–70	34.00	3.1	10.5	3.39
4H-6, 120–120	34.50	3.1	9.7	3.13
5H-1, 20–20	35.50	3.1	9.6	3.10
5H-1, 70–70	36.00	3.1	9.7	3.13

Table 12 (continued).

Core, section, interval (cm)	Depth (mbsf)	Seawater (ohms)	Sample (ohms)	Formation factor
5H-1, 120–120	36.50	3.1	10.2	3.29
5H-2, 20–20	37.00	3.1	10.2	3.29
5H-2, 70–70	37.50	3.1	10.1	3.26
5H-2, 120–120	38.00	3.1	10.9	3.52
5H-3, 20–20	38.50	3.1	10.6	3.42
5H-3, 70–70	39.00	3.1	10.4	3.35
5H-3, 120–120	39.50	3.1	10.0	3.23
5H-4, 20–20	40.00	3.1	9.5	3.06
5H-4, 70–70	40.50	3.1	10.6	3.42
5H-4, 120–120	41.00	3.1	9.7	3.13
5H-5, 20–20	41.50	3.1	9.6	3.10
5H-5, 70–70	42.00	3.1	9.6	3.10
5H-5, 120–120	42.50	3.1	9.5	3.06
5H-6, 20–20	43.00	3.1	10.0	3.23
5H-6, 70–70	43.50	3.1	10.4	3.35
5H-6, 120–120	44.00	3.1	9.6	3.10
6H-1, 20–20	45.00	3.1	10.2	3.29
6H-1, 70–70	45.50	3.1	9.9	3.19
6H-1, 120–120	46.00	3.1	11.6	3.74
6H-2, 20–20	46.50	3.1	10.0	3.23
6H-2, 70–70	47.00	3.1	11.2	3.61
6H-2, 120–120	47.50	3.1	11.3	3.65
6H-3, 20–20	48.00	3.1	10.5	3.39
6H-3, 70–70	48.50	3.1	11.8	3.81
6H-3, 120–120	49.00	3.1	10.3	3.32
6H-4, 20–20	49.50	2.8	10.0	3.57
6H-4, 70–70	50.00	2.8	9.7	3.46
6H-4, 120–120	50.50	2.8	10.4	3.71
6H-5, 20–20	51.00	2.8	10.5	3.75
6H-5, 60–60	51.40	2.8	10.6	3.79
6H-5, 120–120	51.80	2.8	9.7	3.46
6H-6, 20–20	52.50	2.8	10.7	3.82
6H-6, 70–70	53.00	2.8	10.2	3.64
6H-6, 120–120	53.50	2.8	10.4	3.71
7H-1, 20–20	54.50	2.9	9.9	3.41
7H-1, 70–70	55.00	2.9	10.4	3.59
7H-1, 120–120	55.50	2.9	10.8	3.72
7H-2, 20–20	56.00	2.9	10.0	3.45
7H-2, 70–70	56.50	2.9	10.4	3.59
7H-2, 120–120	57.00	2.9	11.1	3.83
7H-3, 20–20	57.50	2.9	10.1	3.48
7H-3, 70–70	58.00	2.9	10.3	3.55
7H-3, 120–120	58.50	2.9	11.1	3.83
7H-4, 20–20	59.00	2.9	9.9	3.41
7H-4, 70–70	59.50	2.9	10.5	3.62
7H-4, 120–120	60.00	2.9	10.8	3.72
7H-5, 20–20	60.50	2.9	10.7	3.69
7H-5, 70–70	61.00	2.9	10.0	3.45
7H-5, 120–120	61.50	2.9	10.8	3.72
7H-6, 20–20	62.00	2.9	12.3	4.24
7H-6, 70–70	62.50	2.9	11.7	4.03
7H-6, 120–120	63.00	2.9	11.4	3.93
8H-1, 20–20	64.00	2.9	11.7	4.03
8H-1, 70–70	64.50	2.9	11.2	3.86
8H-1, 120–120	65.00	3.0	11.0	3.67
8H-2, 20–20	65.50	2.9	12.0	4.14
8H-2, 70–70	66.00	2.9	11.1	3.83
8H-2, 120–120	66.50	2.9	12.0	4.14
8H-3, 20–20	67.00	2.9	11.5	3.97
8H-3, 70–70	67.50	2.9	11.2	3.86
8H-3, 120–120	68.00	2.9	12.0	4.14
8H-4, 20–20	68.50	3.0	10.9	3.63
8H-4, 70–70	69.00	3.0	12.0	4.00
8H-4, 120–120	69.50	3.0	11.1	3.70
8H-5, 20–20	70.00	3.0	10.4	3.47
8H-5, 70–70	70.50	3.0	10.0	3.33
8H-5, 120–120	71.00	3.0	10.6	3.53
8H-6, 20–20	71.50	3.0	9.2	3.07
8H-6, 70–70	72.00	3.0	10.3	3.43
8H-6, 120–120	72.50	3.0	10.3	3.43
9H-1, 20–20	73.50	3.0	12.4	4.13
9H-1, 70–70	74.00	3.0	10.9	3.63
9H-1, 120–120	74.50	3.0	10.7	3.57
9H-2, 20–20	75.00	3.0	12.1	4.03
9H-2, 70–70	75.50	3.0	10.8	3.60
9H-2, 120–120	76.00	3.0	10.6	3.53
9H-3, 20–20	76.50	3.0	9.8	3.27

Table 12 (continued).

Core, section, interval (cm)	Depth (mbsf)	Seawater (ohms)	Sample (ohms)	Formation factor
9H-3, 70–70	77.00	3.0	10.0	3.33
9H-3, 120–120	77.50	3.0	10.2	3.40
9H-4, 20–20	78.00	3.0	10.2	3.40
9H-4, 70–70	78.50	3.0	9.9	3.30
9H-4, 120–120	79.00	3.0	12.6	4.20
9H-5, 20–20	79.50	3.0	10.9	3.63
9H-5, 90–90	80.20	3.0	11.5	3.83
9H-6, 20–20	81.00	2.8	11.2	4.00
9H-6, 70–70	81.50	2.8	13.5	4.82
9H-6, 120–120	82.00	2.8	11.3	4.04
10H-1, 20–20	83.00	3.2	10.2	3.19
10H-1, 70–70	83.50	2.9	9.8	3.38
10H-1, 120–120	84.00	3.0	9.6	3.20
10H-2, 20–20	84.50	3.1	8.9	2.87
10H-2, 70–70	85.00	3.1	9.6	3.10
10H-2, 120–120	85.50	3.0	10.5	3.50
10H-3, 20–20	86.00	3.1	10.1	3.26
10H-3, 70–70	86.50	3.1	11.0	3.55
10H-3, 120–120	87.00	3.1	10.1	3.26
10H-4, 20–20	87.50	3.1	9.6	3.10
10H-4, 70–70	88.00	3.2	9.6	3.00
10H-4, 120–120	88.50	3.0	9.5	3.17
10H-5, 20–20	89.00	3.1	9.9	3.19
10H-5, 70–70	89.50	3.1	9.8	3.16
10H-5, 120–120	90.00	3.1	9.8	3.16
10H-6, 20–20	90.50	3.1	10.2	3.29
10H-6, 70–70	91.00	3.1	10.5	3.39
10H-6, 120–120	91.50	3.0	10.9	3.63
11H-1, 20–20	92.50	3.1	9.8	3.16
11H-1, 70–70	93.00	3.1	10.6	3.42
11H-1, 120–120	93.50	3.0	10.2	3.40
11H-2, 20–20	94.00	3.2	10.1	3.16
11H-2, 70–70	94.50	3.2	9.6	3.00
11H-2, 120–120	95.00	3.2	10.2	3.19
11H-3, 20–20	95.50	3.1	10.0	3.23
11H-3, 70–70	96.00	3.1	9.6	3.10
11H-3, 120–120	96.50	3.1	9.8	3.16
11H-4, 20–20	97.00	3.1	9.6	3.10
11H-4, 70–70	97.50	3.1	9.9	3.19
11H-4, 120–120	98.00	3.1	10.0	3.23
11H-5, 20–20	98.50	3.1	10.0	3.23
11H-5, 70–70	99.00	3.2	10.2	3.19
11H-5, 120–120	99.50	3.2	10.0	3.13
11H-6, 20–20	100.00	3.2	9.9	3.09
11H-6, 70–70	100.50	3.2	9.8	3.06
11H-6, 120–120	101.00	3.0	10.0	3.33
12H-1, 20–20	102.00	3.2	9.7	3.03
12H-1, 70–70	102.50	3.1	10.5	3.39
12H-1, 120–120	103.00	3.3	9.6	2.91
12H-2, 20–20	103.50	3.0	10.3	3.43
12H-2, 70–70	104.00	3.2	10.2	3.19
12H-2, 120–120	104.50	3.2	10.1	3.16
12H-3, 20–20	105.00	3.1	10.3	3.32
12H-3, 70–70	105.50	3.1	10.4	3.35
12H-3, 120–120	106.00	3.0	9.7	3.23
12H-4, 20–20	106.50	3.1	9.8	3.16
12H-4, 70–70	107.00	3.2	9.6	3.00
12H-4, 120–120	107.50	3.2	10.2	3.19
12H-5, 20–20	108.00	3.1	9.6	3.10
12H-5, 70–70	108.50	3.1	9.9	3.19
12H-5, 120–120	109.00	3.4	10.1	2.97
12H-6, 20–20	109.50	3.2	10.1	3.16
12H-6, 70–70	110.00	3.2	10.1	3.16
12H-6, 120–120	110.50	3.1	10.1	3.26
13H-1, 20–20	111.50	3.3	10.9	3.30
13H-1, 70–70	112.00	3.3	10.9	3.30
13H-1, 120–120	112.50	3.3	10.9	3.30
13H-2, 20–20	113.00	3.4	11.3	3.32
13H-2, 70–70	113.50	3.5	10.1	2.89
13H-2, 120–120	114.00	3.5	9.7	2.77
13H-4, 20–20	116.00	3.3	10.6	3.21
13H-4, 70–70	116.50	3.3	9.6	2.91
13H-4, 120–120	117.00	3.2	9.7	3.03
13H-6, 20–20	119.00	3.2	10.3	3.22
13H-6, 70–70	119.50	3.3	10.5	3.18
13H-6, 120–120	120.00	3.3	10.6	3.21
14H-1, 20–20	121.00	3.4	10.6	3.12

Table 12 (continued).

Core, section, interval (cm)	Depth (mbsf)	Seawater (ohms)	Sample (ohms)	Formation factor
14H-1, 70–70	121.50	3.3	9.7	2.94
14H-1, 120–120	122.00	3.0	10.3	3.43
14H-3, 20–20	124.00	3.1	10.7	3.45
14H-3, 70–70	124.50	3.4	12.8	3.76
14H-3, 120–120	125.00	3.2	9.8	3.06
14H-5, 20–20	127.00	3.2	10.0	3.13
14H-5, 70–70	127.50	3.3	10.5	3.18
14H-5, 120–120	128.00	3.4	10.6	3.12
14H-6, 20–20	128.50	3.3	11.8	3.58
14H-6, 70–70	129.00	3.6	11.2	3.11
14H-6, 120–120	129.50	3.3	11.0	3.33
15H-1, 20–20	130.50	3.3	10.3	3.12
15H-1, 70–70	131.00	3.3	10.8	3.27
15H-1, 120–120	131.50	3.2	10.9	3.41
15H-3, 20–20	133.50	3.3	10.0	3.03
15H-3, 70–70	134.00	3.3	9.7	2.94
15H-3, 120–120	134.50	3.3	9.6	2.91
15H-5, 20–20	136.50	3.3	9.6	2.91
15H-5, 70–70	137.00	3.2	9.5	2.97
15H-5, 120–120	137.50	3.2	9.8	3.06
16H-1, 20–20	140.00	3.2	10.0	3.13
16H-1, 70–70	140.50	2.9	9.9	3.41
16H-1, 120–120	141.00	3.0	10.2	3.40
16H-3, 20–20	143.00	2.7	10.2	3.78
16H-3, 70–70	143.50	3.1	10.3	3.32
16H-3, 120–120	144.00	2.8	10.0	3.57
16H-5, 20–20	146.00	2.8	10.8	3.86
16H-5, 70–70	146.50	3.2	11.3	3.53
16H-5, 120–120	147.00	2.8	11.3	4.04
16H-7, 20–20	148.90	3.0	10.2	3.40
16H-7, 70–70	149.40	3.3	12.1	3.67
17H-2, 20–20	151.00	3.3	10.4	3.15
17H-2, 70–70	151.50	3.4	10.2	3.00
17H-2, 120–120	152.00	3.0	10.2	3.40
17H-4, 20–20	154.00	3.3	11.5	3.48
17H-4, 70–70	154.50	3.1	11.2	3.61
17H-4, 120–120	155.00	3.2	10.5	3.28
17H-6, 20–20	157.00	3.4	10.0	2.94
17H-6, 70–70	157.50	3.1	9.7	3.13
18H-1, 20–20	159.00	3.1	10.8	3.48
18H-1, 70–70	159.50	3.3	10.1	3.06
18H-1, 120–120	160.00	3.3	9.9	3.00
18H-3, 20–20	162.00	3.2	12.1	3.78
18H-3, 70–70	162.50	3.4	12.0	3.53
18H-3, 120–120	163.00	3.3	10.9	3.30
18H-5, 20–20	165.00	3.2	10.8	3.38
18H-5, 70–70	165.50	3.2	10.1	3.16
18H-5, 120–120	166.00	3.2	10.8	3.38
19H-1, 20–20	168.50	3.3	10.7	3.24
19H-1, 70–70	169.00	3.3	11.8	3.58
19H-1, 120–120	169.50	3.3	12.3	3.73
19H-3, 20–20	171.50	3.4	11.1	3.26
19H-3, 70–70	172.00	3.6	11.1	3.08
19H-3, 120–120	172.50	3.4	11.9	3.50
19H-5, 20–20	174.50	2.9	10.7	3.69
19H-5, 70–70	175.00	2.9	11.1	3.83
19H-5, 120–120	175.50	3.0	10.8	3.60
20H-1, 20–20	178.00	3.2	7.6	2.38
20H-1, 70–70	178.50	3.2	10.0	3.13
20H-1, 120–120	179.00	2.9	10.4	3.59
20H-3, 20–20	181.00	3.2	11.8	3.69
20H-3, 70–70	181.50	3.1	11.1	3.58
20H-3, 120–120	182.00	3.1	10.9	3.52
20H-5, 20–20	184.00	3.1	10.0	3.23
20H-5, 70–70	184.50	3.2	10.3	3.22
20H-5, 120–120	185.00	3.1	10.2	3.29
21H-1, 20–20	187.50	3.0	6.9	2.30
21H-1, 70–70	188.00	3.3	9.8	2.97
21H-1, 120–120	188.50	3.2	10.1	3.16
21H-3, 20–20	190.50	3.1	12.0	3.87
21H-3, 70–70	191.00	3.1	11.6	3.74
21H-3, 120–120	191.50	3.1	11.5	3.71
21H-5, 20–20	193.50	3.3	11.7	3.55
21H-5, 70–70	194.00	3.3	10.7	3.24
21H-5, 120–120	194.50	3.4	10.4	3.06
22H-1, 20–20	197.00	3.3	9.9	3.00
22H-1, 70–70	197.50	3.3	10.1	3.06

Table 12 (continued).

Core, section, interval (cm)	Depth (mbsf)	Seawater (ohms)	Sample (ohms)	Formation factor
22H-1, 120–120	198.00	3.4	9.9	2.91
22H-3, 20–20	200.00	2.7	11.8	4.37
22H-3, 70–70	200.50	2.7	12.2	4.52
22H-3, 120–120	201.00	2.7	12.2	4.52
22H-5, 20–20	203.00	2.7	13.9	5.15
22H-5, 70–70	203.50	2.7	14.5	5.37
22H-5, 130–130	204.10	2.7	12.6	4.67
22H-7, 20–20	206.00	2.8	10.3	3.68
22H-7, 50–50	206.30	2.8	11.8	4.21
23H-1, 20–20	206.40	2.8	9.7	3.46
23H-1, 70–70	207.00	2.8	12.6	4.50
23H-1, 120–120	207.50	2.9	12.9	4.45
23H-3, 20–20	209.50	2.9	13.6	4.69
23H-3, 70–70	210.00	2.9	12.7	4.38
23H-3, 120–120	210.50	2.9	11.0	3.79
23H-5, 20–20	212.50	2.9	11.9	4.10
23H-5, 50–50	212.80	2.9	11.9	4.10
24H-2, 20–20	217.50	2.9	13.2	4.55
24H-2, 50–50	217.80	2.9	12.8	4.41
24H-2, 70–70	218.00	3.0	12.3	4.10
24H-5, 20–20	222.00	3.0	11.4	3.80
24H-5, 50–50	222.30	2.9	13.3	4.59
24H-5, 70–70	222.50	2.9	14.3	4.93
25H-1, 5–5	225.35	2.9	11.1	3.83
26X-2, 20–20	227.50	2.9	12.1	4.17
26X-2, 70–70	228.00	2.9	11.5	3.97
26X-2, 120–120	228.50	2.9	13.7	4.72
26X-5, 20–20	232.00	2.9	11.2	3.86
26X-5, 50–50	232.30	2.9	11.3	3.90
27X-2, 20–20	233.90	2.9	11.8	4.07
27X-2, 70–70	234.40	2.8	12.4	4.43
27X-2, 120–120	234.90	2.8	12.7	4.54
27X-5, 20–20	238.40	2.8	14.1	5.04
27X-5, 70–70	238.90	2.8	14.6	5.21
27X-5, 120–120	239.40	2.8	14.2	5.07
28X-2, 20–20	243.50	2.8	14.2	5.07
28X-2, 70–70	244.00	2.8	13.8	4.93
28X-2, 120–120	244.50	2.8	14.2	5.07
28X-5, 20–20	248.00	2.8	14.9	5.32
28X-5, 70–70	248.50	2.8	14.3	5.11
28X-5, 110–110	248.90	2.8	12.3	4.39

berger time/depth data with L-DGO temperature-tool time/pressure data.

The temperature pattern shown in Figure 39 indicates approximately constant temperature for the bottom 75 m, which decreases nearly linearly from 400 to 0 mbsf and declines sharply at the seafloor, to bottom-water temperatures of 10° to 12°C. One possible explanation for these observations is that water is flowing up out of the bottom 75 m of the formation. Most of this outflow presumably would be to the seafloor. An alternative explanation is that no fluid flow has an effect on borehole temperatures, but rather that annual variations in bottom-water temperature are so large that the formation is not in thermal equilibrium with the bottom waters.

SEISMIC STRATIGRAPHY

We divided the stratigraphic section at Site 815 into 13 seismic sequences, of which 12 were drilled (Figs. 40 and 41). Each of these sequences is described briefly next and in the following section, they are correlated with the lithology encountered at this site.

The top 10 sequences are conformable and have similar seismic character. The unconformities that define these sequences have been restricted to an area adjacent to the carbonate platform south of the site. The depth below seafloor for each sequence was determined using the sonic log and integrated two-way traveltime plot shown in Figure 36. These sequences are depicted in Figures 40 and 41.

Sequence 1 extends from the seafloor down approximately 0.07 s to 0.690 s at Site 815 (0–70 mbsf). Much of the character of this sequence has been obscured by a strong source pulse signature. Where seismic character can be identified, it appears to consist of continuous reflectors of moderate amplitude and frequency.

Sequence 2 occurs between 0.690 and 0.715 s (70–80 mbsf) at Site 815, where it consists of parallel, continuous reflectors of low-to-moderate amplitude and moderate frequency. Farther south, between common depth points 1300 and 1400, this sequence consists of a series of relatively steeply dipping clinoforms that downlap onto a composite unconformity comprising the sequence boundary for the next eight sequences.

Sequence 3 occurs between 0.715 and 0.745 s (80–104 mbsf) at Site 815, where it consists of a discontinuous low-amplitude and moderate frequency reflector. To the south, the sequence thickens into a series of clinoforms. These clinoforms onlap the top of sequence 4, whereas the bottom of the clinoforms downlap onto the composite unconformity referred to above.

Sequence 4 occurs between 0.745 and 0.760 s (104–115 mbsf), where it consists of moderate amplitude and frequency reflectors that form low-angle clinoforms to the south, adjacent to a carbonate platform. These clinoforms onlap the top of sequence 5.

Sequence 5 occurs between 0.760 and 0.780 s (115–137 mbsf), where it consists of parallel continuous to discontinuous reflectors of moderate amplitude and frequency. To the south, the sequence forms very broad, low-angle clinoforms that downlap onto the top of sequence 6.

Sequence 6 occurs between 0.780 and 0.795 s (137–148 mbsf), where it consists of parallel continuous reflectors of moderate amplitude and frequency at the site.

Sequence 7 occurs between 0.795 and 0.808 s (148–160 mbsf), where it consists of parallel continuous reflectors of moderate amplitude and frequency.

Sequence 8 occurs between 0.808 and .830 s (160–180 mbsf). At the site, this sequence consists of a low-amplitude, moderate frequency reflector. To the south, this reflector passes into a channel fill that consists of high-amplitude, moderate- to low-frequency reflectors.

Sequence 9 occurs between 0.830 and 0.885 s (180–232 mbsf), where it consists of parallel discontinuous reflectors of moderate-to-high amplitude and moderate frequency that downlap the top of sequences 10 and 11, adjacent to a carbonate platform to the south.

Sequence 10 occurs between 0.885 and 0.970 s (232–314 mbsf). The sequence consists of parallel continuous to discontinuous reflectors of moderate- to low-amplitude and moderate frequency that onlap sequence 11.

Sequence 11 occurs between 0.970 and 1.030 s (314–375 mbsf). It consists of discontinuous, hummocky reflectors of moderate amplitude and frequency. Its upper surface is an erosional unconformity. Sequence 11 onlaps sequence 12.

Sequence 12 occurs between 1.030 and 1.085 s (375–440 mbsf) and consists of parallel reflectors of moderate amplitude and frequency that onlap sequence 13.

Sequence 13 occurs between 1.085 and 1.170 s (440–(?) mbsf) and consists of discontinuous hummocky reflectors of moderate amplitude and frequency. To the south, sequence 13 thickens and forms the carbonate platform that was drilled at Sites 816 and 826. The sequence stratigraphy of this platform is described in the appropriate sections of the chapters for these sites.

Correlation With Lithology of Site 815

Sequence 1 corresponds to lithologic Unit 1 (see Fig. 40 for correlation between seismic stratigraphy and lithostratigra-

Table 13. Vane shear strength data from Hole 815A.

Core, section, interval (cm)	Depth (mbsf)	Spring number	Torque (degrees)	Strain (degrees)	Shear strength (kPa)
133-815A-					
1H-1, 91–92	0.91	1	18	20	3.8
1H-2, 91–92	2.41	1	19	20	4.0
1H-3, 91–92	3.91	1	61	22	12.9
1H-4, 91–92	5.41	1	53	19	11.2
1H-5, 31–32	6.31	1	64	23	13.6
2H-1, 91–92	7.71	1	38	28	8.1
2H-2, 91–92	9.21	1	81	20	17.2
2H-3, 91–92	10.71	1	33	25	7.0
2H-4, 91–92	12.21	1	51	24	10.8
2H-5, 91–92	13.71	1	57	22	12.1
2H-6, 91–92	15.21	1	58	23	12.3
3H-1, 91–92	17.21	1	59	24	12.5
3H-2, 91–92	18.71	1	52	22	11.0
3H-3, 91–92	20.21	1	35	21	7.4
3H-4, 91–92	21.71	1	29	20	6.2
3H-5, 71–72	23.01	1	56	22	11.9
3H-6, 91–92	24.71	1	55	20	11.7
4H-1, 102–103	26.82	1	31	26	6.6
4H-2, 91–92	28.21	1	48	24	10.2
4H-3, 91–92	29.71	1	87	25	18.5
4H-4, 91–92	31.21	1	50	23	10.6
4H-5, 91–92	32.71	1	82	21	17.4
4H-6, 91–92	34.21	1	112	19	23.8
5H-1, 91–92	36.21	1	45	25	9.5
5H-2, 91–92	37.71	1	37	26	7.9
5H-3, 91–92	39.21	1	57	20	12.1
5H-4, 91–92	40.71	1	61	23	12.9
5H-5, 91–92	42.21	1	34	26	7.2
5H-6, 91–92	43.71	1	65	22	13.8
6H-1, 91–92	45.71	1	69	25	14.6
6H-2, 91–92	47.21	1	93	25	19.7
6H-3, 91–92	48.71	1	70	25	14.9
6H-4, 91–92	50.21	1	58	25	12.3
6H-5, 91–92	51.71	1	89	23	18.9
6H-6, 91–92	53.21	1	68	25	14.4
7H-1, 91–92	55.21	1	54	23	11.5
7H-2, 91–92	56.71	1	125	23	26.5
7H-3, 91–92	58.21	1	64	23	13.6
7H-4, 91–92	59.71	1	83	23	17.6
7H-5, 91–92	61.21	1	76	22	16.1
7H-6, 91–92	62.71	1	104	25	22.1
8H-1, 91–92	64.71	1	75	22	15.9
8H-2, 91–92	66.21	1	134	25	28.4
8H-3, 91–92	67.71	1	101	25	21.4
8H-4, 91–92	69.21	1	115	25	24.4
8H-5, 91–92	70.71	1	68	21	14.4
8H-6, 55–56	71.85	1	75	23	15.9
8H-6, 91–92	72.21	1	62	23	13.2
9H-1, 90–91	74.20	1	113	25	24.0
9H-2, 90–91	75.70	1	88	25	18.7
9H-3, 90–91	77.20	1	90	25	19.1
9H-4, 90–91	78.70	1	167	24	35.4
9H-5, 69–70	79.99	2	42	23	19.8
9H-6, 90–91	81.70	2	136	18	64.0
10H-1, 90–91	83.70	2	49	21	23.1
10H-2, 90–91	85.20	2	67	19	31.5
10H-3, 90–91	86.70	2	41	20	19.3
10H-4, 90–91	88.20	2	50	24	23.5
10H-5, 90–91	89.70	2	68	22	32.0
10H-6, 95–96	91.25	2	67	23	31.5
11H-1, 95–96	93.25	2	39	18	18.4
11H-2, 95–96	94.75	2	97	20	45.6
11H-3, 95–96	96.25	2	65	19	30.6
11H-4, 95–96	97.75	2	83	20	39.1
11H-5, 95–96	99.25	2	69	16	32.5
11H-6, 95–96	100.75	2	55	18	25.9
12H-1, 95–96	102.75	2	71	18	33.4
12H-2, 95–96	104.25	2	40	14	18.8
12H-3, 95–96	105.75	2	42	18	19.8
12H-4, 95–96	107.25	2	56	16	26.3
12H-5, 95–96	108.75	2	95	23	44.7
12H-6, 102–103	110.32	2	93	17	43.8
13H-1, 102–103	112.32	2	141	19	66.3
13H-2, 102–103	113.82	2	62	19	29.2
13H-4, 102–103	116.82	2	32	16	15.1
13H-6, 102–103	119.82	2	138	16	64.9

Table 13 (continued).

Core, section, interval (cm)	Depth (mbsf)	Spring number	Torque (degrees)	Strain (degrees)	Shear strength (kPa)
14H-1, 102–103	121.82	2	94	16	44.2
14H-3, 102–103	124.82	2	83	23	39.1
14H-5, 102–103	127.82	2	111	21	52.2
14H-6, 102–103	129.32	2	295	24	138.8
15H-1, 102–103	131.32	2	276	19	129.9
15H-3, 102–103	134.32	2	126	17	59.3
15H-5, 102–103	137.32	2	93	13	43.8
16H-1, 102–103	140.82	2	156	16	73.4
16H-3, 102–103	143.82	2	120	21	56.5
16H-5, 102–103	146.82	2	304	26	143.0
16H-7, 77–78	149.47	2	232	24	109.2
17H-2, 89–90	151.69	2	206	15	96.9
17H-4, 89–90	154.69	2	344	11	161.9
17H-6, 82–83	157.62	2	206	24	96.9
18H-1, 90–91	159.70	2	115	14	54.1
18H-3, 90–91	162.70	2	244	30	114.8
18H-5, 90–91	165.70	2	186	11	87.5
19H-1, 90–91	169.20	2	291	28	136.9
19H-3, 90–91	172.20	2	343	23	161.4
19H-5, 90–91	175.20	2	437	16	205.6
20H-1, 91–92	178.71	2	432	17	203.3
20H-3, 91–92	181.71	2	265	26	124.7
20H-5, 95–96	184.75	2	119	20	56.0
21H-1, 95–96	188.25	2	127	14	59.8
21H-1, 101–102	188.31	2	93	19	43.8
21H-3, 101–102	191.31	2	379	22	178.3
21H-5, 101–102	194.31	2	392	23	184.4
22H-1, 101–102	197.81	2	157	17	73.9
22H-3, 101–102	200.81	4	93	18	110.6
22H-5, 95–96	203.75	4	180	17	214.1
22H-7, 40–41	206.20	4	47	19	55.9
23H-1, 90–91	207.20	4	187	20	222.4
23H-3, 90–91	210.20	4	120	20	142.7
23H-5, 30–31	212.60	4	222	24	264.0
24H-2, 90–91	218.20	4	135	22	160.6
24H-5, 90–91	222.70	4	153	21	182.0
26X-2, 90–91	228.20	4	141	23	167.7
26X-5, 30–31	232.10	4	73	23	86.8
27X-2, 91–92	234.61	4	121	20	143.9
27X-5, 99–100	239.19	4	145	17	172.4

phy) and thus consists of white to pale brown to gray foraminifer nannofossil to nannofossil foraminifer ooze.

Sequences 2 through 10 correlate with lithologic Unit II, which consists of greenish-gray to gray homogeneous to slightly bioturbated nannofossil ooze to unlithified nannofossil mixed sediment. Considerable variation exists in the carbonate content of these sediments (see Fig. 25, "Inorganic Geochemistry" section, this chapter). The top half of sequence 10 corresponds to the base of lithologic Unit II.

The lower half of sequence 10 and the upper part of sequence 11 correlate with Unit III, which was divided into two subunits. Subunit IIIA corresponds to the basal half of sequence 10 and consists of greenish-gray to gray foraminifer nannofossil and nannofossil foraminifer chalks.

The top of sequence 11 correlates with the top of Subunit IIIB and consists of lithified mixed sediments with intervals of contorted and convoluted bedding that were interpreted as slump features. The base of sequence 11 and the upper two-thirds of sequence 12 correspond to Unit IV, which consists of greenish-gray to gray foraminifer nannofossil and nannofossil foraminifer chalk.

The lower part of sequence 12 corresponds to Unit V, which consists of pale brown calcareous to dolomitized lithified foraminifer packstone and minor chalk.

Only the upper part of sequence 13 was cored. Recovery was poor. The sediments recovered consisted of the dolomi-

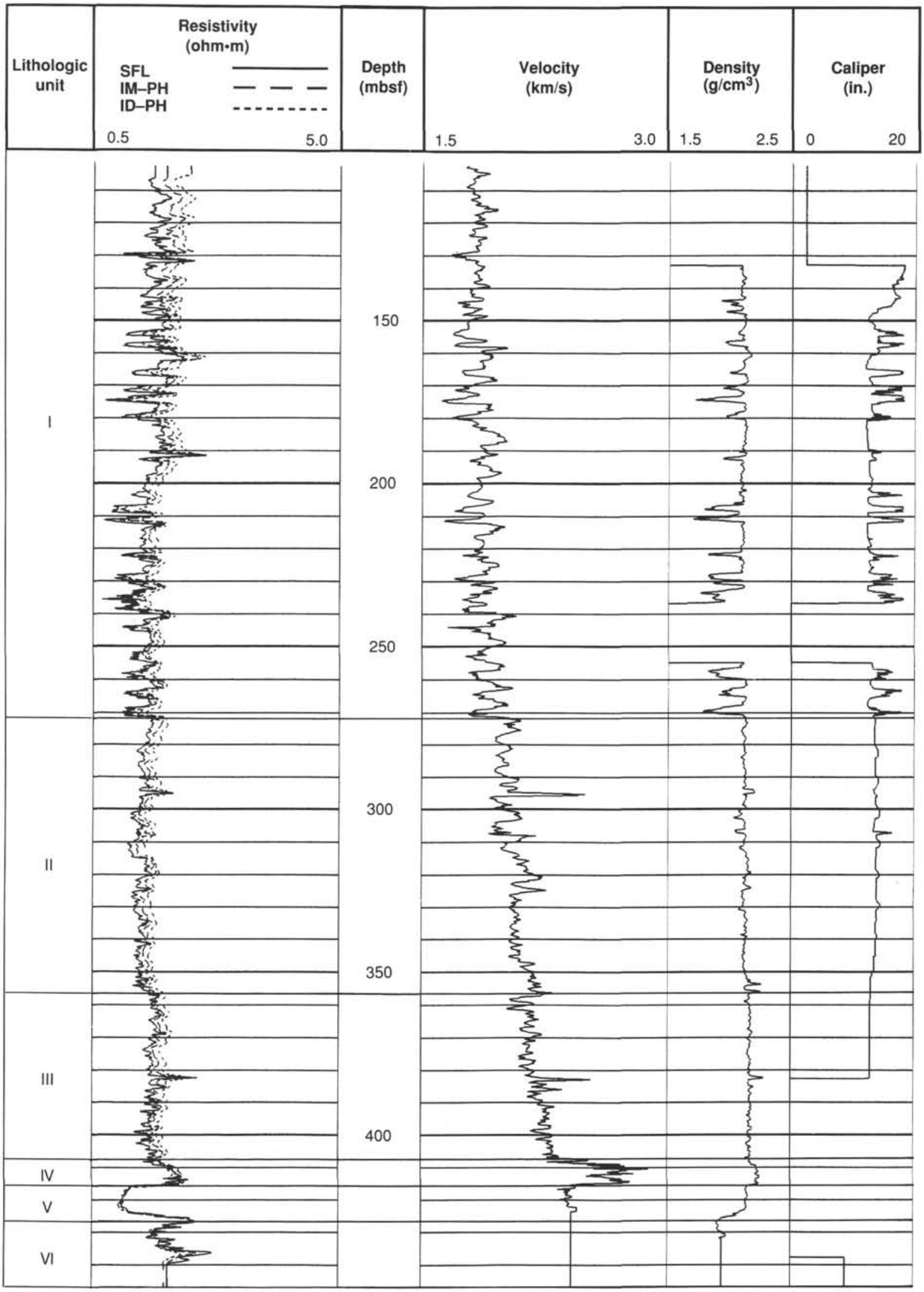

Figure 33. Primary porosity logs obtained with seismic stratigraphic string at Site 815 and used for differentiating lithologies, showing six resistivity-based zones.

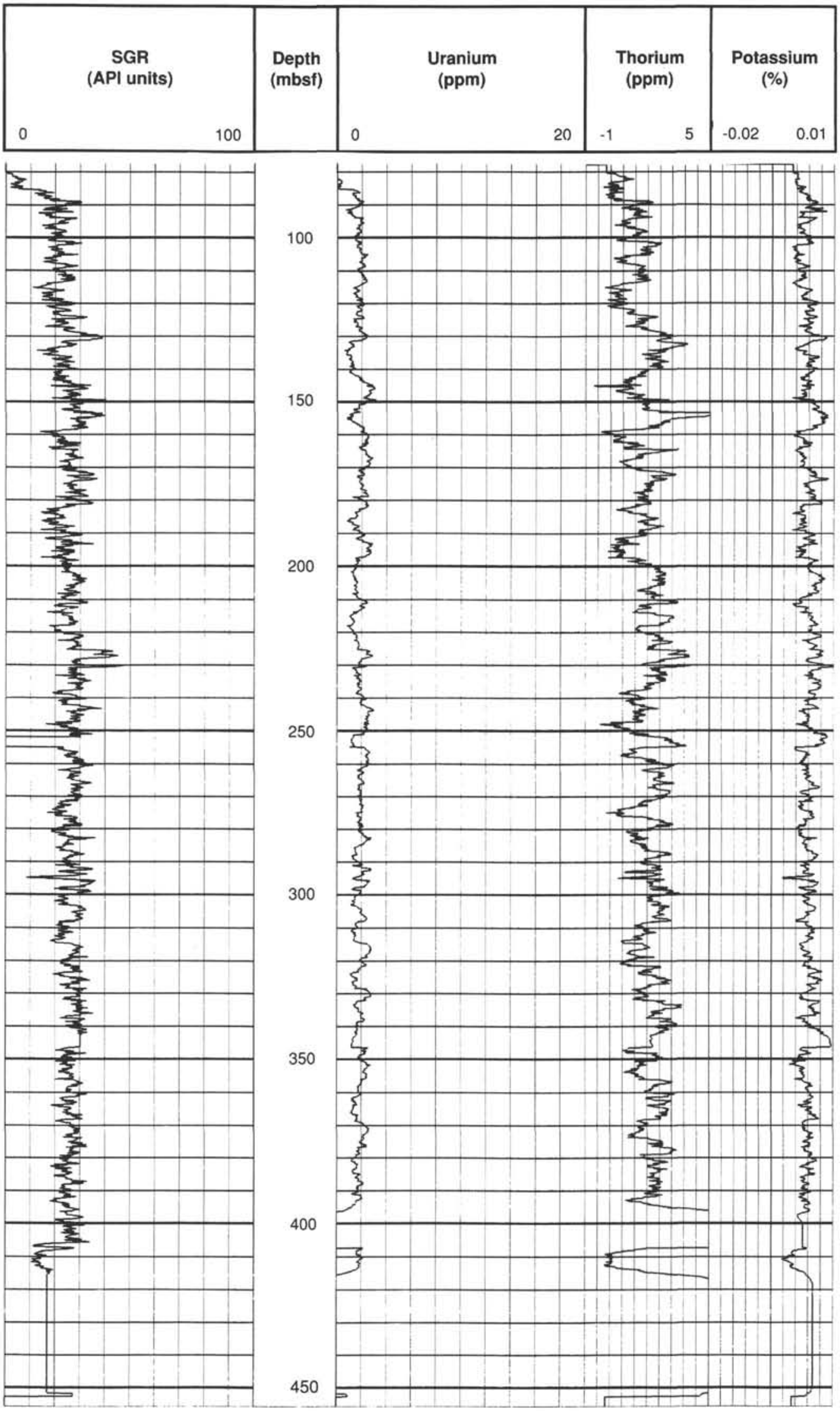

Figure 34. Spectral gamma-ray logs from Site 815 showing effect of large hole size and pipe at 85 to 95 mbsf.

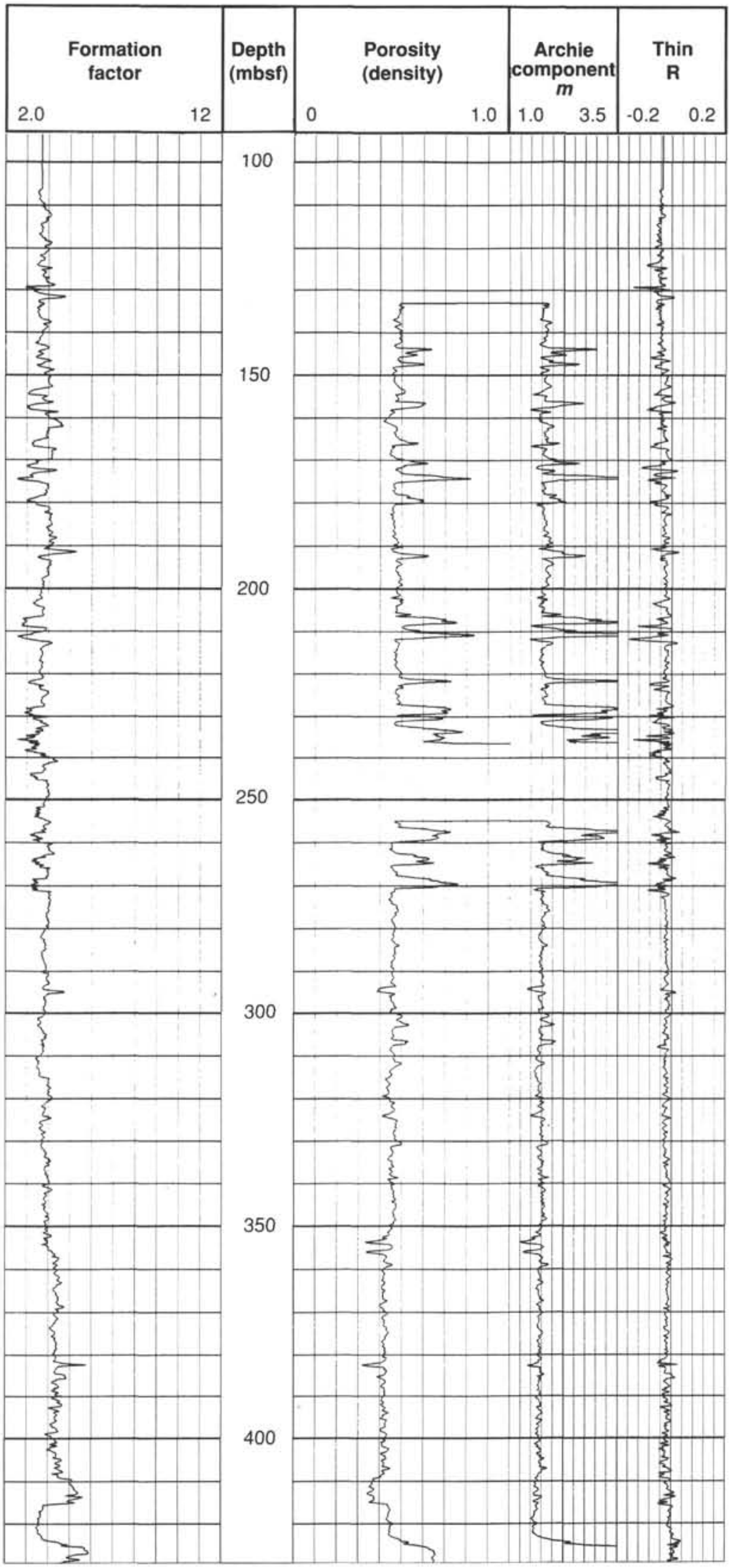

Figure 35. Formation factor (from ratio of formation resistivity to fluid resistivity), porosity (from density), and Archie (1942) component, *m*, relating formation factor to porosity at Site 815.

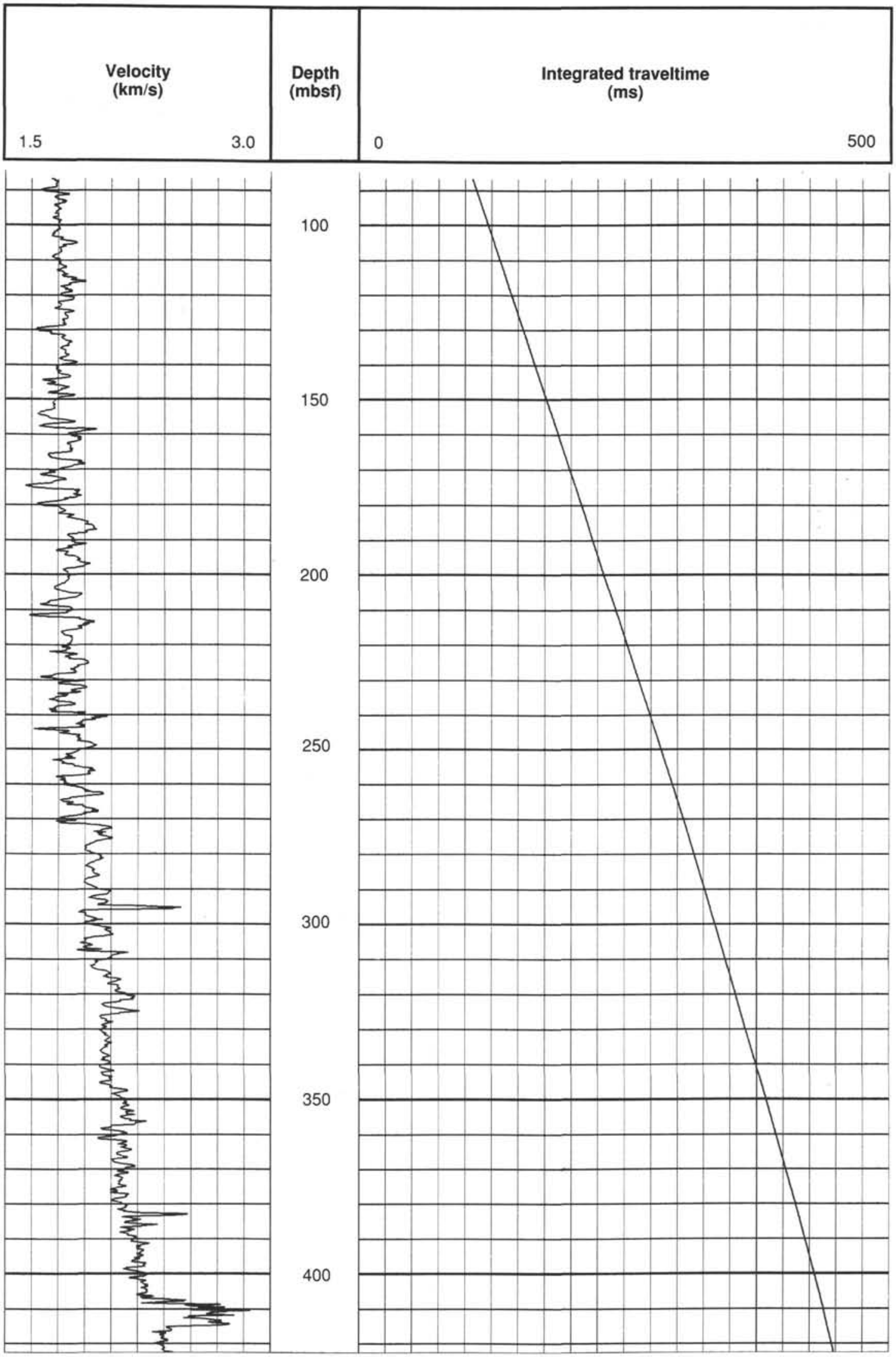

Figure 36. Velocity log and resulting integrated TWT function at Site 815 for matching core-description information from Site 815 with seismic sections from site localities.

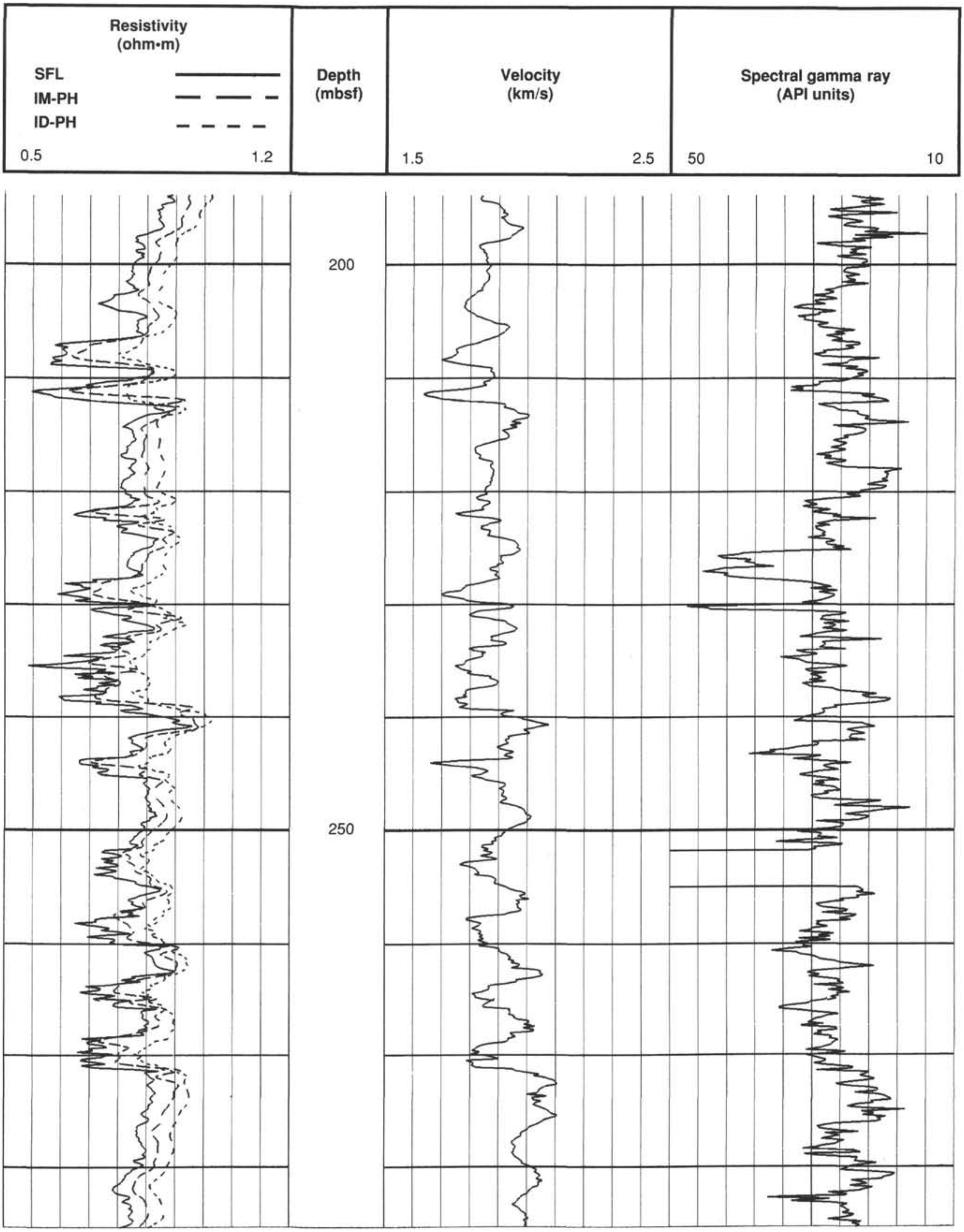

Figure 37. Cyclic nature of velocity and resistivity logs at Site 815 compared to spectral gamma-ray log at expanded scale.

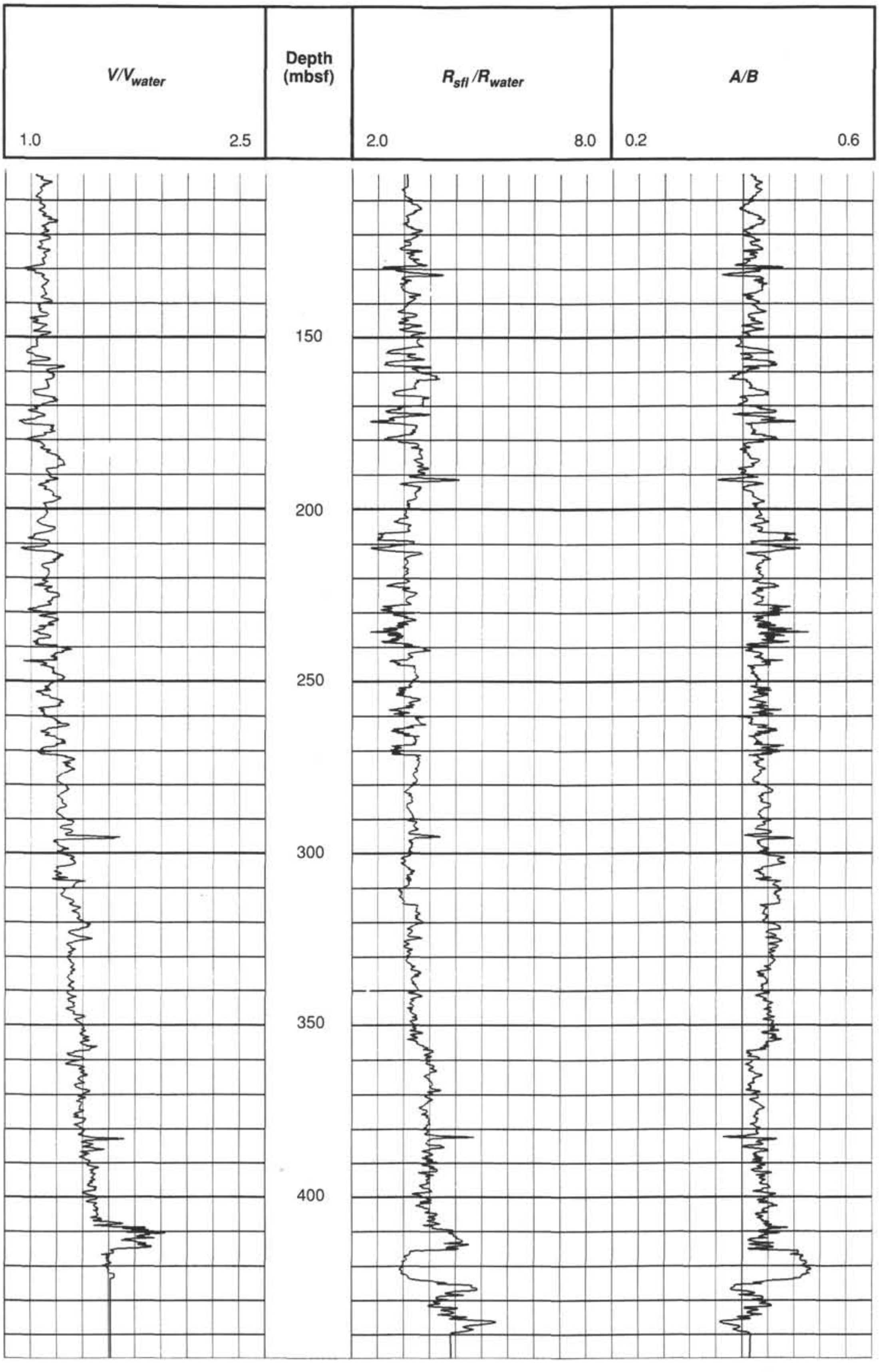

Figure 38. Velocity and resistivity ratio logs at Site 815 plotted to highlight extremely porous lithified facies that exhibit relatively high velocities and correspondingly low resistivities.

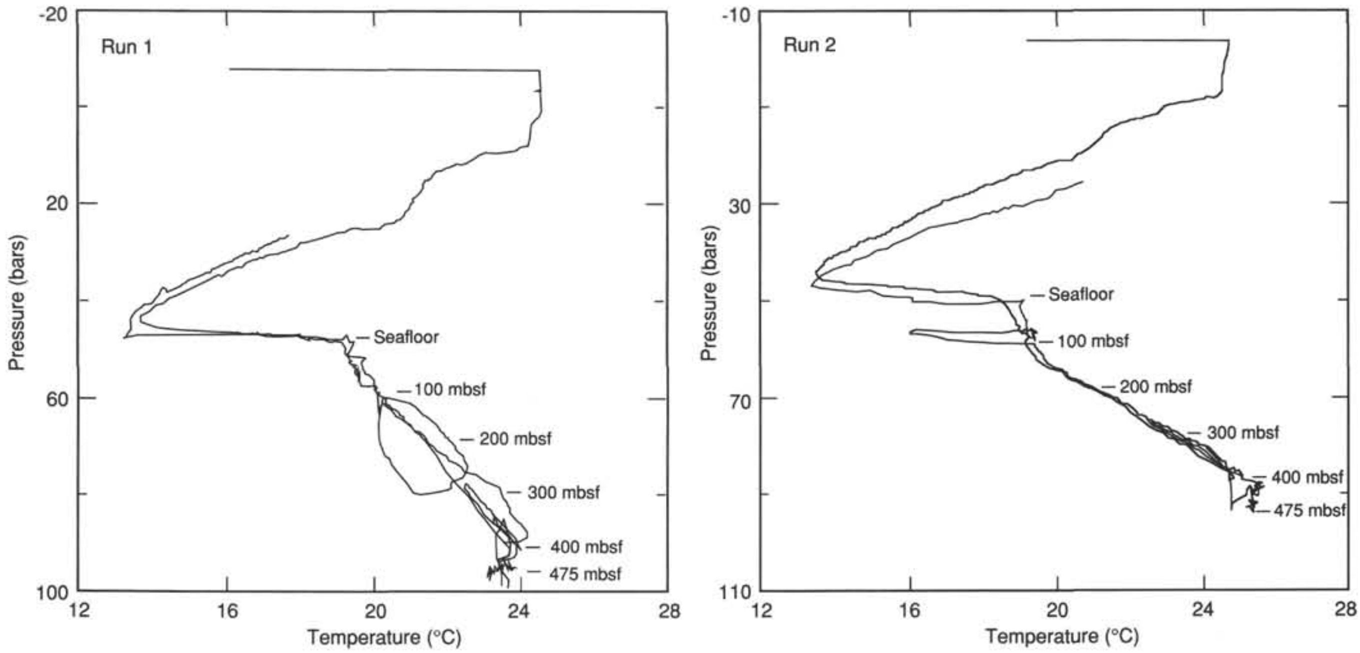

Figure 39. Temperature log as a function of pressure (or depth) at Site 815.

tized white foraminiferal rudstone, floatstone, and packstone of Unit VI.

SUMMARY AND CONCLUSIONS

Overview of Sites 815, 816, and 826

Site 815 is located on the northwestern slope of the Marion Plateau, facing the southern margin of the Townsville Trough, whereas Sites 816 and 826 are situated directly on the platform top, respectively, on the flank of a proposed reefal build-up and in a lagoonal setting behind the reef. These sites were selected to determine the nature and age of the reefal complex and to evaluate the various factors that may have led to its demise. In addition, the influence of major fluctuations in sea level on the carbonate facies and geometries could be studied at these locations. Seismic profiles across the region permit one to correlate distinct seismically imaged packages on the platform slope and top with the drilled sedimentary sequences. This correlation can provide information concerning the timing of observed stratigraphic events and should constrain the magnitude of the major decrease in sea level at the middle/late Miocene transition.

Sedimentation History

The Neogene sedimentation history for the Marion Plateau sites can be divided into two periods, based on distinctly different sediment types: (1) shallow-water carbonate production and redeposition that dominated during the latest early Miocene to late Miocene and (2) hemipelagic sedimentation that began in the latest late Miocene and prevailed throughout the Pliocene and Pleistocene. In addition, the change from shallower to deeper water sedimentation between these two periods is indicated by a change in the paleodepths at all three sites, as determined from the bioassemblages. As expected for a reefal environment, the middle Miocene paleodepths at Sites 816 and 826 were shallow. At Site 815, the benthic foraminiferal assemblage documents outer neritic water depths (100–200 m) for at least the latest Miocene. With the onset of hemipelagic sedimentation during the early Pliocene, deposition was at upper bathyal depths (200–600 m) at all three sites.

Latest Early Miocene to Late Miocene

The latest early to middle Miocene was a period of robust reefal and carbonate bank activity on the Marion Plateau. The youngest shallow-water carbonates recovered at both Sites 816 and 826 have a middle Miocene age. These sediments are unconformably overlain by lower Pliocene hemipelagic ooze and chalk. Apparently, some time during the late middle to late Miocene, the shallow-water system became inactive, probably as a result of subaerial exposure from a significant decline in sea level. Unfortunately, recovery of Miocene sediments at Site 815 was extremely poor, which prohibited a detailed analysis of the depositional environment on the platform slope. However, available samples do provide information about the timing and duration of shallow-water productivity and/or erosion processes on the platform top.

Drilling at Site 815 terminated with the recovery of uppermost lower to lower middle Miocene large benthic foraminifer rudstones within a planktonic foraminifer packstone. This lowermost lithologic unit was followed by upper Miocene foraminifer packstones, which in turn were overlain by uppermost upper Miocene foraminifer nannofossil chalks. In addition to transported reefal taxa, the latter sediments contain diagnostic outer neritic fauna. Thus, the bioassemblage in the lower three lithologic units at Site 815 indicates that the slopes of the Marion Plateau received shallow-water components until the latest Miocene. Whether these components were eroded from older deposits or whether shallow-water productivity on the platform top continued into the latest Miocene cannot be determined with certainty. However, the latest Miocene paleodepths at Site 815 apparently were within the outer neritic zone and provided a maximum water depth for this location during the period of tropical shallow-water productivity.

Early Pliocene–Pleistocene

During the early Pliocene, a rapid deepening to upper bathyal paleodepths, both at the platform slope and at the top sites, probably was a response to a relative increase in sea level produced by the combined effects of an increased

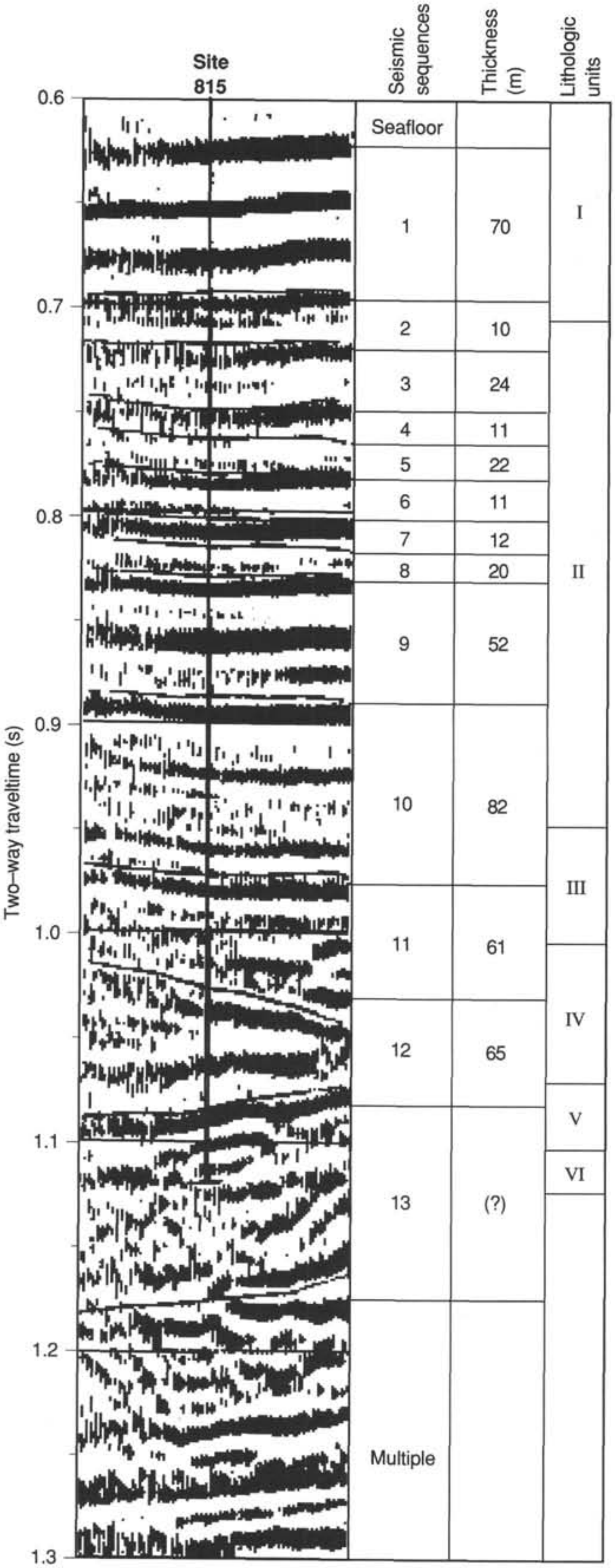

Figure 40. Seismic sequences for Site 815 showing thickness and correlation with lithologic units, based on BMR Line 75/027, Part C.

subsidence pulse and the early Pliocene global transgression event. As a result, shallow-water carbonate activity had ceased to be the dominant sedimentation process on the Marion Plateau. The tropical reef system apparently was so decimated by exposure and unfavorable environmental conditions during the late middle Miocene that renewed growth with the early Pliocene increase in sea level was impossible. On the other hand, the introduction of another factor, a major influx of fine-grained terrestrial material into the system, may have contributed to the ultimate demise of the shallow-water carbonate factory.

The hemipelagic sequences deposited across the Marion Plateau throughout the Pliocene and Pleistocene contain variable amounts of clay that has been mixed with nannofossil chalks and oozes. The terrigenous influx may account in part for the relatively high sedimentation rates, but the exceptionally high rates from the early Pliocene (up to 38.5 cm/k.y.) are best explained by lateral transport and piling up of the mixed carbonate-siliciclastic sediments in a drift deposit or contourite. Given a sufficient influx of terrestrial material and a strong current, such as the present East Australian Current, the resuspension and transport of both fine-grained pelagic carbonate and terrigenous clay should have permitted a build-up of the huge contourite deposit that we recognized in the seismic profiles across the Marion Plateau. In addition, the introduction of large quantities of fine-grained detritus along the margin should have resulted in turbid waters, environmental conditions highly detrimental to flourishing tropical shallow-water carbonate producers that inhibit adequate light penetration, thereby choking the system. Thus, the sedimentary record indicates that changing environmental conditions and sedimentation processes prevented a reactivation of the reefal systems on the Marion Plateau after the major decline in sea level at the middle/late Miocene transition.

Conclusions

In summary, the combined Neogene record recovered at Sites 815, 816, and 826 documents paleoenvironmental changes that occurred in the shallower-water regions and on the slopes of the Marion Plateau. From the latest early Miocene throughout the middle Miocene, warm tropical conditions prevailed across the platform, promoting prolific development of the reef and carbonate bank. These favorable conditions deteriorated, probably beginning in the late middle Miocene, with subaerial exposure of the productive shallow-water zones that were associated with falling sea level. With the influx of large quantities of terrigenous material along the margin during the early Pliocene, the system became inhospitable for growing tropical shallow-water fauna and flora. Since the early Pliocene, hemipelagic sedimentation has prevailed across the outer edge of the Marion Plateau. The factors controlling the transformation of Marion Plateau from a dynamic to an inactive tropical system undoubtedly are multiple and include climatic, oceanographic, terrigenous influx, eustatic sea level, and tectonic controls, and that they are intricately interrelated. These initial results obtained from drilling and from our shipboard studies are preliminary and attempts to relate the causes and consequences of the interpreted environmental changes on the Marion Plateau must wait for results obtained from shore-based studies.

REFERENCES

Andrews, J. E., 1973. Correlation of seismic reflectors. *In* Burns, R. E., Andrews, J. E., et al., *Init. Repts. DSDP*, 21: Washington (U.S. Govt. Printing Office), 459–479.

Archie, G. E., 1942. The electrical resistivity log as an aid in determining some reservoir characteristics, *J. Pet. Tech.*, 5:1–8.

Davies, P. J., Symonds, P. A., Feary, D. A., and Pigram, C. J., 1989. The evolution of the carbonate platforms of northeast Australia. *Spec. Publ. Soc. Econ. Paleont. Mineral.*, 44:233–258.

Ericson, E. K., 1976. Capricorn Basin. *In* Leslie, R. B., Evans, H. J., and Knight, C. L. (Eds.), *Economic Geology of Australia and Papua New Guinea* (Vol. 3). Australas. Inst. Mining and Metall. Monogr., 7:446–450.

Feary, D. A., Pigram, C. J., Davies, P. J., Symonds, P. A., Droxler, A. W., and Peerdeman, F., 1990. Ocean Drilling Program–Leg 133 safety package. *Bur. Miner. Res. Aust. Rec.*, 1990/6.

Haq, B. U., Hardenbol, J., and Vail, P. R., 1987. The chronology of fluctuating sea levels since the Triassic. *Science*, 235:1156–1167.

Jarrard, R. D., and Arthur, M. A., 1989. Milankovitch Paleoceanographic cycles in geophysical logs from ODP Leg 105, Labrador Sea and Baffin Bay. *In* Srivastava, S. P., Arthur, M., Clement, B., et al., *Proc. ODP, Sci. Results*, 105: College Station, TX (Ocean Drilling Program), 757–772.

Jenkins, D. G., 1985. Southern mid-latitude Paleocene to Holocene planktic foraminifera. *In* Bolli, H. M., Saunders, J. B., and Perch-Nielsen, K. (Eds.), *Plankton Stratigraphy:* Cambridge (Cambridge Univ. Press), 263–282.

Kennett, J. P., and Srinivasan, M. S., 1983. *Neogene Planktonic Foraminifera: A Phylogenetic Atlas:* Stroudsburg, PA (Hutchinson Ross).

Mullins, H. T., Thompson, J. B., McDougall, K., and Vercoutere, T. L., 1985. Oxygen-minimum zone edge effects: evidence from the central California upwelling system. *Geology*, 13:491–494.

Mutter, J. C., and Karner, G. D., 1980. The continental margin off northeast Australia. *In* Henderson, R. A., and Stephenson, P. J. (Eds.), *The Geology and Geophysics of Northeast Australia.* Geol. Soc. Aust. Queensland Div., 47–69.

Pickering, K. T., Hiscott, R. N., and Hein, F. J., 1989. *Deep Marine Environments: Clastic Sedimentation and Tectonics:* London (Unwin Hyman).

Poag, C. W., 1981. *Ecologic Atlas of Benthic Foraminifera of the Gulf of Mexico:* Stroudsberg, PA (Hutchinson Ross).

Prell, W. L., Niitsuma, N., et al., 1989. *Proc. ODP, Init. Repts.*, 117: College Station, TX (Ocean Drilling Program).

Shipboard Scientific Party, 1991. Site 808. *In* Taira, A.,, Hill, I., Firth, J. V., et al., *Proc. ODP, Init. Repts.*, 131: College Station, TX (Ocean Drilling Program), 71–269.

Stoakes, F. A., 1980. Nature and control of shale basin fill and its effect on reef growth and termination: Upper Devonian Duvernay and Ireton Formations of Alberta, Canada. *Bull. Can. Petrol. Geol.*, 28:345–410.

Symonds, P. A., and Davies, P. J., 1988. Structure, stratigraphy, evolution and regional framework of the Townsville Trough and Marion Plateau region–research cruise proposal, project 9131.11. *Bur. Miner. Res. Aust. Rec.*, 1988/48.

van Morkhoven, F.P.C.M., Berggren, W. A., and Edwards, A. S., et al., 1986. Cenozoic cosmopolitan deep-water benthic foraminifera. *Bull. Cent. Rech. Explor.-Prod. Elf-Aquitaine*, Mem. 11.

Ms 133-108

NOTE: All core description forms ("barrel sheets") and core photographs have been printed on coated paper and bound separately as Part 2 of this volume, beginning on page 813.

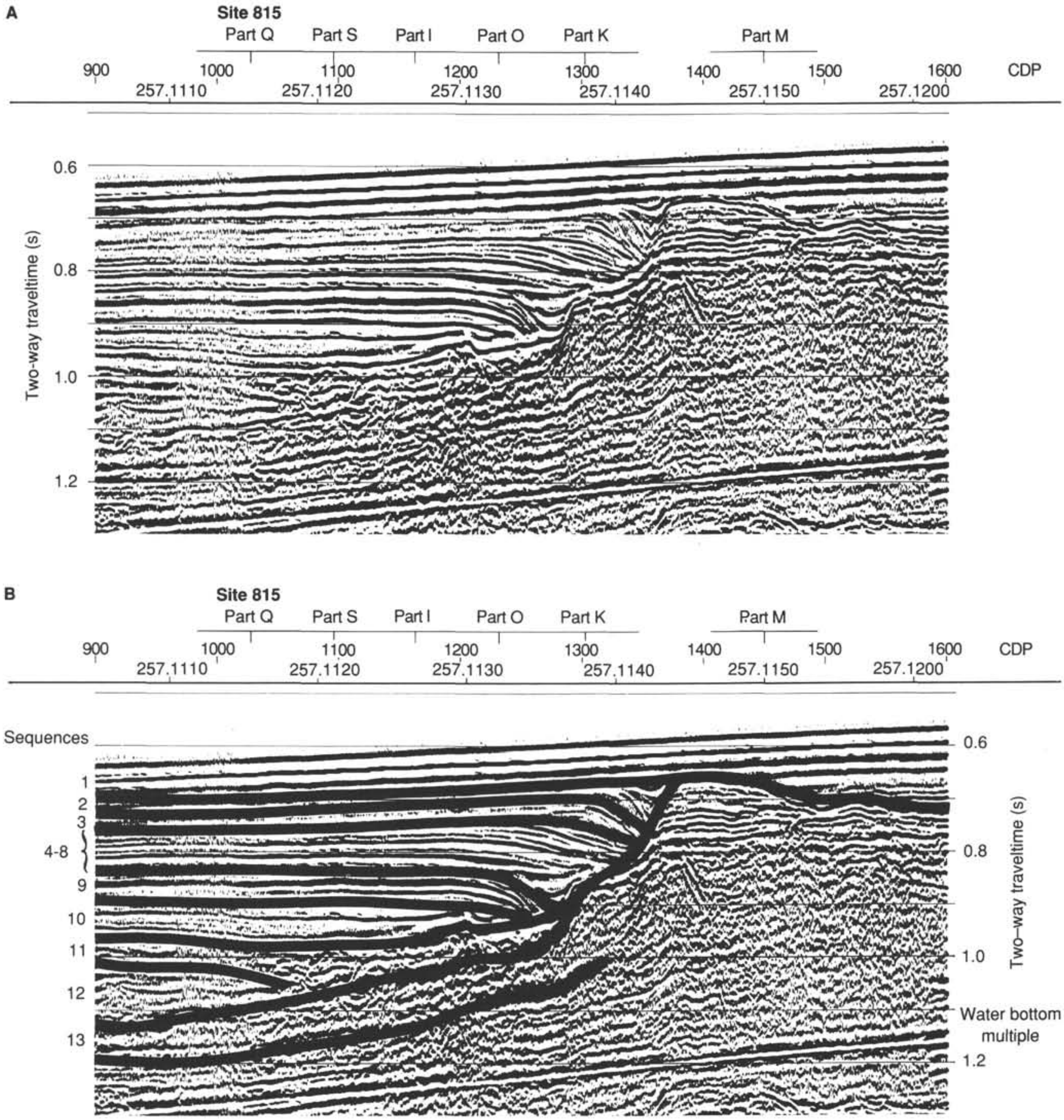

Figure 41. BMR Line 75/027, Part C, showing sequence stratigraphy in region around Site 815. Most of the sequences described at Site 815 are based on unconformities that are recognizable only to the south of the site, where many of the sequences develop downlapping or onlapping relationships. Sequence stratigraphy of section to the right of these downlapping packages is described in "Site 816" chapter (this volume). **A.** Uninterpreted seismic section through Site 815. **B.** Interpreted seismic section through Site 815.

Hole 815A: Density-Natural Gamma Ray Log Summary

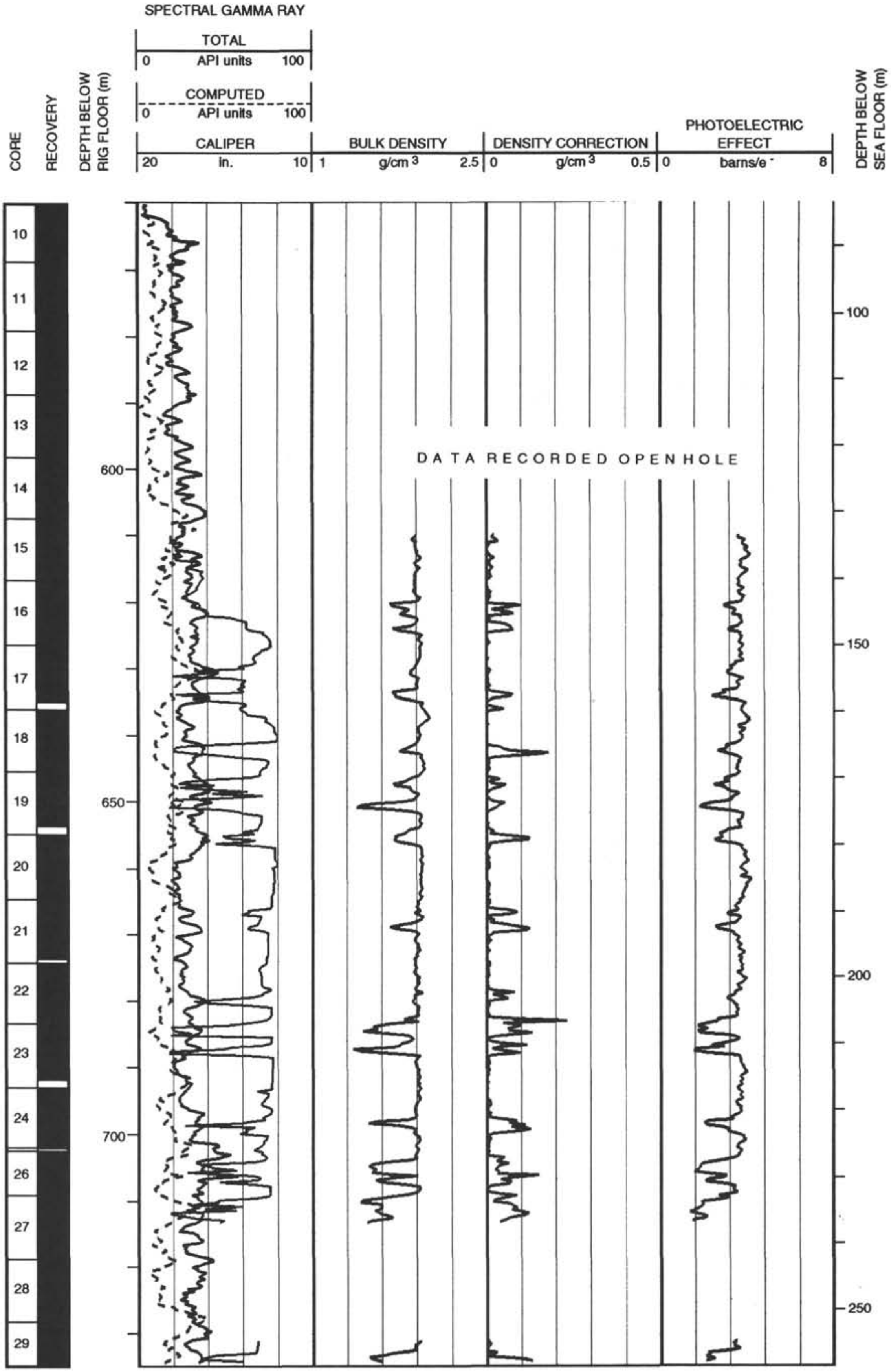

Hole 815A: Density-Natural Gamma Ray Log Summary (continued)

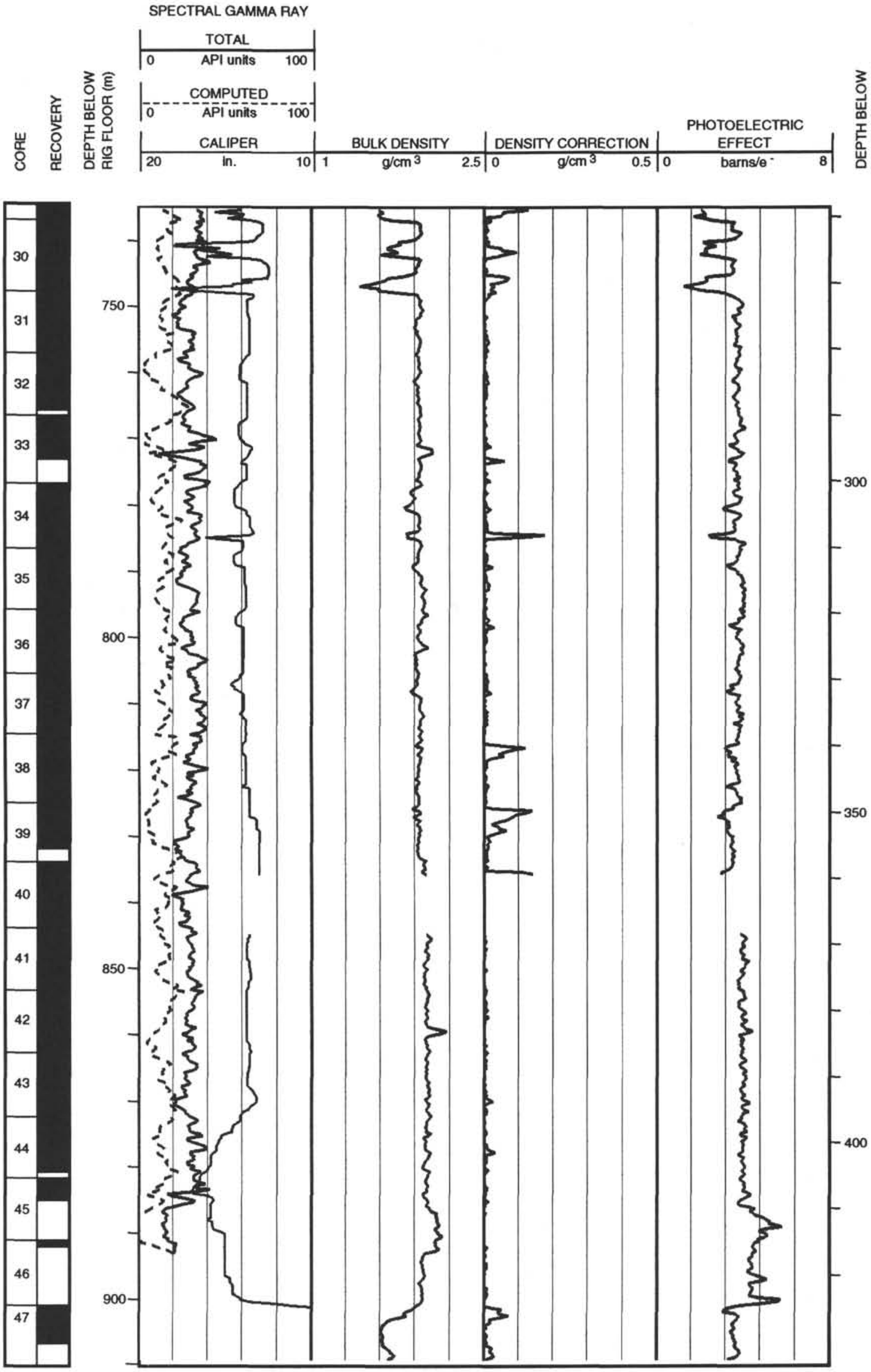

Hole 815A: Resistivity-Sonic-Natural Gamma Ray Log Summary

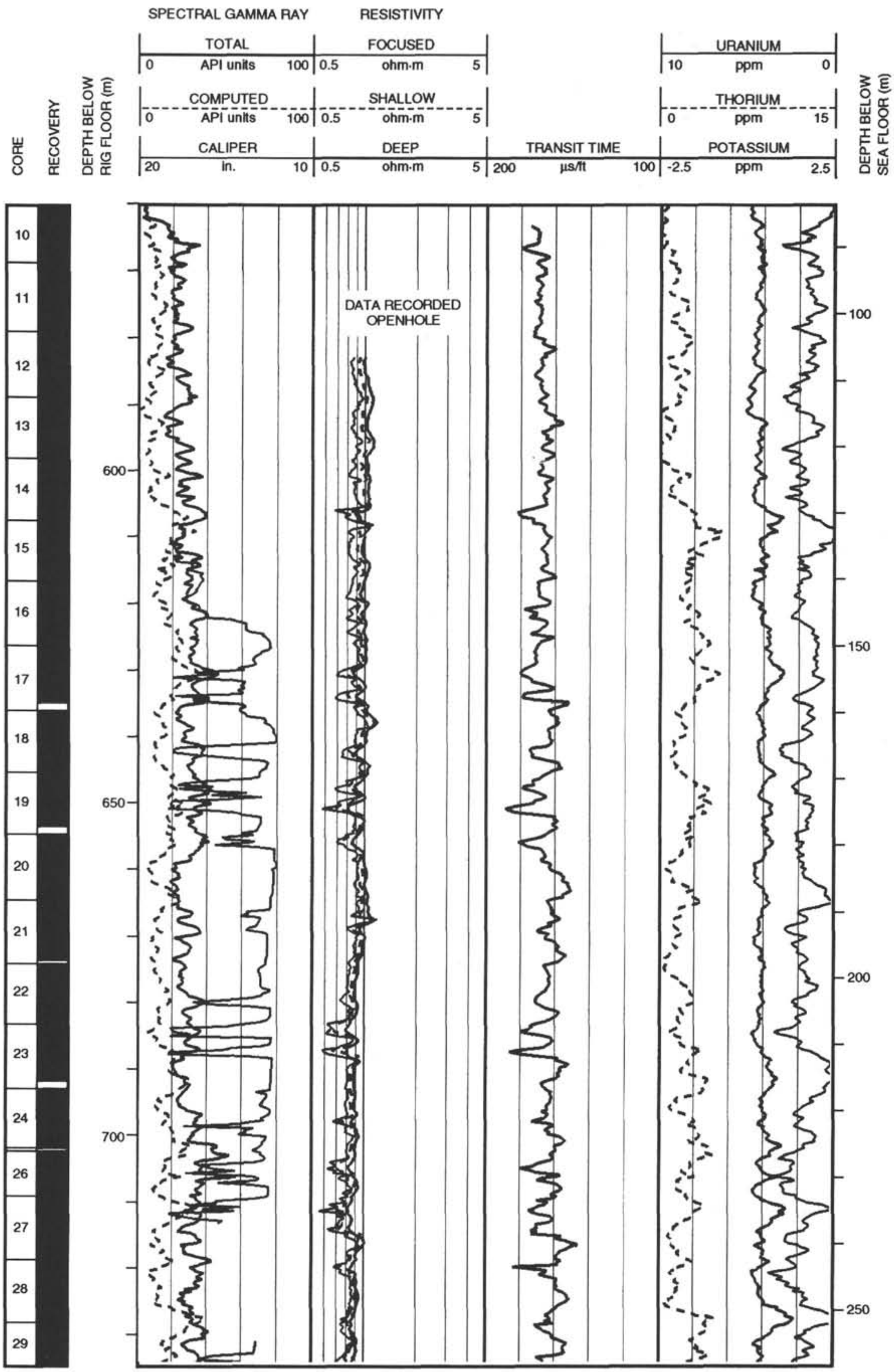

Hole 815A: Resistivity-Sonic-Natural Gamma Ray Log Summary (continued)